Neutron scattering studies of doped cuprates: $Na_8Cu_5O_{10}$ and $YBa_2Cu_3O_{6+x}$

Markus Raichle

Max-Planck-Institut für Festkörperforschung
Stuttgart 2008

Neutron scattering studies of doped cuprates:

$Na_8Cu_5O_{10}$ and $YBa_2Cu_3O_{6+x}$

Von der Fakultät Mathematik und Physik der Universität Stuttgart
zur Erlangung der Würde eines Doktors der Naturwissenschaften (Dr. rer. nat.)
genehmigte Abhandlung

vorgelegt von

Markus Raichle
aus Stuttgart

Hauptberichter: Prof. Dr. Bernhard Keimer
Mitberichter: Prof. Dr. Martin Dressel

Tag der mündlichen Prüfung: 24. Juni 2008

Max-Planck-Institut für Festkörperforschung

Stuttgart 2008

Contents

Deutsche Zusammenfassung

Diese Doktorarbeit trägt den Titel ,,Neutronenstreumessungen an dotierten Cupraten: $Na_8Cu_5O_{10}$ und $YBa_2Cu_3O_{6+x}$". Im Laufe dieser Doktorarbeit wurden mithilfe von drei unterschiedlichen neutronenspektroskopischen Messmethoden Eigenschaften der Cuprate $Na_8Cu_5O_{10}$, $YBa_2Cu_3O_7$ und $YBa_2Cu_3O_{6.6}$ untersucht. Die Gemeinsamkeit dieser drei Substanzen besteht darin, dass sie alle dotierte Mott-Isolatoren sind. Dennoch ist das Natriumcuprat $Na_8Cu_5O_{10}$ ein magnetischer Isolator, während $YBa_2Cu_3O_7$ und $YBa_2Cu_3O_{6.6}$ supraleitend sind. Dies kann dadurch erklärt werden, dass die supraleitenden Cuprate zweidimensionale Cupratschichten beinhalten mit ,,Ecken-teilenden" CuO_4-Quadraten, Natriumcuprat aber eindimensionale Cupratketten mit ,,Kanten-teilenden" CuO_4-Quadraten.
Die Arbeit ist in sieben Kapitel eingeteilt, wobei das erste Kapitel die Einleitung darstellt. Das zweite Kapitel ist eine einfache Einführung in Neutronen als Messteilchen und Neutronenstreuung im Allgemeinen. Im dritten Kapitel wird dann das Material Natriumcuprat $Na_8Cu_5O_{10}$ vorgestellt. Als wichtigstes Merkmal enthält dieses neue Material sogenannte ,,Kanten-teilende" CuO_2-Spinketten. Innerhalb dieser Spinketten wechseln sich Kupferionen mit unterschiedlichen Valenzzuständen ab (Ladungsordnung). Danach werden die Neutronen-Diffraktionsmessungen beschrieben, die am G4-2 Spektrometer in Saclay gemacht wurden. Mithilfe dieser Messungen wurde der magnetische Grundzustand von $Na_8Cu_5O_{10}$ bestimmt. Hierzu wurden die Messdaten mit dem Refinement-Programm Fullprof verfeinert. Hierbei haben wir herausgefunden, dass diese Substanz einen inkommensurablen amplitudenmodulierten magnetischen Grundzustand (Spindichtewelle) hat. Dieser magnetische Grundzustand ist in Einklang mit physikalischen Überlegungen und bisherigen Experimenten. Die Inkommensurabilität wird in diesem Kapitel mithilfe eines einfachen Modells erklärt, das auf konkurrierenden Wechselwirkungen zwischen Spins beruht.
Im vierten Kapitel werden die wichtigen Bestandteile eines Dreiachsenspektrometers erklärt. Hierzu gehören die Abschirmung, der Monochromator, der Analysator, Kollimatoren, Filter und Absorber. Zum Abschluss des Kapitels wird die Justage des Spektrometers beschrieben.
Im fünften Kapitel wird zunächst beschrieben, wie eine Probe justiert wird. Danach

wird der Streuquerschnitt für Phononen hergeleitet. Hieraus können interessante Folgerungen für Phononenexperimente mit Neutronen gezogen werden. Insbesondere ist eine Aussage darüber möglich, an welchem Punkt im reziproken Raum die Intensität für Phononenmessungen am stärksten ist. Im Weiteren wird in diesem Kapitel noch die Auflösungsfunktion des Dreiachsenspektrometers beschrieben. Diese ist von Bedeutung, um später den Einfluss des Spektrometers auf die Linienbreite der gemessenen Phononen herausrechnen zu können und somit die genaue intrinsische Linienbreite der Phononen bestimmen zu können. Zum Abschluss dieses Kapitels werden die ebenfalls sehr wichtigen ,,falschen Signale" besprochen. Diese Signale können unter bestimmten Spektrometerkonfigurationen im Detektor auftreten, ohne dass hierbei ein inelastischer Streuprozess an der Probe stattfindet. Daher müssen sie nach Möglichkeit vermieden, auf jeden Fall aber erkannt werden.
Im sechsten Kapitel wird zunächst das System $YBa_2Cu_3O_{6+x}$ beschrieben. Hierbei wird die Struktur erklärt, die im wesentlichen aus der supraleitenden CuO_2-Doppelschicht und den CuO-Ketten besteht. Die CuO-Ketten sind je nach Dotierungsgrad mehr oder weniger mit Sauerstoffionen gefüllt. Hierbei wird die CuO_2-Doppelschicht mit Löchern dotiert. Je nach Dotierung ist das System $YBa_2Cu_3O_{6+x}$ dann ein antiferromagnetischer Mott-Isolator oder ein Supraleiter. Wenn man die Übergangstemperatur des supraleitenden Zustandes über der Dotierung abträgt, erhält man zwei Plateaus, bei denen sich die Übergangstemperatur nur schwach verändert mit der Dotierung und die fast den ganzen supraleitenden Bereich beschreiben. Unsere beiden Proben befinden sich genau in diesen beiden unterschiedlichen Plateaus. Diese beiden Plateaus sind ein wesentlicher Bestandteil des entsprechenden Phasendiagramms von $YBa_2Cu_3O_{6+x}$, welches auch im fünften Kapitel ausführlich besprochen wird. Zu Vergleichszwecken haben wir darüber hinaus noch die antiferromagnetische Substanz $YBa_2Cu_3O_{6.1}$ untersucht.
Danach werden kurz wichtige Eigenschaften der Hochtemperatursupraleiter besprochen. Hierzu gehört die Paarungssymmetrie der Cooperpaare. Im Gegensatz zur s-Wellen- Symmetrie in konventionellen Supraleitern, haben die (unkonventionellen) Hochtemperatursupraleiter eine d-Wellen-Symmetrie. Dies wurde insbesondere durch Tunnel- und ARPES-Messungen herausgefunden. Das "Pseudogap" ist eine weitere Besonderheit, die nur bei unkonventionellen Supraleitern auftritt. Hierbei ist die Zustandsdichte der elektronischen Zustände über dem Ferminiveau auch oberhalb von T_c deutlich reduziert. Danach wird die ,,Buckling"-Phononenmode beschrieben. Sie entsteht durch die Oszillation der Sauerstoffionen innerhalb der CuO_2-Doppelschicht. Hierbei schwingen diese Ionen transversal, d.h. orthogonal zur CuO_2-Doppelschicht. Die Bedeutung dieser Mode beruht auf theoretischen Vorhersagen, denen zufolge diese Mode zur Bildung von Cooper-Paaren mit d-Wellen-Symmetrie besonders stark beiträgt. Dann werden wichtige frühere Experimente besprochen, die eine supraleitungsinduzierte Anomalie dieser Phononenmode beschreiben. Möglicherweise steht diese Anomalie mit dem in ARPES-Messungen festgestellten ,,,Kink" in der

Dispersionsrelation der Elektronen in Verbindung. Dieser Zusammenhang wird zur Zeit allerdings sehr kontrovers diskutiert. Im Weiteren wird noch auf andere Phononenanomalien und auf die Streifentheorie Bezug genommen. Diese könnten mit dem von uns untersuchten supraleitungsinduzierten Effekt der ,,Buckling-Mode" in Zusammenhang stehen.
In den Unterkapiteln 6.9 und 6.11 werden dann unsere Phononenmessungen der ,,Buckling"-Mode in $YBa_2Cu_3O_7$ und $YBa_2Cu_3O_{6.6}$ dargestellt. Zunächst werden jeweils die wichtigsten Ergebnisse unserer Messungen zusammengefasst. In dem Energiebereich, in dem bisher nur die ,,Buckling"-Mode beobachtet wurde, konnten wir noch zwei weitere Moden messen. Dies kann dadurch erklärt werden, dass wir mit einer höheren Auflösung und an entzwillingten Kristallen gemessen haben. Diese drei Moden konnten durch den Vergleich der Messdaten mit Raman- und Infrarotmessungen identifiziert werden. Unterhalb der ,,Buckling"-Mode konnten wir eine Mode des apikalen Sauerstoffs messen und bei höherer Energie eine Mode, bei der Sauerstoffionen innerhalb der Doppelschicht und in den Sauerstoffketten schwingen. Diese letztere Mode wurde für die Dotierung $x = 1.0$ in beiden Richtungen entlang der a^*-Achse und der b^*-Achse gemessen, wohingegen sie für die Dotierung $x = 0.6$ nur entlang der b^*-Achse beobachtet wurde. Dies ist dadurch erklärbar, dass bei dieser Mode unter anderem die Sauerstoffionen in den Ketten schwingen, deren Konzentration sehr stark dotierungsabhängig ist. Die apikale Mode ist im allgemeinen sehr schwach, daher konnten wir sie lediglich für $YBa_2Cu_3O_7$ mit hinreichender Statistik messen. Für $q = 0.3$, $x = 1.0$ konnten wir einen supraleitungsinduzierten Austausch des Spektralgewichts zwischen dieser apikalen Mode und der ,,Buckling"-Mode nachweisen. Hierbei nimmt die Intensität der ,,Buckling"-Mode deutlich ab, wohingegen die Intensität der apikalen Mode deutlich zunimmt. Dies bedeutet, dass sich supraleitungsinduziert der Eigenvektor des Phonons verändert, und nicht nur die Energie und die Linienbreite. Dieser Effekt ist auf einen engen Bereich der Brillouin-Zone um den zweidimensionalen Wellenvektor $q = (0, 0.3)$ herum beschränkt; ein analoger Effekt bei $q = (0.3, 0)$ wurde nicht beobachtet. Dies deutet auf eine ungewöhnliche Elektron-Phonon-Wechselwirkung hin, die durch kollektive Moden hervorgerufen werden könnte. Die Anisotropie des Effektes kann im Wesentlichen dadurch erklärt werden, dass die apikale Mode für die a^*-Richtung nicht in der Nähe der ,,Buckling"-Mode liegt. Daher ist die Streifentheorie als eventuelle Erklärungsmöglichkeit für diesen stark anisotropen Effekt nicht notwendig.
Für $x = 0.6$ konnten wir einen ähnlichen Effekt beobachten: bei $q = (0, 0.35)$ nimmt die Intensität der ,,Buckling"-Mode deutlich ab, allerdings konnte hierbei die apikale Mode nicht eindeutig aufgelöst werden. Wir vermuten dennoch einen ähnlichen Mechanismus wie für $x = 1.0$. Es ist wichtig, dass dieser Effekt sowohl in $YBa_2Cu_3O_7$ als auch in $YBa_2Cu_3O_{6.6}$ beobachtet wurde, denn bisher wurden supraleitungsinduzierte Phononeneffekte in Yttriumbariumcuprat nur beim optimal dotierten Ma-

terial festgestellt. In der Tat konnten bisher festgestellte supraleitungsinduzierte Phononeneffekte (Renormalisierung der Phononenenergie) für $x = 1.0$ und $q = 0$ reproduziert werden. Für $x = 0.6$ und $q = 0$ konnte ein solcher Effekt ebenfalls in Einklang mit früheren Messungen nicht beobachtet werden. Allerdings ergab sich in Ergänzung zu diesen früheren Messungen ein anisotropes Verhalten der ,,Buckling"-Mode innerhalb der Brillouinzone. Das interessante Verhalten der ,,Buckling"-Mode ist schliesslich im letzten Abschnitt des fünften Kapitels zusammengefasst (siehe 6.12).
Das siebte Kapitel enthält Spin-Echo-Messungen über die ,,Buckling"-Mode in $YBa_2Cu_3O_7$. Zunächst wird kurz das Funktionsprinzip des Spin-Echo-Spektrometers Trisp am FRMII in München beschrieben, an dem die Messungen durchgeführt wurden. Die Messergebnisse sind konsistent mit unseren Dreiachsenmessungen an derselben Probe.

Chapter 1

Introduction

It is well known that ordinary metals such as mercury and lead exhibit superconductivity at low temperatures. In these conventional superconductors the dissipationless current originates from the formation of so-called s-wave Cooper pairs. This is possible due to the instability of the Fermi liquid to any non-zero attractive interaction, which is the electron-phonon coupling for conventional superconductors. Since 1986 so-called high temperature superconductors with transition temperatures above the boiling point of liquid nitrogen have been discovered. These are called unconventional superconductors, because the phase transition breaks not only gauge symmetry but also spatial symmetries. In the high temperature superconductors, the Cooper pair wave function has d-wave symmetry. However, the mechanism underlying the formation of Cooper pairs in these materials is still controversial. As in many other transition metal oxides, the conduction electrons in the cuprates exhibit strong electronic correlations leading to interesting magnetic phenomena. In particular, the undoped parent compound ($x = 0$) of the system $YBa_2Cu_3O_{6+x}$ is a Mott insulator. According to band theory this material should be a metal. However, due to the strong electronic correlations the valence band is split into two sub-bands, and only the lower sub-band is filled. As a consequence, it becomes an antiferromagnetic insulator. By introducing holes into such a Mott-insulating state, so-called Zhang-Rice singlets are formed which have no net magnetic moment.
The superconducting cuprates are doped Mott insulators. $Na_8Cu_5O_{10}$ is an example of a doped Mott insulator that remains insulating. It is a relatively new substance which was synthesized recently at the MPI-FKF. The special experimental challenge during the work with this material was its air sensitivity. The important building block in this cuprate is the one dimensional CuO_2 spin chain which consists of edge-sharing CuO_4 units. Within these chains, spin bearing copper ions and nonmagnetic Zhang-Rice singlets alternate. In contrast to the superconducting cuprates this material does not become superconducting upon doping. Instead it develops a charge-ordered state in which spin-bearing copper ions and Zhang-Rice singlets

alternate. This thesis describes the determination of the magnetic ground state of the charge-ordered chains in $Na_8Cu_5O_{10}$. We show that the magnetic ground state is a spin-density wave, with periodicity different from that of the charge-ordered state. Charge order with uniaxial propagation vector ("stripes") has also been observed in some families of high temperature superconductors, such as $La_{2-x}Ba_xCuO_4$ with $x = \frac{1}{8}$. However, it is still controversial whether this state is generic to this family of materials and whether fluctuations characteristic of dynamical stripes play an essential role for high temperature superconductors. Evidence for these dynamical stripes has been claimed based on the observation of phonon anomalies. This is one reason why it is interesting to investigate phonons in high temperature superconductors.

A very important observation in the high temperature superconductors is the appearance of a magnetic resonance mode below the superconducting transition temperature. As this collective magnetic excitation is directly related to the superconducting transition, there are good reasons to believe that the Cooper pairs in the cuprates may be formed due to attractive antiferromagnetic correlations. However, until now the role of the electron-phonon coupling in the cuprates is still unclear. This is the second reason why investigating phonons in cuprates is interesting. Whereas the presence of superconductivity-induced phonon effects in these cuprates is undisputed, the relation of these effects to the formation of the Cooper pairs is still highly controversial. In order to clarify the role of the phonons for the Cooper pair formation in high-temperature superconductors, these superconductivity-induced phonon effects should be studied more intensively for different cuprates and by different spectroscopic methods. In chapter 6 we present our recent contribution to this research field. We performed inelastic neutron scattering measurements on the phonon buckling mode in the system $YBa_2Cu_3O_{6+x}$ for doping levels $x = 0.1$, $x = 0.6$ and $x = 1$. This particular phonon mode has showed superconductivity-induced phonon softening in previous experiments for $x = 1$ and has been predicted to support the experimentally observed d-wave pairing state. In addition to this effect, we found a novel anisotropic superconductivity-induced transfer of spectral weight of the buckling phonon mode to another phonon mode. This new effect is a strong indication of an unusual electron-phonon interaction and therefore should influence the debate on the importance of electron-phonon interactions in high T_c materials. Its observation was made possible by our fully detwinned samples and the high resolutions of the spectrometers Puma at FRMII in Munich and 1T1 in Saclay. In previous measurements this q-dependent and anisotropic effect could not be observed as crystallographic twinning and lower spectrometer resolution mixed up contributions from different directions and different phonon modes. In measurements on $YBa_2Cu_3O_{6.6}$ (underdoped) with lower resolution we also observed a loss in intensity of the buckling mode, which is consistent with a picture of two interacting phonon modes.

There follows a brief comparison of the two materials investigated in this thesis $YBa_2Cu_3O_{6+x}$ and $Na_8Cu_5O_{10}$. Although both compounds are doped Mott insulators with strongly correlated electrons, they behave completely differently; whereas Yttrium Barium Cuprate shows superconductivity upon doping, Sodium Cuprate remains a magnetic insulator. The main difference between the two investigated compounds is the dimensionality of their electronic structure, which derives from copper oxide planes in Yttrium Barium Cuprate and chains in Sodium Cuprate. The planes in $YBa_2Cu_3O_{6+x}$ consist of corner-shared CuO_4-units, whereas the chains in $Na_8Cu_5O_{10}$ have edge-shared CuO_4-units. Compared to corner-sharing cuprates with a Cu-O-Cu bond angle of 180°, the edge-sharing cuprates have a Cu-O-Cu bond angle around 90°. As a result in the edge-sharing cuprates two orthogonal p-orbitals overlap with the d-orbitals of the copper ions. Hence the hopping of the electrons is strongly reduced and the corresponding superexchange is very weak. This explains why even doped edge-sharing 1D cuprates are insulators.
This thesis is organized as follows: The first chapter is an introduction to the topic and the second to neutron scattering. The third chapter introduces the doped Sodium Cuprate $Na_8Cu_5O_{10}$ and presents the magnetic neutron diffraction measurements that have been performed in order to determine its magnetic structure: a spin-density wave with commensurate spin modulation along the charge ordered chains and with incommensurate spin modulation perpendicular to these chains. The fourth chapter provides an extensive description of a triple axis spectrometer, the instrument used for the phonon measurements on $YBa_2Cu_3O_{6+x}$. In the fifth chapter the dynamical structure factor for phonons is derived. This leads to important information on how to optimize the phonon measurements on the buckling mode. Then it is explained how such a phonon measurement works and the resolution function is discussed. This chapter concludes with the discussion of spurious effects. It is very important to be aware of these effects as they can pretend physical effects which are not present. The sixth chapter begins with the description of the system $YBa_2Cu_3O_{6+x}$ in general and especially of the buckling mode in that system. Moreover previous measurements connected to the buckling mode are reviewed. Sections 6.9 - 6.11 present the inelastic neutron measurements we performed on the buckling mode in $YBa_2Cu_3O_7$ and $YBa_2Cu_3O_{6.6}$ as well as control measurements on undoped $YBa_2Cu_3O_{6.1}$. In particular, we describe a new anisotropic superconductivity-induced phonon effect related to unusual electron-phonon interaction. Section 6.12 contains a summary of these measurements and a discussion on how these measurements can be understood and related to previously reported measurements and effects, especially a possible relation to the well known "kink" in ARPES measurements. The final chapter explains the principle of a spin echo spectrometer and data acquisition. It reports our spin echo measurements on the buckling mode in $YBa_2Cu_3O_7$. These measurements are consistent with our triple axis measurements.

Chapter 2

Neutrons and reciprocal space

2.1 Neutrons for experiments

The neutron is composed of three quarks, one up and two down quarks, so that the neutron has no net electric charge. However it has a charge distribution leading to a finite radius and a net magnetic moment of $\mu_n = 1.91\mu_N$ [1]. Moreover the neutron has a finite mass of around $m_N = 1u$ and spin 1/2. This has important consequences for neutron scattering, as the neutron can not only interact with the atomic nuclei through the strong interaction force but also with the electrons by magnetic dipole-dipole interaction. Therefore one distinguishes between nuclear neutron scattering and magnetic neutron scattering. The free electron has a finite lifetime of 10 minutes and 16 seconds. However this is no problem for neutron scattering experiments. If one makes measurements with neutrons in the thermal energy range $10meV < E_N < 100meV$ (if E_N is the energy of the neutron below this energy range one speaks of cold and above this energy range of hot neutrons), for example with $60meV$, then the velocity of the neutrons is around $3.4km/s$ that means that the neutrons cover the distance from the neutron source to the detector within milliseconds.
Nowadays there are two possible designs of neutron sources: fission and spallation sources. In a fission reaction a thermal neutron is absorbed by a ^{235}U-nucleus which then decomposes into smaller nuclei and several neutrons. On average one fission reaction produces 2.5 highly energetic neutrons (with a kinetic energy of $\sim 2MeV$). In addition the heat of the other reaction products of around $200MeV$ per neutron has to be cooled away. An example of a fission source is the neutron reactor Orphée in Paris at the Laboratoire Léon Brillouin. This reactor is a swimming pool type reactor with a thermal power of $14MW$ and a neutron flux of $3 \cdot 10^{14}$ neutrons per $cm^{-2}s^{-1}$: In order to produce a significant neutron flux the fuel elements (the core of the reactor, aluminium - uranium alloy enriched with ^{235}U) are separated

by narrow channels of water. This ensures a large thermal energy exchange per unit volume. The nuclear reaction is controlled by vertically moving control rods consisting of a material which is absorbing neutrons (Hafnium). The core is placed in a reflector of heavy water circulating from bottom to top in a stainless steel vat. In order to protect the scientists from the neutron beam in addition the core is surrounded by a pool of light water with $15m$ height and $4.5m$ in diameter, and the pool is surrounded by a $1.5m$ thick concrete wall. There are 9 horizontal tubes which are tangential to the core (in order to reduce fast neutrons in the neutron beams). In this way 20 neutron beams are made available for the spectrometers. As mentioned before the core is situated in a heavy water tank, which is $2m$ high and has a diameter of $2m$. The water is kept at a temperature of around 50 degree Celsius in order to operate as a moderator for the thermal beam tubes. Thus one obtains for example for the spectrometer 1T at the first beam tube a flux of thermal neutrons of about $3.93 \cdot cm^{-2}s^{-1}$. This measurement was made by activation of a gold foil. There are also beam tubes for cold and hot neutrons available. For the cold neutron beams a "cold source" of liquid hydrogen is used as a moderator and for the hot neutron beams a "hot source" of a heated graphite cylinder (with $1400K$) is used as a moderator.
In a spallation source highly energetic protons (around $1GeV$) are fired at heavy nuclei, which are excited by the collision. Afterwards the nuclei eject neutrons with the energy of $1 - 2MeV$. One of the strongest spallation sources is ISIS in Great Britain at the Rutherford Appleton Laboratory. An important difference between the spallation sources and a reactor is that the spallation sources are pulsed. That means that there is no continuous flux of neutrons.

2.2 Energy and momentum conservation and the dispersion relation of neutrons

For scattering and diffraction experiments of neutrons the following conservation laws are important: the conservation of energy and the conservation of momentum [2]:

$$\hbar\omega = E_i - E_f \tag{2.1}$$

$$|\vec{K}| = k_i^2 + k_f^2 - 2k_i k_f \cos\theta_S \tag{2.2}$$

$$\vec{K} = \vec{k}_f - \vec{k}_i. \tag{2.3}$$

$\vec{K}$ is called the scattering vector. $\vec{k}_i$ and $\vec{k}_f$ are the wave vectors of the neutrons in the incident and the final beams. The angle between the incident and the final beam is $2\theta_S$, whereas θ is called the scattering angle of the sample. The wavelength of the neutrons is $\lambda = 2\pi/|\vec{k}|$. E_f and E_i are the energies of the neutrons in the

incident and final beams. These conservation laws are important for elastic and inelastic neutron scattering. For elastic neutron scattering the values $|\vec{k}_i|$ and $|\vec{k}_f|$ are equal, whereas they are different for inelastic neutron scattering.
A further very important relationship for neutron scattering experiments is the dispersion relation for neutrons:

$$E = \frac{\hbar^2 k^2}{2m_n} \tag{2.4}$$

$$E[meV] = 2.072 k^2[\mathring{A}^{-2}] \tag{2.5}$$

with m_n the mass of the neutron. The second equation is practical if one wants to calculate the energy from the wave vector of the neutrons. Thermal neutrons are important for measuring collectives excitations in condensed matter, such as phonons, because their energy is well matched to the energy of such excitations.

2.3 Differential cross section for neutron scattering

The content of this section can also be found in the good article of H.Zabel [3]. A neutron experiment means that a neutron beam characterized by the initial wave vector k_i and the corresponding energy $E_i = \hbar^2 k_i^2/2m$ is scattered by the sample due to interaction processes of the neutrons with the sample. The interesting experimental quantity is the differential cross section it measures the neutrons being scattered in a given solid angle $d\Omega_f$ in the direction of the wave vector k_f with a final energy between E_f and $E_f + dE_f$. One distinguishes between the coherent and the incoherent part of the differential cross section [3]:

$$\frac{d^2\sigma}{d\Omega_f dE_f} = \frac{d^2\sigma}{d\Omega_f dE_f}|_{coh} + \frac{d^2\sigma}{d\Omega_f dE_f}\ |_{incoh}\ . \tag{2.6}$$

Incoherent scattering occurs for mono atomic samples if there are different isotopes and if the atoms have a nuclear spin which is not parallel for all the atoms. That means that the scattering length of the various atoms are different. In most of the cases incoherent scattering leads to an unwanted intrinsic background of the sample. Whereas the coherent part of the scattering cross section provides information about cooperative effects among the atoms which lead to elastic Bragg scattering but also to inelastic scattering by phonons and magnons. Therefore in the following text the coherent scattering cross section will be treated as the final goal is to derive the structure factor for elastic Bragg scattering and the dynamical structure factor for phonons.
The interaction between the neutrons and the sample which is considered here is

weak in that sense that the neutrons doesn't change the nature of the eigenstates itself but cause a transition between different eigenstates of the sample. For this case Fermi's golden rule describes the interaction of the neutrons with the sample and the differential cross section can be written:

$$\frac{d^2\sigma}{d\Omega_f dE_f} = \frac{k_f}{k_i}\left(\frac{m_n}{2\pi\hbar}\right)^2 |\langle\vec{k}_f\lambda_f|V|\vec{k}_i\lambda_i\rangle|^2\delta(\hbar\omega + E_i - E_f), \tag{2.7}$$

where m_n is the neutron mass, λ_f is the final eigenstate of the sample, λ_i is the initial eigenstate of the sample and $\hbar\omega$ is the excitation energy of the quasi particle (inelastic scattering). As the interaction is weak one can calculate the matrix element using the Born approximation and treat the incident and final neutrons as plane waves. Moreover one can assume the scattering centers identical (one atom per unit cell) and for nuclear scattering the interaction potential is a δ-function in space. Then it follows for the (coherent) differential cross section:

$$\frac{d^2\sigma}{d\Omega_f dE_f} = N\frac{k_f}{k_i}\frac{\sigma_{coh}}{4\pi}\cdot S(\vec{K},\omega) \tag{2.8}$$

where N is the number of nuclei and $\sigma_{coh} = 4\pi b^2$ is the coherent cross section with b being the scattering length of identical, coherent scatterers. $S(\vec{K},\omega)$ is the scattering function given by:

$$S(\vec{K},\omega) = \frac{1}{2\pi\hbar N}\sum_{ll'}\int_{-\infty}^{\infty} dt\langle\exp(-i\vec{K}\vec{R}_{l'}(0))\exp(i\vec{K}\vec{R}_l(t))\rangle\exp -i\omega t, \tag{2.9}$$

where $\vec{K}$ is the scattering vector, t is the time, $\vec{R_{l'}}(0)$ and $\vec{R_l}(t)$ are position vectors at different times for different nuclei labelled by l' and l. The brackets indicate the average over initial states also called the thermal average. The goal of most neutron scattering experiments is to measure $S(\vec{K},\omega)$ and thereby determine the microscopic properties of the system under investigation as the scattering function contains all the physics of the target [3].
The following three properties of the scattering function [3] [2] (for the first two properties only the inelastic part of the scattering function is considered) are quite interesting. First of all the principle of detailed balance:

$$S(-\vec{K},-\omega) = \exp(-\hbar\omega/k_BT)\,S(\vec{K},\omega), \tag{2.10}$$

where k_B is Boltzmann's constant and T is the temperature. This property expresses that the transition probability depends on the Boltzmann factor and thus especially on the fact whether an excitation will be annihilated or created. The Boltzmann factor is lower if an excitation is annihilated.

Second, the scattering function is related to the dissipative part of a linear response function via the fluctuation-dissipation theorem:

$$S(\vec{K},\omega) = \frac{\chi''(\vec{K},\omega)}{1-\exp(-\hbar\omega/k_BT)}, \tag{2.11}$$

where $\chi''(\vec{K},\omega)$ is the imaginary part of the dynamical susceptibility.
Third the scattering function can be expressed as space and time Fourier transform of the correlation function $G(\vec{r},t)$, reflecting the fact that the scattering function in general contains information on the position and the motion of the atoms within the sample:

$$S(\vec{K},\omega) = \frac{1}{2\pi\hbar}\int G(\vec{r},t)\exp i(\vec{k}\vec{r}-\omega t)d\vec{r}dt, \tag{2.12}$$

where $\vec{r}$ is the position vector. If a particle of the sample is at $\vec{R}_{l'}$ at the time zero, the correlation function is the probability that another particle l is at $\vec{R}_l = \vec{R}_{l'} + \vec{r}$ at another time t. Hence the correlation function can be expressed through δ-functions in real space:

$$G(\vec{r},t) = \frac{1}{N}\sum_{ll'}\int\langle\delta(\vec{r'}-\vec{R}_{l'}(0))\delta(\vec{r'}+\vec{r}-\vec{R}_l(t))\rangle d\vec{r}. \tag{2.13}$$

The upper formula expresses the correlation of all the pairs of two atoms within the sample and hence the summation is over all these pairs (even self correlation is considered). The brackets reflect the thermal average. Inserting the upper formula in equation 2.12 one gets again the result for the scattering function from equation 2.9.
We are now specifying the sample. We assume that the particles move only in the vicinity of their so-called equilibrium positions which are given by a Bravais lattice. So the possible motions of the particles can be described by lattice oscillations or more precisely as a superposition of the normal modes. Hence the crystal may be modelled as a set of coupled harmonic oscillators. This leads for the atoms of the sample the following position vector:

$$\vec{R}_l(t) = \vec{l} + \vec{u}_l(t), \tag{2.14}$$

where $\vec{l}$ is the time independent equilibrium position of the atoms and $\vec{u}_l(t)$ is the time dependent motion around these equilibrium positions. Inserting this position vector in equation 2.9, one obtains for the scattering function the following expression [3]:

$$S(\vec{K},\omega) = \frac{1}{2\pi\hbar}\sum_l \exp(i\vec{K}\vec{l})\int\langle\exp U\exp V\rangle\exp(-i\omega t)dt, \tag{2.15}$$

with $U = -i\vec{K}\vec{u_0}(0)$ and $V = i\vec{K}\vec{u_l}(t)$. The sum over l and l' could be simplified recognizing that for each value of l' the sum over l is the same and the origin can be chosen arbitrarily at $l' = 0$. Instead of the sum one has to multiply the whole expression by the number of atoms within the sample N. Afterwards the factor $\exp(i\vec{K}\vec{l})$ could be taken out of the integral as it is time and temperature independent.
Using the concepts of the quantum mechanical harmonic oscillator and normal modes one can express U and V in the following way. In general one has to consider all the normal modes depending on q the phonon wave vector and j labelling the three different polarizations. The following calculation is made for one normal mode representing the others. (Each phonon mode is orthogonal and can usually be treated independently within the harmonic approximation) Later the other modes have again to be considered by the appropriate summation.

$$U = -i\vec{K}\vec{u}_0(0) = -i(ca_{\vec{q},j} + c^* a^+_{\vec{q},j}) \tag{2.16}$$

$$V = i\vec{K}\vec{u}_l(t) = i(da_{\vec{q},j} + d^* a^+_{\vec{q},j}), \tag{2.17}$$

with

$$c = \left(\frac{\hbar}{2MN}\right)^{1/2} \frac{\vec{K}\varepsilon_{\vec{q},j}}{\sqrt{\omega_{\vec{q},j}}}, \quad d = \left(\frac{\hbar}{2MN}\right)^{1/2} \frac{\vec{K}\varepsilon_{\vec{q},j}}{\sqrt{\omega_{\vec{q},j}}} \exp i(\vec{q}\,\vec{l} - \omega t), \tag{2.18}$$

where $a_{\vec{q},j} = a_s$ and $a^+_{\vec{q},j} = a^+_s$ are the annihilation and creation operators of the corresponding phonon mode, $\varepsilon_{\vec{q},j}$ is the polarization vector for the corresponding phonon mode, $\omega_{\vec{q},j}$ is the phonon frequency for the corresponding phonon mode and M is the mass of the atom. Instead of the indices for the normal modes $\vec{q}$ and j, s is used as a collective index. According to quantum theory the annihilation and creation operator have the following properties:

$$a_s|n\rangle_s = \sqrt{n}|n-1\rangle_s, \quad a^+_s|n\rangle_s = \sqrt{n+1}|n+1\rangle_s, \tag{2.19}$$

where the operators for different modes commute:

$$[a_s, a^+_{s'}] = \delta_{s,s'}. \tag{2.20}$$

The vectors $|n\rangle_s$ denote the eigenstates of the quantum mechanical oscillator and n is the corresponding eigenvalue. Using the properties of the annihilation and creation operator, one can show that [3]:

$$\langle \exp U \exp V \rangle = \langle \exp(U+V) \rangle \cdot \exp(1/2[U,V]). \tag{2.21}$$

Using the fact that the exponential $(U+V)$ is a Gaussian distribution and that we are in thermal equilibrium we can simplify the former expression to:

$$\langle \exp U \exp V \rangle = \exp \langle U^2 \rangle \cdot \exp \langle UV \rangle. \tag{2.22}$$

Using the above relation and the fact that the factor $\exp\langle U^2\rangle$ is time independent, we obtain for the scattering function (see equation 2.15) the following expression:

$$S(\vec{K},\omega) = \frac{1}{2\pi\hbar}\sum_l \exp\left(i\vec{K}\vec{l}\right)\exp\langle U^2\rangle \int \exp\langle UV\rangle \exp\left(-i\omega t\right)dt. \tag{2.23}$$

Where $\langle U^2\rangle$ is the self correlation function of the time dependent deviation while $\langle UV\rangle$ is the average pair correlation function of the deviation. From $\langle U^2\rangle$ it follows the Debye-Waller factor, whereas from $\langle UV\rangle$ follows the phonon cross section. The factor $\exp\langle U^2\rangle$ is called the Debye-Waller factor, with

$$\langle U^2\rangle = -2W = -\frac{\hbar}{2MN}\sum_s \frac{(\vec{K}\vec{\varepsilon_s})^2}{\omega_s}\coth(1/2\hbar\omega_s\beta) \tag{2.24}$$

the Debye-Waller constant W, $\beta = \frac{1}{k_B T}$ and k_B is the Boltzmann constant.
The integral in equation 2.23 contains the factor $\exp\langle UV\rangle$ which can be expanded by expansion of the e-function:

$$\exp\langle UV\rangle = 1 + \langle UV\rangle + \frac{1}{2!}\langle UV\rangle^2 + ... \tag{2.25}$$

The first term yields the scattering function for elastic scattering (ω=0) for point-like scatterers:

$$S(\vec{K}) = \frac{1}{2\pi\hbar}\sum_l \exp\left(i\vec{K}\vec{l}\right)\exp -2W. \tag{2.26}$$

In general, for arbitrary $\vec{K}$ the phase adds up incoherently and hence the net value of the scattering function is zero. However, if the scattering vector equals a reciprocal lattice vector, then the phases add up coherently and the scattering function becomes finite. This condition is called the Bragg condition and the corresponding scattering peak a Bragg peak. This is a very important scattering condition and therefore it is discussed in the following section (2.4) in some detail.

2.4 Elastic Scattering

In the following section the well-known but important scattering conditions for elastic scattering of neutrons will be stated [4]. But also for inelastic scattering these relations play an important role for example for aligning the sample and in determining spurious contributions to the scattering cross section.
In a scattering experiment there is always an initial wave vector of the neutrons $\vec{k_i}$, which corresponds to the neutron beam which is incident on the sample, and a final wave vector $\vec{k_f}$, which corresponds to the scattered neutron beam. When the neutrons are scattered this process corresponds to a phase difference $\exp[i(\vec{k_f} - \vec{k_i})\cdot\vec{r}]$

(see equation 2.26) between the incident and the scattered beam which is quantified by the difference of the initial and the final wave vector:

$$\vec{K} = \vec{k}_f - \vec{k}_i, \tag{2.27}$$

where $\vec{K}$ is the scattering vector of the experiment.
However, as pointed out in the previous section (2.3), an intense scattered beam only appears if this difference corresponds to a reciprocal lattice vector $G_{hkl} = h\vec{b}_1 + k\vec{b}_2 + l\vec{b}_3$, which is given by the reciprocal lattice, defined by the reciprocal lattice vectors $\vec{b}_1, \vec{b}_2, \vec{b}_3$, of the sample and h, k, l are the Miller indices:

$$\vec{K} = \vec{G}_{hkl}. \tag{2.28}$$

This is the important scattering condition for elastic scattering. If this relation is not fulfilled no Bragg reflection is visible. One visualizes this relationship with the help of the Ewald sphere (see figure 2.1). In this figure at the right the reciprocal lattice vectors are shown. At the left the Ewald sphere is constructed. The vector $\vec{k}_i$ ends at an arbitrary point of the reciprocal lattice. If the circle with radius $|\vec{k}_i|$ crosses another reciprocal lattice point the scattering condition is fulfilled as the difference vector is also a vector of the reciprocal lattice. The vector which points to the second reciprocal lattice point is $\vec{k}_f$. The angle between $\vec{k}_i$ and $\vec{k}_f$ is twice the scattering angle θ.

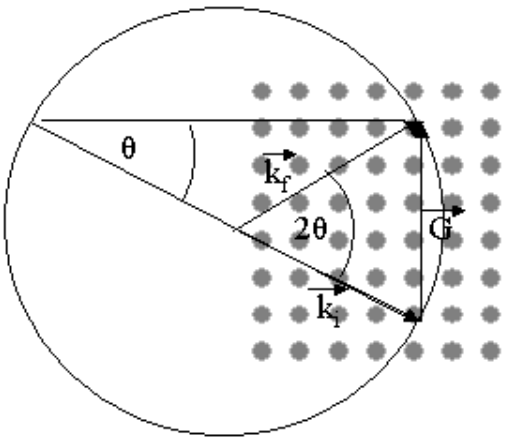

Figure 2.1: Ewald sphere with which the important condition for elastic scattering can be illustrated.

The distance of two scattering planes in real space corresponding to a lattice vector in reciprocal space is given by

$$d_{hkl} = \frac{2\pi}{G_{hkl}}, \tag{2.29}$$

with $G_{hkl} = |\vec{G}_{hkl}|$.
With this relation and $k = |\vec{k}_i| = |\vec{k}_f| = 2\pi/\lambda$ it follows from the scattering condition 2.28 Bragg's law [4]:

$$2d_{hkl} \sin\theta = n \cdot \lambda, \tag{2.30}$$

where λ is the wave length of the neutrons of the electron beam and n is a whole number, it gives the higher order peaks of Bragg scattering. Bragg's law is another way of expressing the scattering condition for elastic scattering.
Bragg's law is a fundamental law of scattering. With this law one can calculate the positions of the nuclear and magnetic Bragg reflections (see section 3.7), and it is also useful for aligning a sample for measurements at a triple-axis spectrometer (see section 5.1).

2.5 Structure factor for nuclear and magnetic scattering

By changing the summation index in equation 2.26 such that one sums up over the atoms in the atomic unit cell and then over all unit cells, one obtains Braggs law and the structure factor for nuclear elastic scattering. In the following formula the sum has been split again: first one sums over the atoms within the asymmetric unit cell, then over the symmetry operators which generate the remaining atoms within the unit cell. In summary one sums over all the atoms in the full unit cell. Then one obtains the nuclear structure factor F_h (also generalized by occupation and anisotropic Debye-Waller factors) which is also used in this form by Fullprof:

$$F_h = \sum_{j=1}^{n} O_j f_j(\vec{h}) \exp(-B_j|\vec{h}|/4) \sum_{s=1}^{m} T_{js}(\vec{h}) \exp\left\{2\pi i(\vec{h}\{S|\vec{t}\}_s\vec{r}_j)\right\} \tag{2.31}$$

where n is the total number of atoms in the asymmetric unit cell, m is the number of the reduced set of symmetry operators (centering lattice translations and inversion center operators removed), j is the index for the jth atom and s for the sth symmetry operator. $\vec{h}$ is a reciprocal lattice vector, $\{S|\vec{t}\}_s$ represents the symmetry operator with $\{S|\vec{t}\}_s = \vec{h}^T S_s \vec{r}_j + \vec{h}^T \vec{t}_s$, $\vec{r}_j$ represents the position vector of the jth atom, O_j is the occupation factor, $f_j(\vec{h})$ is the nuclear form factor, which depends on the shape of the orbitals and hence it depends on the valence state of the ion, $\exp(-B_j|\vec{h}|/4)$ is the isotropic Debye-Waller factor with the isotropic temperature parameter B_j, the anisotropic Debye-Waller factor is $T_{js}(\vec{h}) = \exp\left\{-\vec{h}^T S_s \beta_j S_s^T \vec{h}\right\}$ with the symmetrical matrix β_j representing the anisotropic temperature parameters. If the isotropic temperature factor is refined then the anisotropic temperature parameters are zero. The last term in the upper formula is the phase factor which

depends from the position of the atoms in the nuclear unit cell and from the reciprocal lattice vectors.
The structure factor F_h^2 for a magnetic phase is calculated according to the general formula of Halpern and Johnson [5] (also used by Fullprof):

$$F_h^2 = |\vec{F}_m(\vec{h})|^2 - \left(\vec{e} \cdot \vec{F}_m(\vec{h})\right) \tag{2.32}$$

where $\vec{F}_m(\vec{h})$ is the magnetic structure factor, $\vec{h}$ is the scattering vector, $\vec{e}$ is a unit vector along the scattering vector. The scattering vector can be written as $\vec{h} = \vec{H}+\vec{k}$, where $\vec{H}$ is equal to the reciprocal lattice vector of the nuclear lattice (due to the scattering condition this vector equals $\vec{G}_{hkl}$) and $\vec{k}$ is the propagation vector of the magnetic structure.
The magnetic structures that can be refined with Fullprof must have a distribution of the magnetic moments μ_{lj} that can be developed as a Fourier series:

$$\mu_{lj} = \sum_{\{\vec{k}\}} \vec{S}_{\vec{k}j} \exp\left\{-2\pi i \vec{k} \vec{R}_l\right\}, \tag{2.33}$$

where $\vec{S}_{\vec{k}j}$ is the Fourier component of the magnetic moment, $\vec{k}$ is the propagation vector of the magnetic structure, R_l are the coordinates of the atoms with index l and j is also an index for the atoms.
If the magnetic moment can be expresses as a Fourier series according to equation 2.33, then the magnetic structure factor can be written in the form:

$$\vec{F}_m(\vec{H}+\vec{k}) = p \sum_{j=1}^{n} f_j(\vec{H}+\vec{k}) \vec{S}_{\vec{k}j} \exp\left\{2\pi i (\vec{H}+\vec{k}) \vec{r}_j\right\}, \tag{2.34}$$

where $f_j(\vec{H}+\vec{k})$ is the magnetic form factor. If one considers thermal motion and the symmetry operations, so that the sum is only over the atoms in the magnetic asymmetric unit cell one gets the general equation for magnetic scattering, which is used in the program Fullprof and also given in the Fullprof user manual:

$$\vec{F}_m(\vec{h}) = p \sum_{j=1}^{n} O_j f_j(\vec{h}) T_j^{iso} \sum_s M_{js} S_{\vec{k}j} T_{js} \exp\left\{2\pi i \left[\vec{h}\{S|\vec{t}\}_s \vec{r}_j - \Psi_{\vec{k}js}\right]\right\}, \tag{2.35}$$

where $\vec{h} = \vec{H} + \vec{k}$ is again the scattering vector, $\vec{H}$ and $\vec{k}$ are the lattice vectors of the nuclear and magnetic lattice in reciprocal space. O_j is the occupation factor, $f_j(\vec{h})$ is the magnetic form factor, which depends on the form of the orbital, T_j^{iso} is the isotropic Debye-Waller factor and T_{js} is the anisotropic one. M_{js} is an operator, which transforms the Fourier components $\vec{S}_{\vec{k}j}$ according to the given symmetry. $\{S|\vec{t}\}_s$ is again the symmetry operator which generates from the position of the

atoms $\vec{r}_j$ in the asymmetric magnetic unit cell the whole set of atomic positions in the magnetic unit cell. The first sum over j goes over the magnetic atoms (ions with spin) of the asymmetric magnetic unit cell, whereas s goes over the magnetic symmetry operators. The last term is the phase factor with $\Psi_{\vec{k}js} = \Phi_{\vec{k}j} + \phi_{\vec{k}js}$, where $\Phi_{\vec{k}j}$ is a phase factor which is not determined by the symmetry and $\phi_{\vec{k}js}$ is a phase factor which is determined by symmetry.

2.6 Magnetic structure factor for collinear magnetic structures

In the following section the magnetic structure factor, is given according to the book from Bacon [6]. This gives a more intuitive picture of the magnetic structure factor than the structure factor in the previous section. Bacon gives a magnetic structure factor which is general in that sense that one can calculate arbitrary magnetic models especially the general case of a helimagnetic structure. This formula will be given in this section and then it will be derived from it the magnetic structure factor for collinear magnetic models. This formula can be used in order to get a intuitive understanding under which conditions magnetic Bragg peaks cancel. Using this knowledge can help if one tries to find a correct model for a given data set.
According to Bacon the magnetic structure factor is given by the following formula where $\vec{h} = \vec{h}(h,k,l)$ is the magnetic scattering vector which is equal with the reciprocal lattice vector for magnetic Bragg scattering (this is due to the scattering condition for magnetic Bragg scattering) and for which in general a non zero structure factor is obtained:

$$\vec{F}_m(\vec{h}) = -\frac{e^2\gamma}{mc^2} \sum_n \left[\vec{s}_n - \hat{h}(\hat{h}\vec{s}_n)\right] f_n(\vec{h}) \exp(i\vec{h}\vec{\varrho}_n) \tag{2.36}$$

Where $e^2\gamma/mc^2$ is a constant with m the electron mass, e the electron charge, c is the velocity of light and γ is the magnetic moment of the neutron expressed in nuclear magnetons. n runs over all the magnetic atoms, which are carrying a magnetic moment, within the magnetic unit cell. $\vec{s}_n$ is the spin vector of the nth atom. $\vec{h} = h\vec{a}^* + k\vec{b}^* + l\vec{c}^*$ is the magnetic scattering vector, which defines the scattering plane and $\hat{h}$ is the corresponding unit vector. It is emphasized that even for the magnetic scattering vectors $\vec{a}^*$, $\vec{b}^*$ and $\vec{c}^*$ are also the reciprocal lattice vectors of the nuclear lattice. However that means that the Miller indices for magnetic Bragg reflections are no whole numbers. $f_n(\vec{h})$ is the magnetic form factor and it is determined by the shape of the orbitals in which the electrons bearing the magnetic moments are. $\exp(i\vec{h}\vec{\varrho}_n) = \exp 2\pi i(h\varrho + k\lambda + l\sigma)$ is the phase factor and $\vec{\varrho}_n = \varrho\vec{a} + \lambda\vec{b} + \sigma\vec{c}$ is the position vector of the magnetic atoms in the magnetic unit

cell. Again $\vec{a}$, $\vec{b}$ and $\vec{c}$ are the lattice vectors of the nuclear lattice and ϱ, σ and λ are the relative coordinates of the magnetic atoms. The Debye-Waller factor was omitted for simplicity.
The spin term of the magnetic structure factor can be simplified so that the structure factor reads (see figure 2.2):

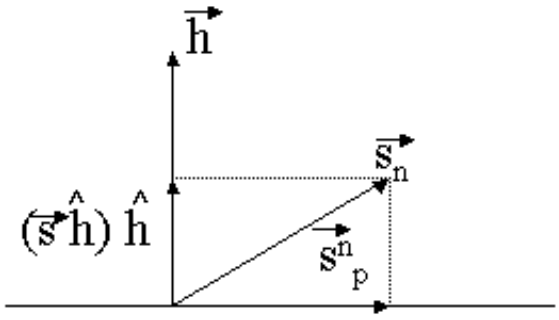

Figure 2.2: The decomposition of the spin vector $\vec{s}_n$ in its component along the scattering vector $\vec{h}$ and its component on the scattering plane $\vec{s}_p^n$. The horizontal thick line at the bottom of the picture is the scattering plane, which is rectangular to the scattering vector $\vec{h}$.

$$\vec{F}_m(\vec{h}) = -\frac{e^2\gamma}{mc^2}\sum_n \vec{s}_p^n f_n(\vec{h}) \cdot \exp(i\vec{h}\vec{\varrho}_n). \tag{2.37}$$

where $\vec{s}_p^n$ is the projection of the spin vector of the nth atom in the magnetic unit cell onto the scattering plane. If the orbitals of the magnetic atoms are equal one can simplify the magnetic structure factor as the magnetic form factors for different atoms are equal $f_n(\vec{h}) = f(\vec{h})$:

$$\vec{F}_m(\vec{h}) = -\frac{e^2\gamma}{mc^2} f(\vec{h}) \sum_n \vec{s}_p^n \exp(i\vec{h}\vec{\varrho}_n). \tag{2.38}$$

The formula above is the general formula in that sense that one can implement an arbitrary magnetic model where every spin has its own coordinates s_p^n. However for collinear magnetic models, that means all the spins are aligned along the same direction the magnetic structure factor can again be simplified. Therefore one uses for the spin component the expression $s_p^n = \sigma|\vec{s}_p|$, where σ_n is $+1$ if the corresponding magnetic atom has spin up or is -1 if the corresponding magnetic atom has spin down. Now the magnetic structure factor reads:

$$\vec{F}_m(\vec{h}) = -\frac{e^2\gamma}{mc^2} f(\vec{h})|\vec{s}_p| \sum_n \sigma_n \exp(i\vec{h}\vec{\varrho}_n), \tag{2.39}$$

with $|\vec{s}_p| = |\vec{s}|\sqrt{1-(\hat{s}\hat{q})^2} = |\vec{s}| \cdot \sin\alpha$ and α is the angle between the scattering vector $\vec{h}$ and the spin vector $\vec{s}_n$.
This magnetic structure factor is consistent with the differential cross section $\frac{d\sigma}{d\Omega}$ for elastic magnetic scattering for an antiferromagnet (collinear magnetic models) in Squires' book [7]:

$$\frac{d\sigma}{d\Omega} \sim |\vec{F_m}(\vec{h})|^2 \sim f^2(\vec{h})|\vec{s}|^2 \left[1-(\hat{s}\hat{q})^2\right] |\sum_n \sigma_n \exp(i\vec{h}\vec{\varrho}_n)|^2, \tag{2.40}$$

where $|\vec{s}|^2$ corresponds to the staggered mean spin $\langle S^\eta\rangle^2$ and η stands for the spin direction in sublattice A. In an antiferromagnet the spin structure consists of two sublattices, one sublattice with spin up and the other sublattice with spin down. Mean staggered spin means, that the average is made over one sublattice and not the whole magnetic structure as then the average would be zero.
In the formula above one recognizes the spin term $[1-(\hat{s}\hat{q})^2]$. This term is zero if the magnetic moments are parallel to the direction of the magnetic scattering vector. That means that for this case the intensity for the corresponding magnetic Bragg reflection cancels. This behavior of the magnetic structure factor can be used for finding the appropriate magnetic model.

Chapter 3

Magnetic measurements on $Na_8Cu_5O_{10}$

The relation between the magnetic and electric properties of copper oxides has recently been the subject of intense research activity. There are two main reasons for that special interest. First the occurrence of high temperature superconductivity is related to magnetism and second usually magnetism and ferroelectricity exclude each other. Therefore, multiferroic materials which show magnetic order as well as ferroelectricity are rare and are especially interesting. In particular, states with collinear and noncollinear magnetic order are currently under discussion in the contexts of ferroelectricity in undoped copper-oxide chain compounds [8] and of the anomalous transport properties of underdoped high temperature superconductors [9, 10]. Since theoretical methods are well established in one dimension, compounds with quasi-one-dimensional electronic structure are particularly suitable as model systems to obtain a detailed understanding of this interplay. However, research on doped copper-oxide chain compounds has been limited by the lack of materials that support a significant density of holes on the chains. Most of the attention has been focused on the "telephone number compounds" $(La,Sr)_{14-x}Ca_xCu_{24}O_{41}$, which contain chain and ladder systems based on edge-sharing CuO_4 square plaquettes [11, 12, 13, 14, 15, 16, 17]. A variety of experiments have revealed intricate charge and spin ordering patterns on the chain subsystem, which depend strongly on the hole content. However, complications originating from the presence of two distinct electronically active subsystems with different hole concentrations and from the random potential of substituents (for $x \neq 0$) partially mask the intrinsic behavior of the copper-oxide chains. Moreover, recent work has shown that the magnetic properties of this material are strongly influenced by an incommensurate structural modulation arising from a mismatch of different units constituting the complex crystal lattice [15, 16, 17]. $Ca_{2+x}Y_{2-x}Cu_5O_{10}$, a class of materials containing only copper-oxide chains, also exhibits a complicated structural modulation unrelated to charge order-

ing [18, 19]. In addition, the magnetic properties of doped chains in this material appear to be influenced to a large extent by substitutional disorder and/or oxygen non-stoichiometry [20].
Therefore the investigation of the magnetic structure in doped spin chain compounds with long range charge order and a commensurate nuclear structure has not been possible so far. However, the current chapter of this PhD thesis is dedicated to the magnetic ground state of a new material which fulfills these special requirements.

3.1 Introduction

Na_xCuO_2, a recently synthesized family of compounds with very low chemical disorder [21, 22, 23]. This material consists entirely of electronically inert Na^+ ions and chains built of edge-sharing CuO_4 plaquettes similar to those in $(La,Sr)_{14-x}Ca_xCu_{24}O_{41}$ and $Ca_{2+x}Y_{2-x}Cu_5O_{10}$ (figure 3.1). Holes donated to the chains by the Na ions form long-range ordered superstructures that are generally incommensurate with the Na sublattice . However, in contrast to other copper oxides with dopable chains, incommensurate structural modulations unrelated to charge ordering are not present, so that commensurate charge order can be established if x is a rational number. By carefully adjusting the chemical synthesis conditions, a state with $x = 1.60$, corresponding to a hole filling factor of 2/5 on the chains, has recently been stabilized [23]. The stoichiometric compound created in this way, $Na_8Cu_5O_{10}$, is a unique testing ground for theories of magnetism in doped copper oxides, without complications arising from substitutional disorder and/or incommensurate lattice distortions.

Our measurements were made with two powder samples. One of the samples turned out to be of better quality and has a mass of 4.5g. The results being reported here were obtained by measurements with that powder sample [21]. Its magnetic susceptibility was found to be in good agreement with prior reports [21, 22]. In particular, a magnetic transition temperature $T_N = 23$ K, between the magnetically long range ordered and the paramagnetic phase, was obtained by analyzing the derivative of the magnetization as a function of temperature.
The atomic positions within the unit cell are displayed in figure 3.1. The unit cell comprises ten copper ions, which are organized in two parallel CuO_2 chains pointing along the *b*-axis. The chains are separated by Na ions. Four of the copper ions in each unit cell (Cu3 in figure 3.5) were found to exhibit bonding patterns characteristic of spin-less Zhang-Rice singlet states with formal valence 3+. The Cu-O bond lengths of the remaining six copper ions indicate a valence state of Cu^{2+} with spin 1/2. The Cu^{2+} ions are located in two inequivalent sites, which are surrounded by two Cu^{3+} ions (Cu1), and one Cu^{3+} ion and one Cu^{2+} ion (Cu2), respectively. Nominally di- and trivalent copper ions are ordered in the sequence 2-2-3-2-3-2-2-3-... along the chains (figure 3.1). The charge order is stable up to temperatures well

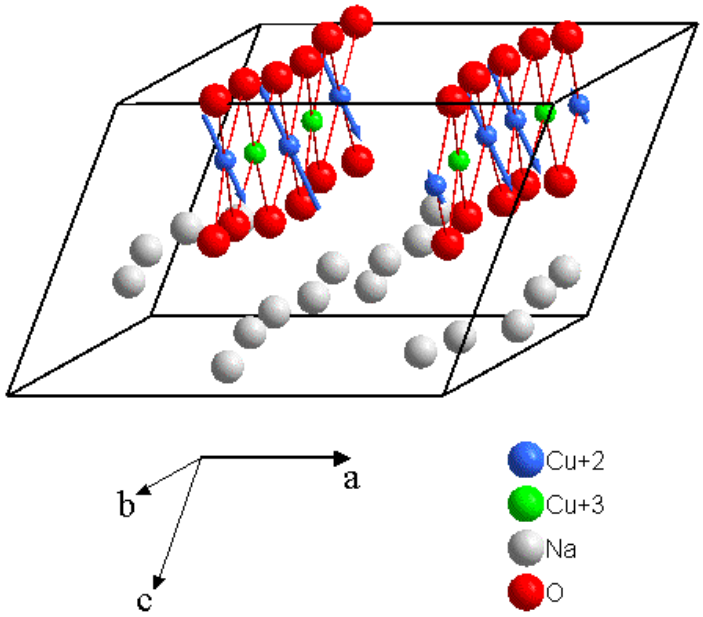

Figure 3.1: Nuclear unit cell of $Na_8Cu_5O_{10}$. The Cu^{2+} ions are blue,the Cu^{3+} ions green, the oxygen ions are red and the sodium ions are grey. This figure shows, that there are two CuO_2-chains within one nuclear unit cell. Within these chains a given sequence of Cu^{2+} and Cu^{3+}-ions leads to charge order. The nuclear structure has space group symmetry C m. The b-axis is running along the chains. The Cu^{2+}-ions bear the magnetic moments which are shown by blue arrows. The green ions are the Zhang-Rice singlets and have (almost) zero magnetic moment. The three-dimensional magnetic structure is determined by the propagation vector (0.5-α, 0, 0.5-β) and the difference of the magnetic phase between of the ions.

above room temperature [21].

3.2 Neutron diffraction measurements at 3 T-2 and Rietveld refinement

As $Na_8Cu_5O_{10}$ is sensitive to air, for the neutron measurements the samples were sealed in air-tight vanadium cans, which were loaded into a helium flow cryostat. The neutron diffraction data were taken at the Laboratoire Leon Brillouin in Saclay, France. In order to determine the nuclear structure, we used the high-resolution diffractometer 3-T-2. For that spectrometer the resolution is optimized for higher angles (ΔQ ($\AA^{-1}$) $\approx$ 0.0125 from 60 degrees to 90 degrees). The incident wave-

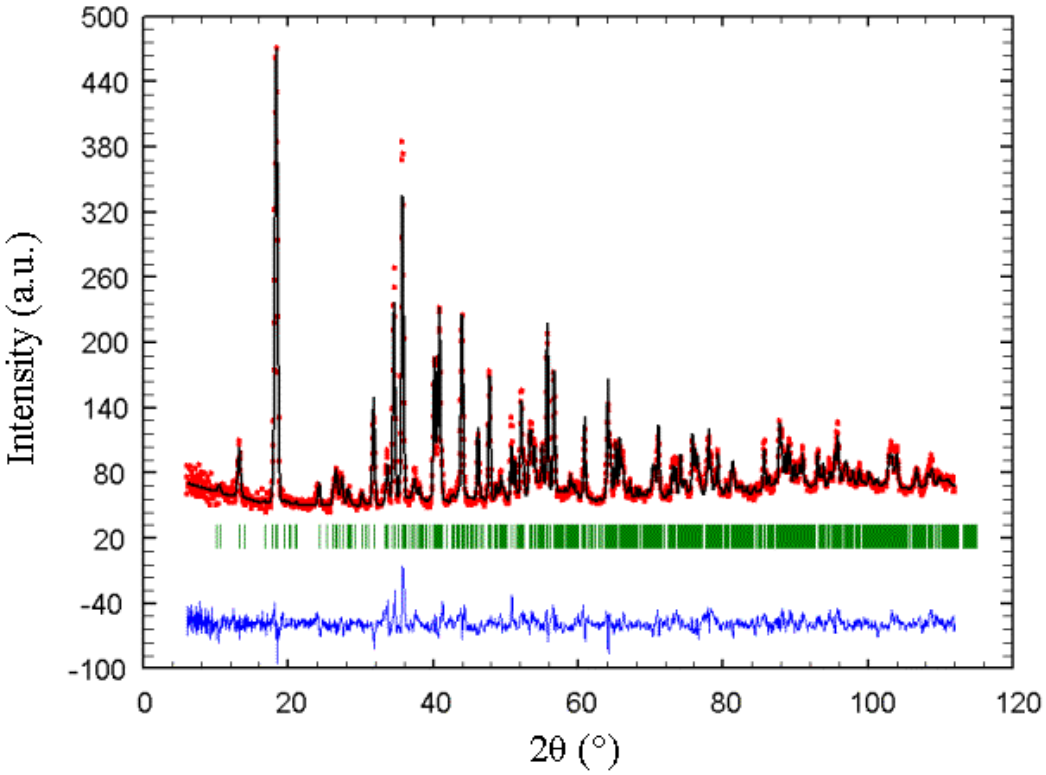

Figure 3.2: Rietveld Refinement of the powder diffraction pattern from our sample made with Fullprof. The black line shows the calculated refinement, whereas the red dots are the measured data. The Bragg reflections are indicated by green lines. The blue curve gives the difference between the calculated and measured intensities.

length was 1.23 $\mathring{A}$. Our measurements were performed at room temperature (around $290K$). Figure 3.2 shows the corresponding high-resolution powder diffraction pattern. The nuclear intensities for both samples were refined with the program Fullprof [24] on the basis of the monoclinic space group Cm. The unit cell parameters $a = 8.23492 \pm 0.00014$Å, $b = 13.92889 \pm 0.00020$Å, $c = 5.71324 \pm 0.00010$Å, and $\beta = 111.91 \pm 0.004°$, the isotropic Debye-Waller factor 1.2478(6) $\mathring{A}^2$ and atomic positions (see table 3.1) obtained from the refinement agree with the results of earlier x-ray diffraction studies [21, 23]. Additionally the asymmetry parameters of the line shape were quite small. The line shape was assumed to be a pseudo-Voigt function, which is a linear combination of a Lorentzian with a Gaussian. The resulting diffraction pattern yields an excellent description of the experimental data (figure 3.2), as indicated by the goodness-of-fit-parameters $R_P = 0.213$, Bragg $R = 0.109$, and $\chi^2 = 0.0473$. This implies that the sample is chemically homogeneous, and that the lattice structure is indeed commensurate. Another sample prepared under

Atom	Wyck.	x/a	y/b	z/c
Cu1	2a	0.30(3)	0.5	-0.16(0)
Cu2	4b	0.26(9)	0.90(5)	0.80(0)
Cu3	4b	0.27(6)	0.70(1)	-0.18(2)
Na1	4b	0.14(6)	0.87(4)	0.19(7)
Na2	2a	0.96(6)	1	0.38(4)
Na3	4b	0.90(7)	0.79(4)	0.42(9)
Na4	4b	0.56(3)	0.86(2)	0.16(5)
Na5	2a	0.44(8)	1	0.45(8)
O1	2a	0.20(0)	1	0.53(8)
O2	2a	0.34(4)	1	0.05(6)
O3	4b	0.25(4)	0.59(5)	0.58(3)
O4	4b	0.31(3)	0.80(5)	0.03(3)
O5	4b	0.23(1)	0.79(5)	0.56(1))
O6	4b	0.33(5)	0.60(7)	0.05(9)

Table 3.1: The refined atomic positions of the ions within the asymmetric unit cell are given in units of the lattice constants $a = 8.23492 \pm 0.00014$Å, $b = 13.92889 \pm 0.00020$Å, $c = 5.71324 \pm 0.00010$Å, and $\beta = 111.91 \pm 0.004°$, which have also been refined. Moreover, the anisotropic temperature (displacement) factor (Biso: isotropic Debye-Waller factor 1.2478(6)) has also been obtained by our refinement.

nominally identical conditions yielded substantially worse refinements, and data on a sample consisting of batches of powder material synthesized in different reactions could only be fitted by a superposition of different charge ordering patterns. These findings show the sensitivity of the nuclear structure to the synthesis conditions.

3.3 Magnetic measurements at G 4-1

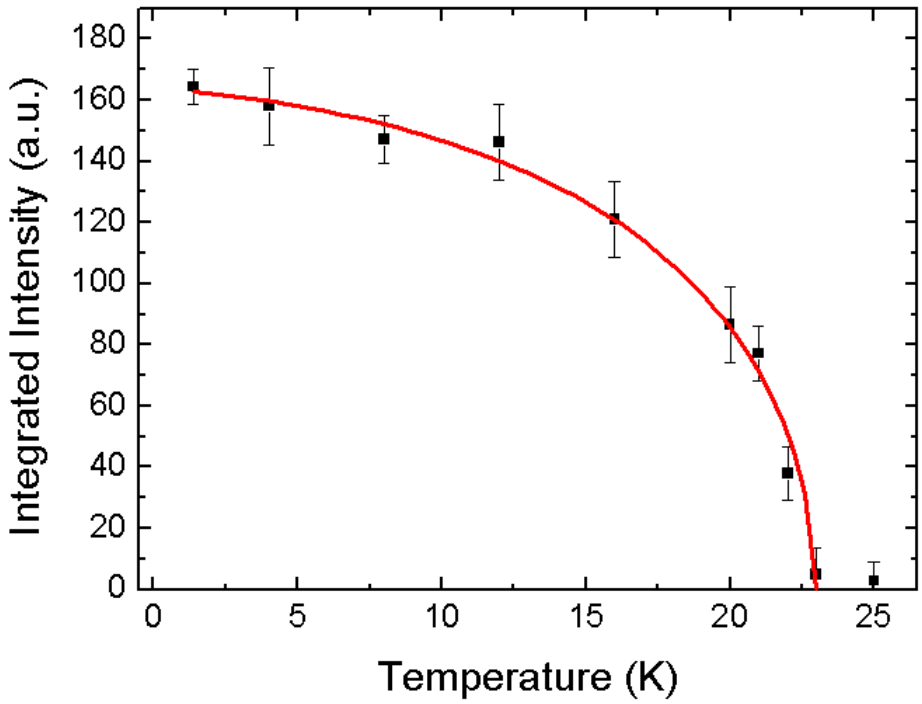

Figure 3.3: Integrated intensities of the ($\mp 0.5 \mp \alpha$, 1, $\pm 0.5 \pm \beta$)- and the (0.5-α, 0, 0.5+β) magnetic Bragg reflection as a function of temperature. The line is the result of a power-law fit. Thus we obtained a transition temperature of 23K.

Our magnetic measurements were taken at G 4-1, a cold neutron two axis spectrometer for magnetic structure determination. The resolution was optimized for small angles (ΔQ ($\mathring{A}^{-1}$) ≈ 0.0065 up to about 20 degrees). The incident wavelength was $\lambda = 2.43$ $\mathring{A}$. With a 800-cell multi-detector, we could cover a 2θ range from 3 degrees up to 82.9 degrees in 0.1 degrees steps. We used a cryostat, so that we could reach temperatures down to 1.4K. Before each measurement the temperature was stabilized for 5 minutes. For our $Na_8Cu_5O_{10}$ powder sample, we took data above and below the magnetic ordering temperature T_N. To obtain the temperature dependent magnetic order parameter, we measured the diffraction patterns

for our sample at 1.4K, and from 4K to 20K in steps of 4K. In order to determine the transition temperature we made three further measurements between 20K and 25K. (For our second sample measurements at 1.4K, 20K and 30K were made.) By comparing the magnetic measurements below and above T_N two magnetic Bragg reflections were identified. Further magnetic Bragg reflections could not be identified above the background. The temperature evolution of the integrated intensity of the ($\mp 0.5 \mp \alpha$, 1, $\pm 0.5 \pm \beta$)- and the (0.5-α, 0, 0.5+β) magnetic Bragg reflection (see figure 3.4) ,is well described by a power-law fit without detectable rounding near $T_N = 23K$ (see figure 3.3), which indicates homogeneous magnetic long-range order in the low-temperature phase. Moreover, the Néel temperature of $23K$ is consistent with our susceptibility measurements.

3.4 Magnetic model for $Na_8Cu_5O_{10}$

The magnetic structure was refined using Fullprof. And our data for $T = 1.4K$ together with this refinement is shown in figure 3.4. The corresponding formula for the magnetic structure factor is explained in section 2.5. The positions of the magnetic Bragg peaks indicate an approximate doubling of the unit cell along a and c, whereas the magnetic and nuclear unit cells coincide along the spin-chain axis b. A systematic shift away from scattering angles corresponding to commensurate Bragg reflections (inset in figure 3.4) reveals that the magnetic structure is incommensurate. The propagation vector resulting from the refinement is $(-0.5+\alpha,\ 0,\ 0.5-\beta)$ with $\alpha = 0.089(3)$ and $\beta = -0.030(1)$ at $1.4K$. The Miller indices of the magnetic Bragg reflections are shown in figure 3.4. The asymmetric lineshape of the magnetic peak at higher scattering angle is well explained as a consequence of the superposition of two resolution-limited, nearly coincident incommensurate Bragg reflections. Although only three inequivalent magnetic Bragg reflections are visible, the diffraction pattern imposes strong constraints on the magnetic structure. Because of the large unit cell and the incommensurate magnetic modulation, most possible spin arrangements generate additional Bragg reflections with intensities well outside the experimental error bars, where none are observed. By far the best agreement with the data ($R_P = 0.245$, Bragg $R = 0.0493$, $\chi^2 = 0.0477$, magnetic $R = 0.114$) was obtained based on a collinear spin structure in which the two Cu^{2+} moments on Cu2 sites directly adjacent along the chains are parallel, whereas Cu1 and Cu2 moments separated by Cu3 ions are antiparallel. The magnetic moment on the Cu3 site was refined to (almost) zero, consistent with the Zhang-Rice singlet state inferred from the bond-length analysis mentioned above [21]. The incommensurate propagation vector perpendicular to the chains modulates the magnitude of the Cu^{2+} moments. The modulation amplitude was refined as $0.84 \pm 0.10 \mu_B$ on both Cu1 and Cu2 sites, consistent with a spin-1/2 state. The spin direction resulting from the refinement

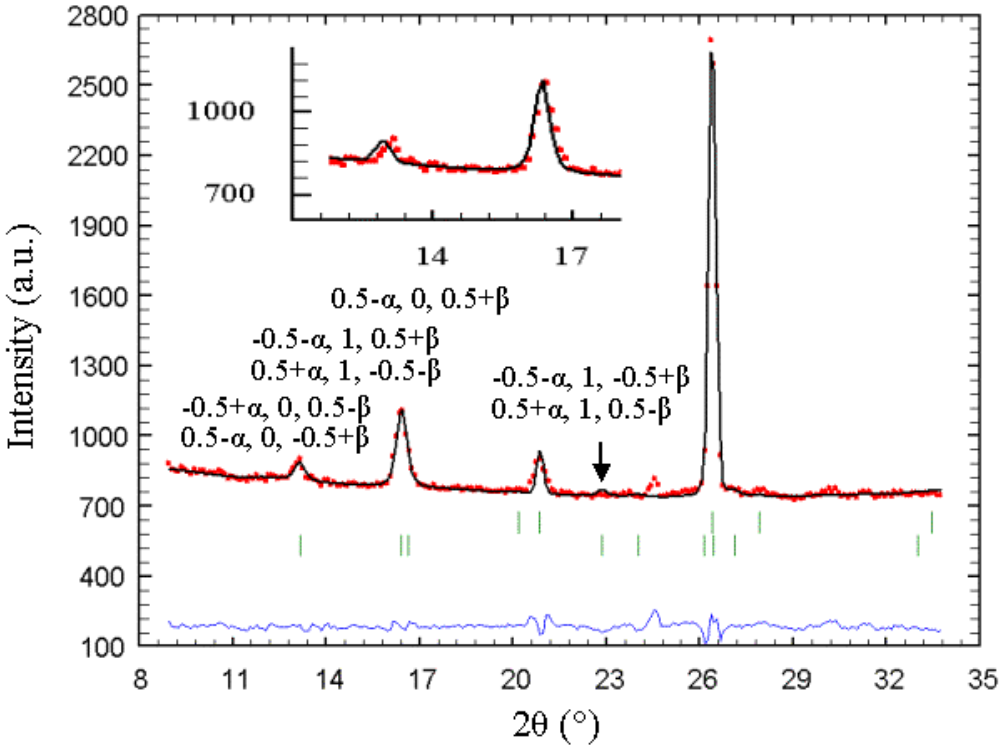

Figure 3.4: The red points show the measured data obtained at G 4-1 for T = 1.4K. The black line shows the Rietveld refinement for our magnetic model, for which the magnetic moments are modulated incommensurably along the a^* and the c^* axis and commensurately along the b^* direction. The green bars indicate the Bragg reflections. The bars in the first line represent the nuclear Bragg reflections and the bars in the second line represent the magnetic Bragg reflections. The observed magnetic Bragg peaks are given according to their Miller indices. The inset shows the same data but with a Rietvield refinement assuming a magnetic model with commensurate wave propagation for all three crystallographic axis. This shows that an incommensurate propagation vector is essential to refine our data properly.

is $(0.86 \pm 0.39, 0, 0.92 \pm 0.07)$, that is, perpendicular to the chains. An additional refinable parameter is the phase difference $\Psi_{12} = 45 \pm 4.5°$ of the modulation on Cu1 and Cu2 sites. The spin arrangement within the nuclear unit cell is displayed in figure 3.1. The corresponding diffraction pattern is in excellent agreement with the data (see figure 3.4).
A comprehensive set of alternative collinear and noncollinear spin structures was also tested, but the resulting refinements were unsatisfactory. In particular, the diffraction patterns of the circular helix structure that yields the best agreement

with the data generates prominent Bragg reflections $(\pm 0.5 \pm \alpha, 1, \pm 0.5 \mp \beta)$ at 22.9°, where the Bragg intensity vanishes within the error (arrow in figure 3.4). The corresponding magnetic R-factor is 0.3541, much worse than that of the collinear state. If the refinement is generalized to include elliptical helix structures, the length of the minor axis of the ellipse ($0.061 \pm 0.165\mu_B$ along b) is consistent with zero, and the magnetic R-factor does not improve significantly compared to the collinear state. Although a small noncollinear component cannot be ruled out, the incommensurate modulation therefore predominantly affects the moment amplitude.

3.5 Discussion

Although the observed spin amplitude modulation is formally analogous to spin density waves in metallic systems, the insulating nature and robust charge order of $Na_8Cu_5O_{10}$ imply that it cannot arise from a Fermi surface instability. We therefore discuss our data in terms of superexchange interactions between local magnetic moments, focusing first on the commensurate spin structure along the chain axis b. The spin alignment along this axis indicates a ferromagnetic nearest-neighbor exchange interaction $J_{\|1}$ and an antiferromagnetic next-nearest-neighbor interaction $J_{\|2}$ (figure 3.5), in agreement with electronic structure calculations for edge-sharing copper-oxide chains [14, 25, 26, 27, 28] and with the conclusions of experiments on a variety of undoped compounds including $LiCu_2O_2$ [29, 30] and $NaCu_2O_2$ [31], which contain undoped chains with similar bond lengths and angles as the ones in $Na_8Cu_5O_{10}$. Since the Cu-O-Cu bond angle in the edge-sharing chain geometry is close to 90°, $J_{\|1}$ is anomalously small, and the competing next-nearest-neighbor coupling $J_{\|2}$ is comparable or larger in magnitude. The undoped spin systems of $(Li,Na)Cu_2O_2$ respond to the resulting frustration by forming incommensurate, helical magnetic order propagating along the chains [29, 31, 30]. In $Na_8Cu_5O_{10}$, charge ordering lifts this frustration and gives rise to a commensurate spin structure along the chains.

The situation is different for interactions between different chains. For simplicity, we first ignore the small incommensurability along c and consider the magnetic bonding pattern in the ab-plane (figure 3.5), including both interactions between directly adjacent chains within the same unit cell ($J_{\perp 1}$, $J_{\perp 2}$) and interactions between next-nearest-neighbor chains ($J_{\perp 3}$). For most sign combinations of these parameters, the inter-chain interactions are frustrated. For instance, the simplest explanation for the approximate doubling of the unit cell along a is that $J_{\perp 3}$ is dominant and antiferromagnetic, leaving the interactions between nearest-neighbor chains frustrated. (We note that ab-initio calculations on $NaCu_2O_2$ indeed yield antiferromagnetic next-nearest-neighbor inter-chain interactions of magnitude comparable to the leading intra-chain coupling [26]). In principle, the spin system can respond

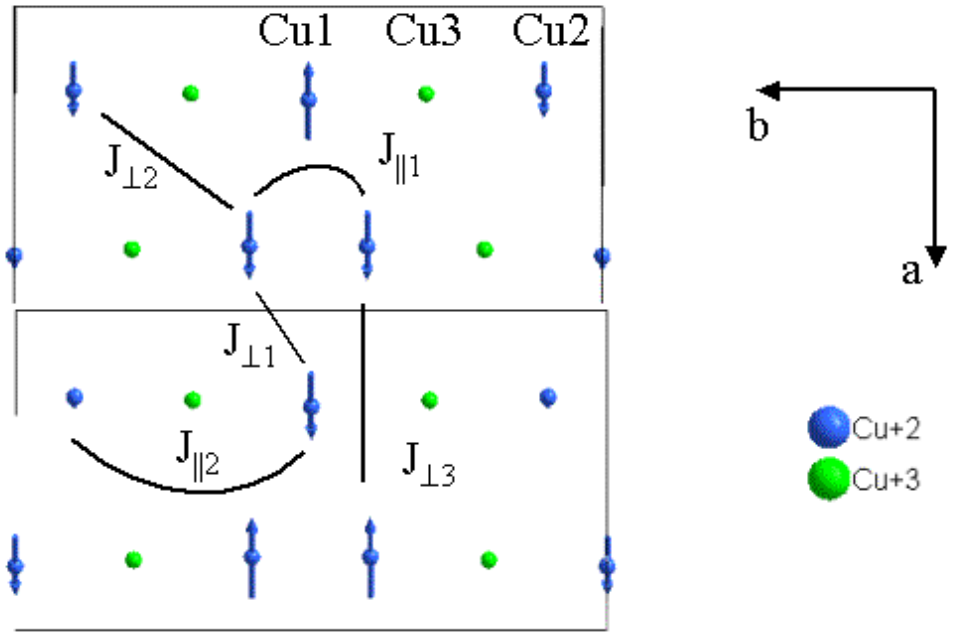

Figure 3.5: Cut of the lattice structure along the *ab* plane, showing two unit cells with inequivalent copper sites. Moreover the nearest and next-nearest neighbor superexchange paths between the spin baring copper ions are shown. Further explanation see text. The spins have been calculated by considering the propagation vector and the phase differences between inequivalent copper ions. As a result one obtains a spin density wave, where the amplitudes of the spins are modulated.

to the frustration by establishing either noncollinear magnetic order, as observed in (Na,Li)Cu_2O_2, or periodic spin-singlet correlations, as found in models of frustrated and/or doped quasi-two-dimensional quantum antiferromagnets [10]. Whereas the neutron diffraction data rule out substantial noncollinearity, an admixture of spin-singlet correlations is a possible mechanism underlying the observed spin density modulation. To obtain a crude estimate of the magnitude of the inter-chain interactions in $Na_8Cu_5O_{10}$ in the framework of this scenario, we consider classical spins coupled by sinusoidally modulated exchange bonds with amplitudes shown in figure 3.5. Minimization of the exchange energy E

$$E = -J_{\parallel 2}\cos\Psi_{12} + 2J_{\perp 1}\cos(\Psi_{12} + \frac{h_x a}{2}) - 2J_{\perp 3}\cos(h_x a) + 2J_{\perp 2}\cos(\frac{h_x a}{2}) \quad (3.1)$$

with respect to the phase shift Ψ_{12} of the modulation on the Cu1 and Cu2 sublattices then yields $J_{\perp 1}/J_{\parallel 2} = \sin\Psi_{12}/2\sin(\frac{1}{2}h_x a + \Psi_{12}) \sim -0.72$, where h_x is the

component of the incommensurate propagation vector along the a-axis determined by the competing interactions between nearest- and next-nearest-neighbor chains. While a full quantum-mechanical calculation is required to assess the viability of this scenario, this simple estimate indicates that the exchange interactions between CuO_2 chains along a are comparable to those within the chains. Similar findings have been reported for other copper-oxide chain compounds [26, 28, 32]. The smaller incommensurability along c suggests weaker exchange interactions in this direction. In view of the helicoidal states observed in the undoped analogues (Li,Na)Cu_2O_2, the collinear spin density modulation in $Na_8Cu_5O_{10}$ may seem surprising. However, as other cuprates with undoped edge-sharing chains exhibit collinear spins [19, 32], the energy balance between both types of order appears to be quite subtle. This is also confirmed by ab-initio calculations [28, 27]. Anisotropic exchange [12, 32] and/or order-from-disorder mechanisms [33] may be responsible for tipping the balance towards collinear order in $Na_8Cu_5O_{10}$.

3.6 Summary

We have determined the magnetic structure of $Na_8Cu_5O_{10}$ below its Néel temperature $T_N = 23$ K by neutron powder diffraction. We find that the spins are collinear and exhibit an incommensurate spin density modulation that is unusual for magnetic insulators. A possible origin is a network of competing inter-chain exchange interactions generated by commensurate charge order. In conclusion, by virtue of their commensurate lattice structure and absence of substitutional disorder, $Na_8Cu_5O_{10}$ and other members of the Na_xCuO_2 family are interesting model systems for theories of frustrated quantum antiferromagnetism in copper oxides [8, 9, 10, 27].

3.7 Magnetic reflections in the monoclinic cell

In section 2.4 Bragg's law $2d_{hkl}\sin\theta = n \cdot \lambda$ was derived. With Bragg's law one can calculate at which scattering angle 2θ the nuclear or magnetic Bragg reflections occur. Therefore one has to calculate the distance of two scattering planes d_{hkl} in real space. This distance depends on the corresponding reciprocal lattice vector $\vec{G}_{hkl}$:

$$d_{hkl} = \frac{2\pi}{\sqrt{\vec{G}_{hkl}^2}}. \tag{3.2}$$

And for the orthorhombic case it is depending on the Miller indices h, k, l and the lattice constants (in real space) a, b, c:

$$d_{hkl} = \frac{1}{\sqrt{\left(\frac{h}{a}\right)^2 + \left(\frac{k}{b}\right)^2 + \left(\frac{l}{c}\right)^2}}. \tag{3.3}$$

As mentioned in section 3.2 $Na_8Cu_5O_{10}$ has the space group C m, that means that it has a monoclinic lattice. In order to calculate the distance d_{hkl} between two scattering planes for the monoclinic case; first of all the scalar product $\vec{G}^2_{hkl}$ will be calculated. Therefore the coordinates (the Miller indices) and the lattice constants will refer to monoclinic coordinates, moreover the monoclinic vectors in real space will be expressed by orthogonal coordinates in order to calculate the scalar product (see figure 3.6):

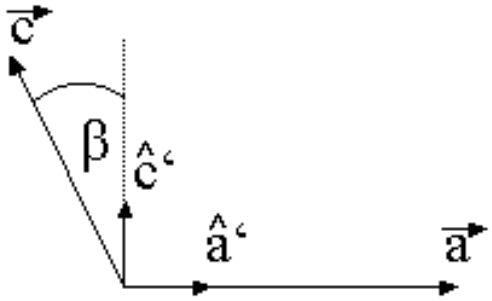

Figure 3.6: The monoclinic plane given by the vectors $\vec{a}$ and $\vec{c}$ is shown. In addition a orthorhombic coordinate system with unit vectors $\hat{a}'$ and $\hat{c}'$ is shown. The angle β of the monoclinic unit cell is shown.

$$\vec{a} = \vec{a}\,' = a\,\hat{a}' \tag{3.4}$$
$$\vec{b} = \vec{b}\,' = b\,\hat{b}' \tag{3.5}$$
$$\vec{c} = c\cos\beta\,\hat{c}' - a\sin\beta\,\hat{a}' \tag{3.6}$$

The reciprocal lattice vectors $\vec{a}^*$, $\vec{b}^*$ and $\vec{c}^*$ are given by their counterparts in real space by the following expression:

$$\vec{a}^* = 2\pi\frac{\vec{b}\times\vec{c}}{V} \tag{3.7}$$

$$\vec{b}^* = 2\pi\frac{\vec{c}\times\vec{a}}{V} \tag{3.8}$$

$$\vec{c}^* = 2\pi\frac{\vec{a}\times\vec{b}}{V} \tag{3.9}$$

whereas the Volume V is given by $V = (\vec{a}\times\vec{b})\cdot\vec{c}$.
Now we will express the reciprocal lattice vectors of the monoclinic lattice by the real lattice vectors of the orthorhombic lattice:

$$\vec{a}^* = \frac{2\pi}{V}\, bc\cdot\cos\beta\,(\hat{b}'\times\hat{c}') - bc\cdot\sin\beta\,(\hat{b}'\times\hat{a}') \tag{3.10}$$

$$= \frac{2\pi}{V}[bc\cdot\cos\beta\,\hat{a}' + bc\cdot\sin\beta\,\hat{c}'] \tag{3.11}$$

$$\vec{b}^* = \frac{2\pi}{V}\, ca\cdot\cos\beta\,(\hat{c}'\times\hat{a}') - ca\cdot\sin\beta\,(\hat{a}'\times\hat{a}') \tag{3.12}$$

$$= \frac{2\pi}{V}\, ca\cdot\cos\beta\,\hat{b}' \tag{3.13}$$

$$\vec{c}^* = \frac{2\pi}{V}\, ab\cdot(\hat{a}'\times\hat{b}') = \frac{2\pi}{V}\, ab\cdot\hat{c}'. \tag{3.14}$$

Now we will calculate $\vec{G}^2_{hkl}$ with $\vec{G}_{hkl} = h\vec{a}^* + k\vec{b}^* + l\vec{c}^*$ and the volume of the unit cell $V = abc\cdot\cos\beta$:

$$\vec{G}^2_{hkl} = (h\vec{a}^* + k\vec{b}^* + l\vec{c}^*)(h\vec{a}^* + k\vec{b}^* + l\vec{c}^*) \tag{3.15}$$

$$= \left(\frac{2\pi}{V}\right)\left[h^2(b^2c^2\cdot\cos^2\beta + b^2c^2\sin^2\beta) + ...\right] \tag{3.16}$$

$$\left[... \, 2hlab^2c\cdot\sin\beta + k^2c^2a^2\cdot\cos^2\beta + l^2a^2b^2\right] \tag{3.17}$$

$$= \left(\frac{2\pi}{V}\right)\left[h^2b^2c^2 + k^2c^2a^2\cos^2\beta + l^2a^2b^2 + 2hlab^2c\sin\beta\right] \tag{3.18}$$

$$= (2\pi)^2\left[\frac{h^2}{a^2\cos^2\beta} + \frac{k^2}{b^2} + \frac{l^2}{c^2\cos^2\beta} + 2hl\frac{1}{ac}\frac{\sin\beta}{\cos^2\beta}\right] \tag{3.19}$$

That means that the distance between two scattering planes in real space d_{hkl} follows:

$$d_{hkl} = \frac{1}{\sqrt{\left[\frac{h^2}{a^2\cos^2\beta} + \frac{k^2}{b^2} + \frac{l^2}{c^2\cos^2\beta} + 2hl\frac{1}{ac}\frac{\sin\beta}{\cos^2\beta}\right]}} \tag{3.20}$$

Now one can calculate with Bragg's law the positions of the magnetic Bragg reflections. This was done for all three magnetic Bragg reflections of $Na_8Cu_5O_{10}$ (section 3.4). We obtained values in accordance with the calculations with Fullprof.

Chapter 4

The Triple-Axis Spectrometer

The main parts of a triple-axis spectrometer are the three spectrometer axes, the monochromator axis, analyzer axis and the sample axis. During each experiment these are the axes which are changed in order to obtain the right experimental conditions. Besides, it consists of other important elements as the monochromator and the analyzer crystal, energy filters, collimators, detectors and the shielding. The very good book from Shirane et al. [2] was used as a basis in order to describe all parts of a triple-axis spectrometer.

4.1 Shielding

As the moderation of the neutrons is not perfect, there are fast neutrons and in addition to these dangerous γ-rays which have to be shielded. To slow the neutrons down one uses iron or hydrogen in different forms and finally cadmium in order to absorb the low-energy neutrons. In order to absorb the γ-rays one uses significant amount of lead. As the fast neutrons need a lot of collisions to slow down the shielding of the monochromator is bulky and usually consists of a large drum filled with scattering and absorbing materials. The shielding around the analyzer, the sample and the detector can be more compact as the number of fast neutrons reaching these instruments is much lower. However besides the massive shielding the monochromator and also the analyzer and the detector must still rotate smoothly and accurately in order to ensure that precise measurements can be made [2].

4.2 Monochromator and analyzer

Apart from the source it is mostly the monochromator which determines the intensity of the neutron beam on the sample. It selects a very narrow range of wave lengths according to Bragg's law. So this very narrow range of wavelengths depends

on the separation of the crystallographic planes d_{hkl} of the monochromator crystal. However, if one uses a perfect single crystal as monochromator crystal the divergence, of the reflected beam would be to small for an acceptable beam intensity. Hence one uses monochromator crystals with a certain mosaicity, that means that the crystal consist out of small crystallites which have a certain, small misorientation with respect to each other. The distribution of these misorientations of the crystallites is assumed to be Gaussian:

$$W(\Delta) = \frac{1}{\sqrt{2\pi}\eta} \; e^{\frac{-\Delta^2}{2\eta^2}} \tag{4.1}$$

where Δ is the misorientation of a crystallite with respect to the crystallite with averaged misorientation and η is the width of the Gaussian distribution function, which gives a measure for the mosaicity. A single crystal being used as a monochromator crystal should not only have a certain mosaicity but should have a negligible absorption. Such crystals are called ideally imperfect crystals. For diffraction, meaning that Bragg's law is valid, of the neutron beam at a large flat monochromator, which is made of an ideally imperfect crystal, Shirane et al. [2] gives in his textbook two different kinds of reflectivity. First the so called peak reflectivity R_p and second the integrated reflectivity R_i. Then the peaked reflectivity is given by

$$R_p = \frac{R_0}{1 + R_0} \tag{4.2}$$

where

$$R_0 = \frac{Q_c t_0}{\sqrt{2\pi}\eta \sin\theta_B} \tag{4.3}$$

and

$$Q_c = \frac{\lambda^3 F_N^2}{v_0^2 \sin 2\theta_B} \tag{4.4}$$

with Q_c the crystallographic quantity, t_0 the thickness of the monochromator, η the monochromator mosaicity, θ_M the scattering angle from Bragg's law, λ the neutron wave length, F_N the static nuclear structure factor and v_0 the unit-cell volume. And the integrated intensity is given for large values of R_i

$$R_i = 0.96\sqrt{\frac{Q_c t_0}{\eta \sin\theta_M}}. \tag{4.5}$$

And if a white beam is used the λ dependent integrated intensity is given by

$$R_\lambda = R_0 \lambda \cot\theta_M. \tag{4.6}$$

For the monochromator the integrated reflectivity is applicable whereas for the analyzer the peaked intensity is appropriate.

In order to get a high beam intensity the monochrometer should have a large crystallographic quantity Q_c making the reflectivity high (4.3). That implies (see equation 4.4) for the monochromator material a large structure factor F_N meaning a big scattering length and a small unit-cell volume v_0. In order to keep the background low in an inelastic scattering experiment a large Debye temperature meaning a more or less rigid lattice and a low incoherent scattering cross section σ_{inc} or more precisely a low relation between incoherent and coherent scattering cross section $\sigma_{inc}/\sigma_{scat}$ are desirable. In addition the absorption of neutrons of the material should be low. There are various materials with good monochromator properties. For example Nickel and Beryllium, however with these materials it is difficult or expensive to prepare good monochromators. Other good materials are PG (pyrolytic graphite) and copper. The properties of these materials being important for the use as a monochromator are summarized in the following table, where a and c are the lattice constants [2]:

material	structure	a ($\AA$)	c ($\AA$)	(hkl)	F_n/v_0 ($10^{11}cm^{-2}$)	$\sigma_{inc}/\sigma_{scat}$ ($percent$)
Nickel	fcc	3.52394		(220)	1.316	0
Beryllium	hcp	2.2854	3.5807	(002)	0.962	0.02
				(110)	5.4985	
PG	layer	2.4612	6.7079	(002)	0.734	0.02
				(004)	3.7467	
copper	fcc	3.61509		(220)	0.653	6.8

In general single crystals of the materials above are not ideally imperfect meaning that their mosaicity is too low. This means that the angular width of the reflected beam (the beam divergence) would be to small in order to get an acceptable beam intensity. Hence it is important to increase the mosaicity for these materials before using them as monochromators for example by introducing dislocations within the crystal. This is a complicated process as the reflected beam should maintain a Gaussian shape. In summary the intensity on the sample depends on two main properties of the monochromator, the peak intensity and the mosaicity. PG (pyrolytic or oriented graphite) is a very good monochromator material as it has good reflectivity properties and it has an appropriate mosaicity. Pyrolytic graphite has oriented (00l) planes, whereas other planes in general (hkl) are oriented randomly and generate powder like diffraction patterns. The orientation of the (00l) planes is good enough to obtain a high reflectivity but leads moreover to a certain mosacity. One can obtain a peak reflectivity of around 80 per cent for low energies, a mosaicity $\eta = 0.56°$ and an absorption of less then 2 per cent [2]. The peak reflectivity decreases for higher energies because of double Bragg scattering for the following reasons. If one uses PG as a monochromator crystal one uses for example the (002) reflection of the oriented layers. That means the (000) and the (002) point in recip-

rocal space determine the Ewald sphere for low energies. Hence the Ewald sphere is small but increases for neutrons with higher energies, that means that higher Bragg reflections for example (112) and (114) are also lying on the Ewald sphere. Thus two or more reflections fulfill the scattering condition simultaneously. This is called double Bragg scattering. According to Bragg's law the scattering angles of the other Bragg reflections are in general not the same as for the (002) reflection and thus the intensity decreases if double Bragg scattering occurs. Furthermore in PG these higher order reflections are powder like and hence they are represented by rings in reciprocal space. That means the reflected intensity is further lowered for higher energies (for PG around 60 per cent at 40meV and 80 per cent at 5meV) [2].
In order to increase the intensity on the sample further one can focus the beam (see figure 4.1). Focusing the beam does not only increase the intensity on the sample

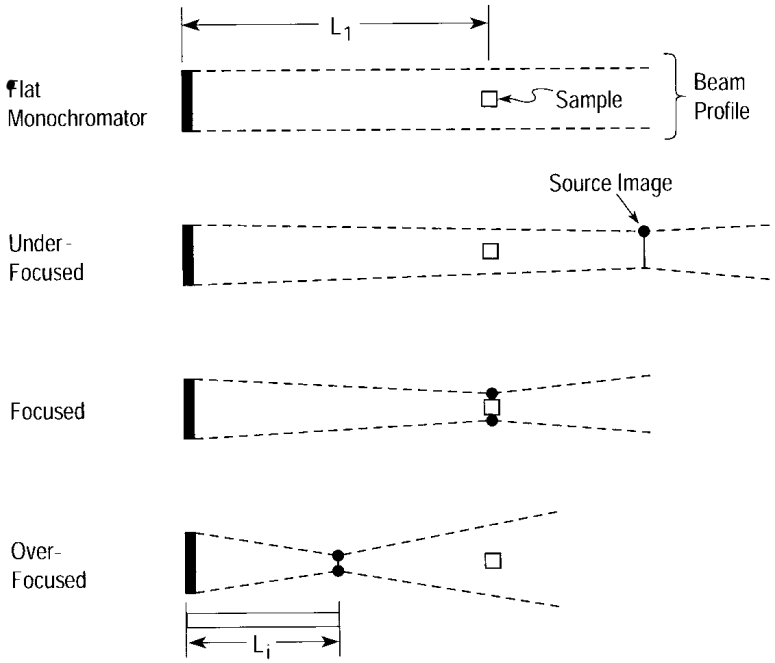

Figure 4.1: Behavior of the beam depending on the degree of focusing. For $L_i = L_1$ the monochromator is focused and the beam performs the maximum intensity on the sample. From Shirane et al. [2], page 66.

but also effects the resolution. The resolution of the momentum transfer component perpendicular to the scattering plane is decoupled from the resolution components within the scattering plane and from the energy resolution. Within the scattering plane a good resolution is required. Therefore vertical focusing (see figure 4.1), which affects only the resolution perpendicular to the scattering plane, is more commonly used (see resolution parameters in chapter 6.9.1). The effects of vertical focusing on

the in-plane resolution of the momentum transfer and on the energy resolution have been tested experimentally with a perfect single crystal and it has been found that this effect can be neglected as the line width change was around 2 per cent [2]. For vertical focusing the monochromator is bent vertically and within the framework of geometric optics it can be approximated as a cylindrical mirror. If the source to monochromator distance is L_0 and the curvature of the monochromator is R then the image of the source will be at a distance L_i and the following relation will apply [2]

$$\frac{1}{L_0} + \frac{1}{L_i} = \frac{2 \sin \theta_M}{R}. \tag{4.7}$$

Where θ_M is the scattering angle of the diffracted beam. The focusing condition is obtained if the image is located at the sample. That means $L_i = L_1$, where L_1 is the monochromator to sample distance. If the beam is focused that means that the beam intensity is maximal at the sample.
Focusing the analyzer crystal means that one maximizes the intensity at the detector and hence a detector with a smaller size can be used. This is an advantage as the signal to background ratio is improved.

4.3 Collimators

The moderated, emitted neutrons from the reactor core do not have a common direction, they emerge in all possible directions. The monochromator and analyzer reflect only neutrons propagating in a narrow range of directions and they influence the beam divergence for example by focusing. However, it may be helpful to have additional control of the beam divergence. The beam divergence can be controlled in the horizontal scattering plane by so-called Soller collimators [34]. A Soller collimator consists of parallel absorbing plates of length L and height h. The plates are separated by a distance a. The transmission function is triangular with a FWHM of $\alpha = \frac{a}{L}$ in the horizontal plane and $\beta = \frac{h}{L}$ in the vertical plane. The efficiency of a Soller collimator depends on the following factors [2]

1. the uniformity of the spacing of the blades throughout the collimator
2. the neutron absorption cross section of the blade material
3. the thickness of the blades
4. the straightness of the blade edges at the entrance and exit to the collimator.

A high efficiency Soller collimator was developed by Carlile et al. [35] consisting of thin plastic films stretched by a metal frame. These plastic films are coated with a gadolinium oxide which has a big neutron absorption coefficient. These

collimators fulfill the conditions listed above. Especially the collimation may be very fine as the blades are quite thin and hence the distance a between the blades may be very small without losing too much intensity. In fact these collimators have a high transmission. The peak transmission of the triangular transmission function exceeds 95%. In general a collimator is used to control the beam divergence but it is also possible to use a triple-axis spectrometer without collimators. Then the beam divergence is determined by the monochromator and the analyzer.

4.4 Filters

According to Bragg's law (see equation 2.30) the angle of the diffracted beam depends on the ratio $\lambda/2d_{hkl}$. If a higher order reflection (nh, nk, nl) with $d_{nh,nk,nl} = d/n$ is also allowed, neutrons with a different energy and wavelength λ/n will be diffracted at the same angle. The corresponding reflections are called higher order reflections. As they can disturb the measured spectra it is important to have filters in order to suppress these reflections.
The total neutron cross section which gives a measure for the attenuation of the direct neutron beam by a certain material is given by [2]

$$\sigma_N = \sigma_{abs} + \sigma_{el} + \sigma_{inel}, \tag{4.8}$$

where σ_{abs} is the cross section due to nuclear capture processes due to strong resonances of the nuclei, σ_{el} is the cross section for elastic scattering and σ_{inel} corresponds to inelastic neutron scattering. According to Bragg's law the maximal wavelength that can be elastically scattered is $\lambda_{cutoff} = 2d^{max}_{h,\,k,\,l}$. Where $d^{max}_{h,\,k,\,l}$ is the maximal spacing of the crystal. For poly-crystalline samples there is a steep increase of the elastic cross section above λ_{cutoff}. Due to multi phonon processes the inelastic neutron cross section increases with energy.
Three-axis instruments are typically used in the thermal energy range. However, there are also a lot of high energy or fast neutrons which contribute to the background. In newer reactors one uses tangential beam tubes and heavy-water moderators which reduce the number of fast neutrons. In some older reactors or if the beam tubes look more directly at the core one needs fast neutron filters to eliminate the large number of fast neutrons in order to reduce the background. Filters for fast neutrons use the inelastic neutron cross section σ_{inel} of certain materials in order to attenuate the flux at high energies. Various materials can be used as fast neutron filters: Bi, Si, quartz (SiO_2) and sapphire (Al_2O_3). For a high quality sapphire crystal Tennant [36] measured the transmission and got the following results: the transmission is high and varies slowly in the thermal ($5 < E_i < 100meV$) and cold ($0.1 < E_i < 10meV$) energy range. For fast neutrons ($E > 500meV$) the transmission is less than 3%. Cooling the crystal has only a small effect on the transmission.

This material is a useful material in order to reduce the flux of fast neutrons and it is better than quartz and silicon.
All nuclei have strong resonances given by their nuclear structure. This effect can be used in order to build $\lambda/2$ and $\lambda/3$ filters. Due to their resonances these materials have a a high absorption cross section for $\lambda/2$ and a low absorption cross section for λ.
Higher order reflections can also be attenuated by so-called Bragg scattering filters. These filters use the steep increase of σ_{el} at the cutoff wavelength $\lambda_{cutoff} = 2d^{max}_{h,\,k,\,l}$. Freund and Forsyth [37] gave the cutoff energies for different materials. These materials are used in the poly crystalline form as the orientation of the Bragg reflections is of no concern for the cutoff energy and hence for the use as a filter. Two useful materials for Bragg scattering filters are Be and BeO with cutoff wavelengths (energies) of $4.0\mathring{A}$ and $4.7\mathring{A}$ ($5.2meV$ and $3.7meV$), respectively. For smaller wavelength with respect to the cutoff value and for higher energies these materials can be used in order to filter higher order reflections. Another very useful material in order to filter higher order neutrons is PG (pyrolytic graphite). A PG filter is placed in the beam with its c-axis parallel to the beam. Thus Bragg scattering can occur for certain reflections and the corresponding neutrons are scattered out of the beam. Figure 4.2 presents the transmission [38] for neutrons travelling parallel to the c-axis for a 5-cm-thick piece of PG. It shows the transmission for the desired

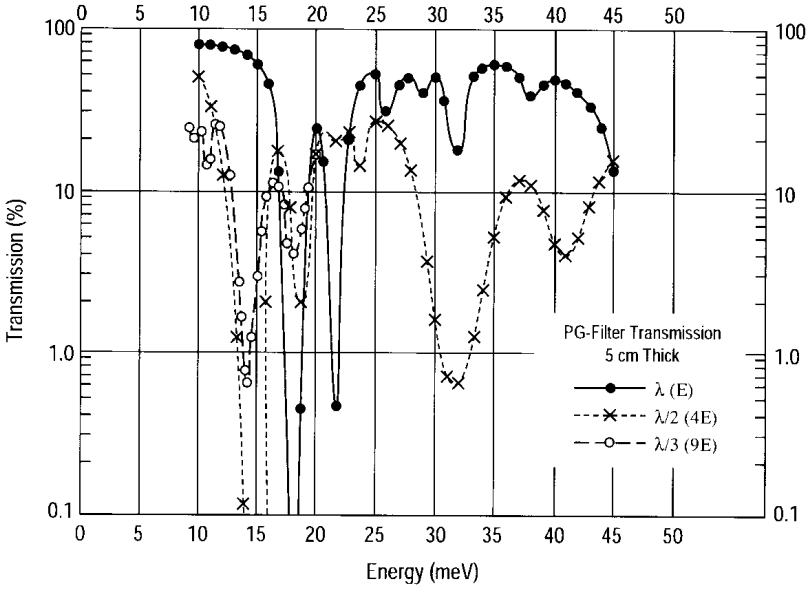

Figure 4.2: Transmission of a 5-cm-thick PG filter as a function of energy for the desired energy E, $4E$ and $9E$. From Shirane et al. [2], page 82.

energy E (wavelength λ) and the corresponding transmissions for the higher orders, namely $4E$ ($\lambda/2$) and $9E$ ($\lambda/3$). Desirable is a large transmission for λ and a low transmission for $\lambda/2$ and $\lambda/3$. It was shown by Shirane and Minkiewicz [39] that reducing the mosaicity, improves the transmission for λ and the attenuation for $\lambda/2$. This was shown with a 2-cm-thick PG filter with a mosaic width of 3.5 degrees and 6.5 degrees. The transmission for $\lambda = 2.44\mathring{A}$ decreased from 75% to 50 % and the transmission for $\lambda/2$ increased from 0.07 % to 5 %. It is often useful to apply a second filter in order to check whether a given signal of the beam is intrinsic or whether it is due to second (higher) order contamination. If the intensity decreases substantially with the use of a second filter it is due to higher order neutrons.

4.5 Absorbers

The most commonly used absorber for neutron experiments is Cadmium, which is easily pliable and has a high absorption cross section for neutrons. Therefore it can be easily used in order to shield experimenters from harmful stray neutrons. However one has to consider that neutron absorption leads to emission of γ-rays. Other materials commonly used as neutron absorbers are Gd_2O_3 and borated plastic or glass.

4.6 Spectrometer alignment

First the spectrometer must be aligned in a series of steps. The center lines of the Soller collimators must intersect the centers of rotation of the monochromator, the sample and the analyzer. This can be done best with an optical method. This step is called the optical alignment.
Second, one has to align the three spectrometer axes in a systematic approach in order to avoid correlated errors. This step is called the experimental alignment.
As a first step of the experimental alignment the monochromator has to be aligned. Therefore the nominal positions of the sample and analyzer angles ($2\theta_S$ and $2\theta_A$) are set to their nominal zero positions. The analyzer should be rotated to an angle where it is not reflecting, so that the detector looks directly into the beam reflected from the monochromator. A single horizontal collimator should be placed between the monochromator and the sample table. Collimation restricting the vertical divergence should be placed after the sample. If one makes sure that the detector is not saturated one can open the shutter and rotate the monochromator along its vertical and horizontal axes in order to maximize the intensity. This should be done iteratively.
The next step is to operate the spectrometer in a two-axis mode, with one (hori-

zontal) collimator after the sample. A standard, Q-independent scatterer should be placed as a sample. Therefore one can use for example a poly-crystalline vanadium sample with $2\theta_S \sim 2\theta_M$ (where θ_M is the scattering angle of the monochromator) and the detector should be placed at a nonzero position. The translation of the monochromator is checked by measuring the scattering intensity as the vanadium sample is translated across the beam. The peak-intensity position marks the beam center and should coincide with the center of rotation of the sample axis. If they don't coincide the monochromator should be translated to bring them into coincidence.
If one is satisfied with the monochromator alignment one should simultaneously calibrate the incident wave vector and check for an offset in $2\theta_S$. This is performed with a poly crystalline sample with known lattice spacing and with at least three Bragg reflections, such as the vanadium sample already used in the previous alignment step.
The instrument is now aligned for two-axis operation. The next procedure would be to place the sample in its position and align it by using two orthogonal reflections. This procedure will be explained in detail in section 5.1.
The last step is to adjust the analyzer. The analyzer can be aligned either from the beam of a properly aligned sample or from the direct beam of the monochromator. The procedure is the following: First, the analyzer is rocked to find the position of maximum intensity, and the analyzer angle θ_A is adjusted to correspond to this position. Then the analyzer crystal and the detector arm are scanned together in $\theta_A - 2\theta_A$ mode, meaning a longitudinal scan for the analyzer is being performed, and any necessary adjustment in the value of $2\theta_A$ is made.

4.7 Goniometers

For neutron measurements at a triple-axis instrument there is commonly used a two-circle goniometer, on which the sample is mounted. It consists of two tilt stages which allow the rotation of the sample around two orthogonal axes. These stages are used in order to align the sample. For aligning the sample one uses two orthogonal reflections with the corresponding reciprocal lattice vectors along the upper and the lower stage of the goniometer. Then it is important to align first he upper stage and then the lower one.

4.8 Detectors

In order to detect neutrons a nuclear reaction is necessary, as the neutron has no net electric charge and therefore does't react with matter in that sense that it is

ionizing. There are proportional counters and scintillation detectors, the later are better suited for higher counting rates whereas proportional counters are better suited for lower counting rates [1].
In the following a proportional counter is shortly explained. This detector uses ^3He or BF_3 gas enriched with ^{10}B, which is under pressure. This gas is used as an absorbing gas for the nuclear reaction, which yields charged particles. For the ^3He detector the nuclear reaction of a neutron with the ^3He atom yields tritium and a high energetic proton ($\sim 0.57MeV$). This proton or the charged particles from another nuclear reaction ionizes the gas and the resulting electrons ionize more gas. Thus one obtains a discharge at a high voltage of around $2 - 4kV$. This charge is proportional to the initial energy of the charged particles produced by the nuclear reaction and can therefore be discriminated from the smaller signal from γ-radiation. The counting time is limited due to the collection of the ions and the electronics of the preamplifier. The main advantage of a proportional counter is the high efficiency for thermal neutrons. The efficiency η of a ^3He detector is

$$\eta \propto (1 - \exp(-N\sigma_a d)) \,, \tag{4.9}$$

with N the number density of the ^3He atoms, σ_a the absorption cross section and d the thickness of the detector. If one would produce detectors with very high efficiencies for thermal neutrons fast neutrons ($E > 0.6eV$) would also be detected. As one tries to avoid this a detector efficiency $\eta_{thermal}$ for thermal neutrons of 80 % is a good compromise as then fast neutrons are detected more unlikely.
As the neutrons are scattered in several directions it is a loss of intensity not to have more detectors in several directions. Therefore multi detectors are used, especially for elastic measurements. One can use several detectors with a certain angular distance between them. For the case of gas detectors one can also use a multi detector with several wires in order to improve the angular resolution.

Chapter 5

Inelastic neutron scattering with a triple-axis spectrometer

5.1 Sample alignment

After the spectrometer (monochromator and/or analyzer) is aligned one can align the sample (see 4.6). This is done in the two axis mode of the spectrometer. The following scheme of a triple-axis spectrometer (see figure 5.1) helps to understand the following discussion how a sample is aligned. The monochromator selects by

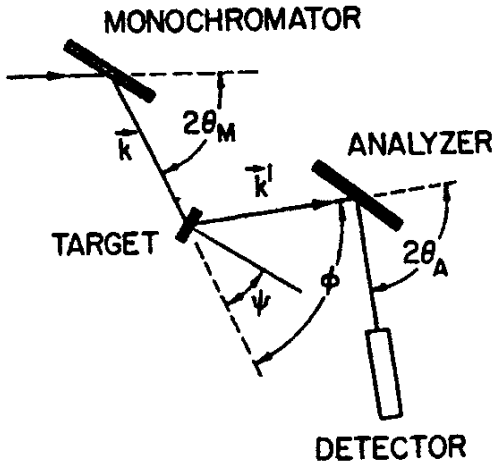

Figure 5.1: Scheme of a triple-axis spectrometer for inelastic neutron measurements [3]. The angles are explained in the text.

Bragg scattering from the thermal neutron beam the neutrons with the propagation vector $\vec{k}$ and scatters them under the angle $2\theta_M$. These neutrons compose the incident beam on the sample with $\vec{k} = \vec{k_i}$. The sample scatters the neutrons under

the angle $2\theta = \Phi$. The angle Ψ is the angle between the incident neutron beam and a reciprocal lattice vector of the sample. The analyzer scatters the neutron beam again under the angle $2\theta_A$. Finally the neutron beam reaches the detector.
Before aligning the sample the spectrometer is set to the two-axis mode and driven

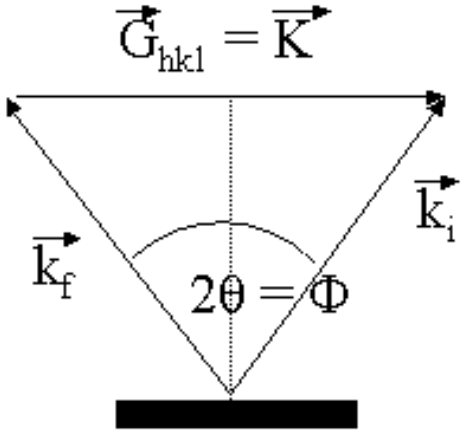

Figure 5.2: Elastic scattering condition (Bragg condition) which must be fulfilled, so that the sample is aligned properly.

to a 2θ angle, where a well observable Bragg reflection is expected. This angle can be checked by hand and by the use of Bragg's law. The next step is to bring the scattering plane of the sample, in which the reciprocal lattice vector G_{hkl} is laying, in coincidence with the scattering plane of the spectrometer, which is being defined by the scattering vector $\vec{K}$ and the propagation vectors $\vec{k_i}$ and $\vec{k_f}$ (see figure 5.2). This is been done by aligning two reciprocal lattice vectors of the sample to the two goniometers (see figure 5.3). For orthorhombic samples this is especially easy, as then the reciprocal lattice vectors are along the crystallographic axis of the sample. Afterwards one has to change the angle Φ (turning the sample) such, that the Bragg condition $\vec{G_{hkl}} = \vec{K}$ for the Bragg peak to which the spectrometer was driven is fulfilled. If this Bragg peak is found in principle the sample is aligned. By tilting the sample (for both reciprocal lattice vectors) with the corresponding goniometer on a corresponding Bragg reflections, one optimizes the intensity of the Bragg reflection and hence one finds the optimal alignment of the sample. Usually then one performs longitudinal scans (where the ratio between Ψ and Φ remains the same) in order to check the lattice constants. After the sample alignment and the correction of the lattice constants the spectrometer is prepared for inelastic measurements. That means one can start to measure phonons. For our orthorhombic sample of YBCO

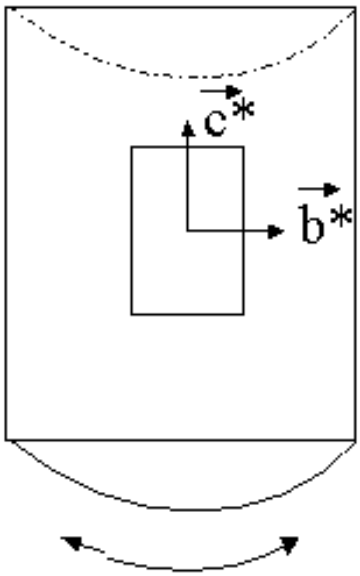

Figure 5.3: Mechanical alignment of the sample on top of the goniometer plate.

6.6 with $b = 3.885$ and with a value of the initial propagation vector $k_i = 3.5\mathring{A}^{-1}$ one gets an angle $2\theta \approx 60$ degrees. During our measurements described in the following chapter we aligned the sample in the a^*c^* and b^*c^* plane by the use of the (2, 0, 0), (0, 0, 9) and the (0, 2, 0), (0, 0, 9) Bragg reflections, respectively.

5.2 Dynamical structure factor for phonons

For the derivation of the dynamical structure factor for phonons, one follows the derivation for neutron diffraction in section 2.3. From equation 2.23:

$$S(\vec{K},\omega) = \frac{1}{2\pi\hbar}\sum_l \exp\left(i\vec{K}\vec{l}\right)\exp\langle U^2\rangle \int \exp\langle UV\rangle \exp\left(-i\omega t\right)dt \qquad (5.1)$$

it follows not only the scattering function for diffraction but also the scattering function for phonons. From $\langle U^2\rangle$ it follows the Debye-Waller factor:

$$\langle U^2\rangle = -2W = -\frac{\hbar}{2MN}\sum_s \frac{(\vec{K}\vec{\varepsilon_s})^2}{\omega_s}\coth(1/2\hbar\omega_s\beta) \qquad (5.2)$$

the Debye-Waller constant W, $\beta = \frac{1}{k_B T}$ and k_B is the Boltzmann constant.
The integral in equation 2.26 contains the factor $\exp\langle UV\rangle$ which can be expanded

by expansion of the e-function:

$$\exp\langle UV\rangle = 1 + \langle UV\rangle + \frac{1}{2!}\langle UV\rangle^2 + ... \tag{5.3}$$

The first term yields the scattering function for elastic scattering (see section 2.3). The second term refers to the annihilation or creation of one phonon. This term yields the scattering function and thus the differential cross section of one phonon scattering. Therefore the expansion above is called the phonon expansion. The third order terms yield the scattering functions of two-phonon scattering. However this term and higher order terms have less intensity and usually contribute to a diffuse background in inelastic neutron scattering experiments.
So in order to calculate the scattering function of one-phonon processes we have to calculate the following expectation value:

$$\begin{aligned}
\langle n_s|UV|n_s\rangle &= \langle n_s|(ca_s + c^* a_s^+)(da_s + d^* a_s^+)|n_s\rangle & (5.4)\\
&= cd^*\langle n_s + 1\rangle + c^* d\langle n_s\rangle & (5.5)\\
&= \left(\frac{\hbar}{2MN}\right)\frac{(\vec{K}\vec{\varepsilon_q})^2}{\omega_q} & (5.6)\\
&\quad \left[\exp -i(\vec{q}\,\vec{l} - \omega_q t)\langle n_s + 1\rangle + \exp i(\vec{q}\,\vec{l} - \omega_q t)\langle n_s\rangle\right]. & (5.7)
\end{aligned}$$

Here the brackets still represent the thermal average and hence $\langle n_s\rangle$ is the Bose occupation number for the phonon mode with wave vector $\vec{q}$ and polarization j. The Bose factor is then:

$$\langle n_s\rangle = \frac{1}{exp(\hbar\omega_q/k_B T) - 1}. \tag{5.8}$$

Now we can insert the one-phonon term of the phonon expansion in the equation 5.1 and obtain for the scattering function:

$$\begin{aligned}
S(\vec{K},\omega) &= \frac{1}{2\pi\hbar}\exp(-2W)\sum_l \exp(i\vec{K}\vec{l})\cdot & (5.9)\\
&\quad \left(\frac{\hbar}{2MN}\right)\frac{(\vec{K}\vec{\varepsilon_q})^2}{\omega_q}\int_{-\infty}^{\infty} dt\exp(-i\omega t) & (5.10)\\
&\quad \left[\exp -i(\vec{q}\,\vec{l} - \omega_q t)\langle n_s + 1\rangle + \exp i(\vec{q}\,\vec{l} - \omega_q t)\langle n_s\rangle\right]. & (5.11)
\end{aligned}$$

Using the following two expressions for the δ-function

$$\int \exp -i(\omega \pm \omega_q)t \;\; dt = 2\pi\delta(\omega \pm \omega_q) \tag{5.12}$$

and

$$\sum_l \exp i(\vec{K} \pm \vec{q})\cdot\vec{l} = \frac{(2\pi)^3}{v_0}\sum_G \delta(\vec{K} \pm \vec{q} - \vec{G}), \tag{5.13}$$

one obtains for the scattering function for one-phonon processes:

$$S(\vec{K},\omega)_{\pm 1} = \frac{(2\pi)^3}{v_0}\frac{1}{2MN}\exp -2W \sum_G \frac{(\vec{K}\varepsilon_q)^2}{\omega_q} \tag{5.14}$$

$$\left[\left(\langle n(\omega_q)\rangle + \frac{1}{2} \pm \left(-\frac{1}{2}\right)\right)\delta(\omega \pm \omega_q)\delta(\vec{K} \pm \vec{q} - \vec{G})\right] \tag{5.15}$$

where v_0 is the volume of the unit cell in reciprocal space and $\vec{G}$ is an arbitrary reciprocal lattice vector. This is the complete expression for the scattering function of the one-phonon process for a given mode. The annihilation of one phonon refers to the plus sign, whereas the creation of a phonon is referred to the minus sign.
Now we consider again all phonon modes, that means we include the sum over the given normal modes s. Moreover we assume that there are more than one atom within the nuclear unit cell and that they have different masses. Then we obtain for the coherent differential cross section for the one-phonon annihilation or creation process the following expression [3]:

$$\left(\frac{d^2\sigma}{d\Omega dE_f}\right) = \frac{(2\pi)^3}{v_0}\cdot\frac{k_f}{f_i}\sum_{s=\{\vec{q},j\}}\sum_{\vec{G}}\frac{F^2(\vec{K},\vec{q})}{2\omega_s} \tag{5.16}$$

$$\left[\left(\langle n(\omega_q)\rangle + \frac{1}{2} \pm \left(-\frac{1}{2}\right)\right)\delta(\omega \pm \omega_s)\delta(\vec{K} \pm \vec{q} - \vec{G})\right], \tag{5.17}$$

where $F(\vec{K},\vec{q})$ is the dynamic structure factor:

$$F(\vec{K},\vec{q}) = \left|\sum_d \frac{b_d}{\sqrt{M_d}}\exp(i\vec{K}\vec{r_d})[\vec{K}\vec{\varepsilon_j}(\vec{q})]\exp -W_d(\vec{q})\right|, \tag{5.18}$$

where d is the index over all basis atoms within the nuclear unit cell, hence M_d is the mass of the dth atom and b_d is the scattering length of the dth atom. By introducing more than one atom within the nuclear unit cell one had also to include the corresponding phase factor $\exp(i\vec{K}\vec{r_d})$ for each atom, as they are at different positions $\vec{r_d}$ within the unit cell.
The differential cross section for one-phonon scattering (equation 5.17) contains besides the dynamic structure factor and the Bose factor also two products of δ-functions in the four dimensional $\omega, \vec{K}$-space. These δ-functions ensure the energy and momentum conservation during the scattering process. The plus sign within equation 5.17 refers to the Stokes process, a scattering process where phonon creation appears. That means the energy transfer to the target is $\omega = +\omega_q$, whereas the neutron energy change is $E_f - E = -\hbar\omega_q$. This is also the energy conservation during the scattering process while the momentum conservation reads $\vec{K} = \vec{k}_f - \vec{k}_i = \vec{G} + \vec{q}$.
The minus sign within equation 5.17 refers to the Anti-Stokes process, a scattering

process where phonon annihilation appears. That means the energy transfer to the target is $\omega = -\omega_q$, whereas the neutron energy change is $E_f - E = +\hbar\omega_q$. Again this is the energy conservation during the scattering process while the momentum conservation reads now $\vec{K} = \vec{k}_f - \vec{k}_i = \vec{G} - \vec{q}$. For $T = 0$ only phonon creation is possible as there are no phonons excited within the target. Moreover it should be recognized that the intensity for the Stokes and Anti-stokes processes depend especially on the Bose factor (within the scattering function). The lower the temperature the more probable are phonon creation processes compared to phonon annihilation processes. The momentum is conserved relative to a reciprocal lattice vector $\vec{G}$. If the phonon wave vector differs by a multiple of the reciprocal lattice vector this doesn't affect the displacements of the atoms and hence the phonon energy doesn't change either. Therefore the dispersion relation of a phonon mode $\omega(\vec{q})$ can be measured in any Brillouin zone which is experimentally obtainable. However the dynamic structure factor differs within different Brillouin zones if there are more than one atom within the nuclear unit cell.
The dynamic structure factor also depends on the scalar product $\vec{K}\vec{\varepsilon}_q$. That means especially that the scattering geometries are different for longitudinal and transversal phonons. And hence due to that factor one can distinguish between longitudinal and transversal phonons. For a longitudinal phonon the polarization vector is parallel to the phonon wave vector, whereas for a transversal phonon the polarization vector is orthogonal to the phonon wave vector.
In a three dimensional lattice with N unit cells each containing r atoms there are three acoustic phonon branches and $3r-3$ optical phonon branches. For each phonon branch there exists a dispersion relation $\omega(\vec{q})$. (The dispersion relation contains N $\omega(\vec{q})$ points.) This relation meaning the frequency goes to zero if the phonon wave vector goes to zero for acoustic modes, whereas it remains finite for the phonon wave vector going to zero for optical modes. For acoustic branches as well as for optical branches one third of the modes is longitudinal and two thirds are transversal modes.
In addition, the cross section is damped with increasing temperature because of the temperature dependent Debye-Waller factor.
The proportionality $S(\vec{K}, \varepsilon_q) \propto 1/\omega_q$ is typical for any inelastic neutron scattering. The differential cross section in equation 5.17 considers the ideal case that the phonon lifetime is infinitely high. However in real systems the phonon-phonon interaction and the electron-phonon interaction tend to give the phonon a finite life time. One can consider this dissipation of energy and describe the phonon with the model of the damped harmonic oscillator. Therefore on has to replace in equation 5.17 the δ-functions by a Lorentzian function, which describes the phonon with its finite life time Γ_s (given as the peak half-width at half maximum, HWHM) and

simultaneously renormalizing the phonon frequencies [2] $\omega_s^2 = \omega_s'^2 + \Gamma_s^2$:

$$\frac{1}{\omega_s}\delta(\omega \pm \omega_s) \rightarrow \frac{1}{\pi\omega_s'}\frac{\Gamma_s}{[\omega \pm \omega_s']^2 + \Gamma_s^2}. \tag{5.19}$$

5.3 Phonon energy analysis and constant $\vec{K}$-scan

For the following two sections the book [3] was used as a good basis for information. In the last section it was summarized that there exist several phonon branches depending on the number of atoms within the nuclear unit cell. Measuring phonons means now to chose one of the phonon branches and measure the corresponding dispersion relation of this branch. That means one measures the energy of the phonon depending on the phonon wave vector. Phonon dispersions are usually measured in a constant $\vec{K}$-mode. That means that $\vec{K} = \vec{G} \pm \vec{q}$ is kept constant during the measurements (also called scan). However, for special reasons constant energy scans can also be useful. In figure number 5.4 is shown, that in principle the dispersion relation can be measured by a constant $\vec{K}$- or a E-energy scan. In

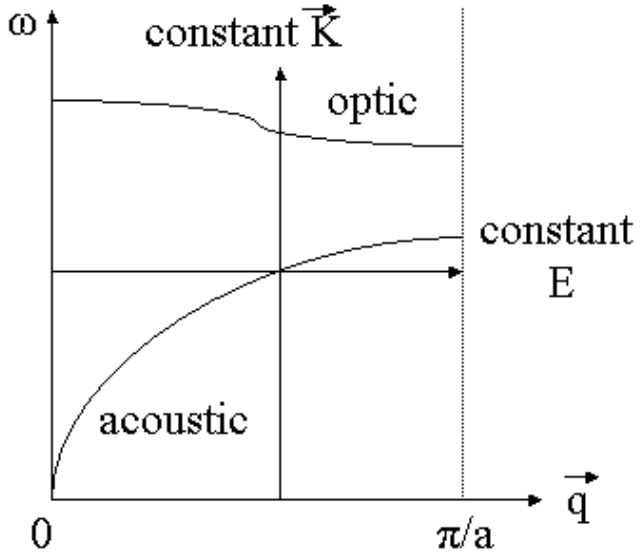

Figure 5.4: Schematic dispersion relation of one optical and one acoustical mode within the first Brillouin zone (simplified figure for one dimension). Moreover a constant $\vec{K}$-scan and a constant E-scan are shown. This is in principle the way of measuring points within the phonon dispersion relation.

principle there are two different ways of measuring the dispersion relation by a constant $\vec{K}$-scan: Either one can measure with fixed final or with fixed initial energy. Moreover one can measure with neutron energy loss or with neutron energy gain.
Figure 5.5 shows the scattering triangle for neutron energy loss and fixed final energy. Fixed final energy means that the spectrometer angle $2\theta_A$ is fixed during the scan. According to Bragg's law then the final energy of the neutrons are fixed during the scan. Moreover the spectrometer angle $2\theta_M$ is scanned during the measurement, that means the initial energy of the neutrons varies. In figure 5.5 one recognizes

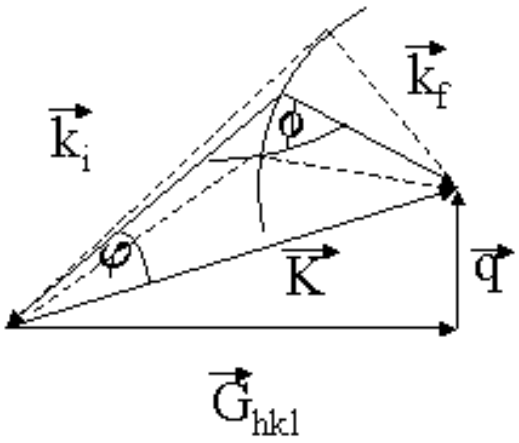

Figure 5.5: A constant $\vec{K}$-scan is shown. Moreover the final energy is fixed, meaning that $\vec{k}_f$ describes a circle when the spectrometer angle ϕ and φ change. The measurement is shown for neutron energy loss.

that

$$|k_f| < |k_i|, \tag{5.20}$$

as we measure with energy loss. Moreover this figure shows the scattering condition for inelastic scattering:

$$\vec{K} = \vec{k}_f - \vec{k}_i = \vec{G}_{hkl} + \vec{q}, \tag{5.21}$$

which is equivalent with an Stokes transition. Moreover the figure shows how the spectrometer angles Φ and φ (refers to Ψ as Ψ is in general defined as the angle between k_i and a crystallographic axis) change, whereas the scattering vector itself $\vec{K} = \vec{G}_{hkl} + \vec{q}$ remains constant, but the energy $\hbar\omega$ changes during the scan. As a short summary that means that the spectrometer angles $2\theta_M$, Ψ and $2\theta_S$ are changed during a scan with fixed final energy.
It is also possible to measure with fixed initial energy. In principle this is the same as above, but that this time $\vec{k}_i$ describes a circle during the change of Φ and φ and

not $\vec{k}_f$. And $2\theta_M$ is fix whereas $2\theta_A$ is scanned. So if one measures with fixed initial energy the spectrometer angles Ψ, $2\theta_S$ and $2\theta_A$ are scanned.

5.4 Polarization Analysis

With a triple-axis spectrometer one can measure both longitudinal and transversal phonons. As shown in section 5.2 the dynamic structure factor depends on the scalar product of the scattering vector and the polarization vector:

$$F(\vec{K}, \vec{q}) \propto |\vec{K}\vec{\varepsilon_j}(\vec{q})|^2. \tag{5.22}$$

That means that the intensity of transversal or longitudinal phonon depends on the scattering geometry and thus one can distinguish between longitudinal and transversal phonons. The scattering triangle for the measurement of a transversal phonon is shown in figure 5.6. Transversal phonon means that the polarization vector $\vec{\varepsilon}_j(\vec{q})$

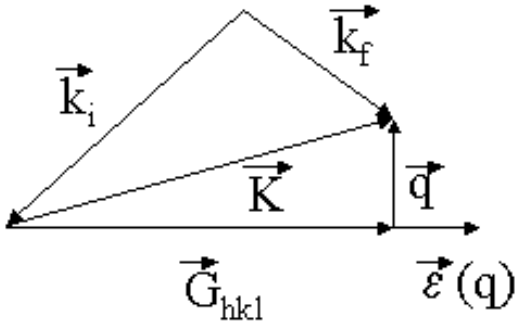

Figure 5.6: Scattering triangle for the measurement of a transversal phonon is shown. For a transversal phonon the phonon wave vector $\vec{q}$ is orthogonal to the scattering vector $\vec{K}$, as this ensures that the scattering vector is parallel to the polarization vector $\vec{\varepsilon}_j(\vec{q})$. Hence the intensity is maximal due to the dynamic structure factor.

is orthogonal to the phonon wave vector $\vec{q}$. Because of the dynamic structure factor the polarization vector and the scattering vector $\vec{K}$ should be parallel in order to have maximum intensity for the transversal phonon. As it is shown in the figure, that means that the phonon wave vector $\vec{q}$ is almost perpendicular to the scattering vector.
Whereas for longitudinal phonons the situation is different. This time the polarization vector is parallel to the phonon wave vector and hence the phonon wave vector is parallel to the scattering vector, as the polarization vector needs to be parallel

to the scattering vector in order that the intensity is maximal for the longitudinal phonon.

5.5 Resolution function of a triple-axis spectrometer

With a triple-axis spectrometer one can in general measure a point in four dimensional reciprocal space $(\vec{K}, \omega)$. If one measures for example the dispersion relation $\omega(\vec{q})$ of a phonon mode one makes a constant $\vec{K}$- or a constant E-scan trough the points of the dispersion relation within the four dimensional reciprocal space: $(\vec{K} = \vec{G} + \vec{q},\ \omega(\vec{q}))$. The constant $\vec{K}$-scan was explained in section 5.3.
As a basis for the following two sections the book Shirane, Shapiro and Tranquada [2] was used in order to obtain important information about the resolution function of a triple-axis spectrometer and spurious peaks.
However small scattering cross sections of the neutrons and limited neutron flux available makes it necessary that one has finite beam divergences and that the monochromator and analyzer crystals have significant mosaic widths. That means the neutron beam has an energy and momentum distribution around the mean values $(\omega_0, \vec{K}_0)$. The measured signal in a neutron scattering experiment depends not only on the scattering function $S(\vec{K}, \omega)$ alone, but on the convolution of the spectrometer resolution function $R(\vec{K} - \vec{K}_0, \omega - \omega_0)$ and the scattering function. Therefore the measured signal depends on the way how the resolution function is scanned through the structures defined by the scattering function [2]. One might improve the measured spectra by knowledge of the resolution function. The first analysis of the resolution function was made by Cooper and Nathans in 1967 [40] and the proper normalization of the resolution function was showed by Chasser and Axe in 1973 [41].
The angular divergence is typically limited by the collimators C_j, which are situated between the source and the monochromator, the momochromator and the sample, the sample and the analyzer and between the analyzer and the detector. However, one can also make inelastic neutron measurements without collimators letting the divergence of the beam being determined by the monochromator and the analyzer crystal. The collimators are assumed to have a gaussian transmission function with width α_j in the horizontal scattering plane and width β_j in the vertical direction. Moreover the monochromator and the analyzer are assumed to have a gaussian mosaic distribution of width η_M and η_A, respectively, in the horizontal plane and $\eta_M^{'}$ and $\eta_A^{'}$, respectively, in the vertical direction. Therefore it follows a gaussian distribution of the energy and the momentum of the neutrons within the beam.
The neutrons incident on the sample are characterized by an average wave vector $\overline{\vec{k}_i}$.

Its length is determined by the monochromator and the direction by the collimator between the monochromator and the sample. The initial momentum distribution of $\vec{k}_i$ given by $P_i(\vec{k}_i - \overline{\vec{k}_i})$ is determined by the transmission functions for the collimators before and after the monochromator and by the monochromator itself. The final momentum distribution of $\vec{k}_f$ given by $P_f(\vec{k}_f - \overline{\vec{k}_f})$ is determined by the collimators before and after the analyzer and the analyzer itself. Therefore the spectrometer defines the distribution of the incident wave vectors $\vec{k}_i$ reaching the sample and the scattered wave vectors $\vec{k}_f$ reaching the detector. Whereas the scattering properties of the sample depend only on the energy transfer $\hbar\omega$ and the momentum transfer $\hbar\vec{K}$. The relationship between these values is given by the law of energy and momentum conservation:

$$\hbar\omega = \frac{\hbar^2}{2m_n}(\vec{k}_i^2 - \vec{k}_f^2),\ \vec{K} = \vec{k}_i - \vec{k}_f. \tag{5.23}$$

Therefore also the average energy and momentum transfer depends on $\overline{\vec{k}_i}$ and $\overline{\vec{k}_f}$. In order to calculate the flux reaching the detector, we consider first of all a simplified differential cross section, where some of the prefactors of the scattering function such as the nuclear cross section σ_{coh} are included within the scattering function [2]:

$$\frac{d^2\sigma}{dE_f d\Omega_f} = \frac{k_f}{k_i} S(\vec{K}, \omega), \tag{5.24}$$

where $d\Omega_f$ is the final differential element of solid angle and the final energy is given by the dispersion relation for neutrons $E_f = \hbar^2 k_f^2 / 2m_n$. By rewriting the differentials for the solid angle and the energy and using a cartesian coordinate system with the z-axis along $\vec{k}_f$ one can rewrite the differential cross section in the following form:

$$\frac{d^3\sigma}{dk_f^3} = \frac{\hbar^2}{m_n} \cdot \frac{1}{k_i} \cdot S(\vec{K}, \omega). \tag{5.25}$$

Together with the momentum distributions of the neutron beam before and after the scattering process P_i and P_f one can write the flux reaching the detector in the following form:

$$F_d(\overline{\vec{k}_i}, \overline{\vec{k}_f}) = \int d\vec{k}_i d\vec{k}_f F_i(k_i) P_i(\vec{k}_i - \overline{\vec{k}_i}) \frac{d^3\sigma}{dk_f^3} P_f(\vec{k}_f - \overline{\vec{k}_f}), \tag{5.26}$$

where the initial flux is given by the equation $F_i(k_i) = k_i \phi(k_i)$, which can be approximated by $k_i \phi(\overline{k_i})$. One can now introduce the resolution function by defining:

$$F_d(\omega_0, \vec{K}_0) = \phi(\overline{k_i}) \int d\omega d\vec{K} R(\omega - \omega_0, \vec{K} - \vec{K}_0)\ S(\vec{K}, \omega), \tag{5.27}$$

where ω_0 and $\vec{K}_0$ correspond to $\overline{\vec{k}_i}$ and $\overline{\vec{k}_f}$. This definition shows that one doesn't measure the scattering function at the detector but a four dimensional convolution of the scattering function and the spectrometer resolution function. From the equations 5.24 - 5.27 one can derive an expression for the resolution function in which it depends on an integral over the initial and final wave vectors containing the momentum distributions of the initial and final neutron beam and δ-functions ensuring the law of energy and momentum conservation. These δ-functions give the relation between the scattering variables of the sample (the energy and momentum transfer) and the variables defined by the spectrometer (the initial and final wave vectors). In order to give a functional form for the resolution function one introduces the four dimensional vector of the deviations $\Delta\kappa$:

$$\Delta\kappa = (\frac{m_n}{\hbar K_0}(\omega - \omega_0), K_\parallel - K_0, K_\perp, K_z) \tag{5.28}$$

and a 4×4 matrix M called the resolution matrix. Moreover one has to use the gaussian approximation, that means to consider the collimator transmission functions and the mosaic distributions of the monochromator and analyzer crystals being gaussian distributions. Then if follows for the resolution function a four dimensional gaussian distribution [40]:

$$R(\omega - \omega_0, \vec{K} - \vec{K}_0) = R_0 \exp(-\frac{1}{2}\Delta\kappa M \Delta\kappa), \tag{5.29}$$

with R_0 and M being functions of the value of the initial, final wave vector $\overline{k_i}, \overline{k_f}$ and the scattering angle $2\theta_S$. Setting the argument of the exponential in equation 5.29 constant defines a four dimensional ellipsoid. In general the matrix M is not diagonal, however, if one uses the paraxial approximation (small beam divergence) then the matrix M separates in a 3×3 matrix coupling $\omega, \Delta K_\parallel$ and $\Delta K_\perp$ and a 1×1 Matrix for ΔK_z. Equation 5.29 means that the shape of the resolution function is given by the deviations $\Delta\kappa$ from the average values of the point $(\vec{K}_0, \omega_0)$. Within the scattering plane these deviations can be decomposed, where $\Delta\kappa_\parallel$ is parallel to $\vec{K}$ and $\Delta K_\perp$ is perpendicular to $\vec{K}$. In figure 5.7 these relationships are shown within the scattering plane for a right handed system. That means that the monochromator and the analyzer crystal scatters to the right. The deviation ΔK_z is perpendicular to the scattering plane. The resolution function is maximal at $(\vec{K}_0, \omega_0)$ and decreases for deviations $\Delta\kappa$ and constant amplitude plots are ellipsoids in $(\vec{K}, \omega)$-space around this maximal value. The volume and the shape of these ellipsoids depend only on $(\vec{K}_0, \omega_0)$. Because of the extension of the resolution ellipsoid the effective resolution depends not only on the spectrometer but also on the structure present in the scattering function. Finally one can characterize the resolution of a triple-axis spectrometer by the deviations $\Delta\kappa$ for a given amplitude

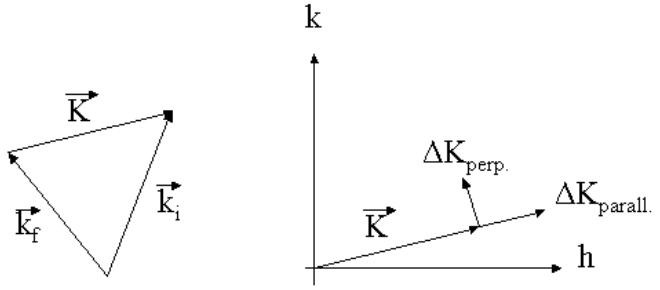

Figure 5.7: Shows the scattering vector $\vec{K}$ in reciprocal space with the scattering triangle at the left and with the deviations $\Delta K_{\parallel} = \Delta K_{parall.}$ and $\Delta K_{\perp} = \Delta K_{perp.}$ at the right. These deviations can be used to characterize the resolution of the spectrometer. Moreover they are the semi axis of the resolution ellipsoid describing constant amplitudes of the resolution function.

for example the deviations for half the maximum.
The vertical direction of the deviations $\Delta\kappa$ is decoupled from these within the scattering plane. Therefore it is enough to consider a three dimensional resolution ellipsoid: the in-plane momentum components (scattering plane of the spectrometer) and the energy. In general the shape of the resolution ellipsoid is a flattened cigar. The peak width of a measured point depends on the relative orientation of the resolution ellipsoid to the dispersion function. This can be understood with the help of figure 5.8. The dispersion relation is given by the area $\omega(\vec{K})$ within $(\vec{K}, \omega)$-space. It shall steeply increase in the direction of the $\vec{K}$-scan. The resolution is given by the deviation components $\Delta\kappa$ within the scattering plane $\{h, k\}$ and $\Delta\omega$ as the three dimensional resolution ellipsoid and whose two dimensional projection on the scattering plane is shown. During a constant $\vec{K}$-scan the resolution ellipsoid moves through the $(\vec{K}, \omega)$ space. Wherever it crosses the dispersion relation $\omega(\vec{K})$ a signal $I(\vec{K_0}, \omega)$ is being measured according to equation 5.27. This equation can be simplified by assuming a sharp dispersion relation so that the scattering function can be modelled as a δ-function:

$$S(\vec{K}, \omega) = S_0 \delta \left[\omega - \omega(\vec{K}) \right], \tag{5.30}$$

where S_0 is a constant. Then for the intensity measured at point $(\vec{K_0}, \omega)$ is

$$I(\vec{K_0}, \omega) = V_i^{-1} S_0 \int d\vec{K} R \left[\omega(\vec{K}) - \omega, \vec{K} - \vec{K_0} \right], \tag{5.31}$$

where V_i is a constant so that the intensity is normalized to the monitor count rate. That means that the measured intensity depends crucially on the spectrometer

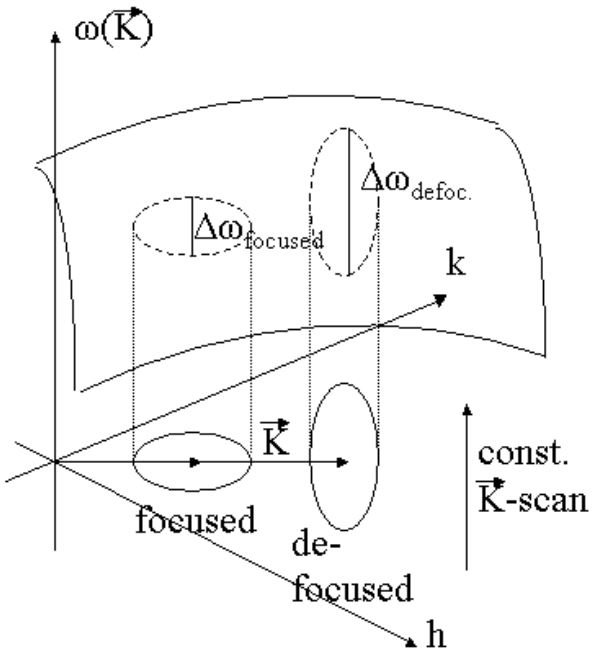

Figure 5.8: Constant $\vec{K}$-scan is shown in a focused and a defocused condition. In the focused condition the long axis of the resolution ellipsoid is parallel to the dispersion relation and hence the measured peak width $\Delta\omega_{focused}$ is minimal, whereas for the defocused condition the long axis of the resolution ellipsoid is perpendicular to the dispersion relation and hence the peak width $\Delta\omega_{defoc.}$ is maximal.

resolution function. If the long axis of the resolution ellipsoid is parallel to the dispersion relation (left part of the picture 5.8) one speaks of a "focused" condition and the measured peak width is minimal. Whereas if the long axis is perpendicular to the dispersion relation the measured peak width might be quite long and we speak of a "defocused" condition (right part of the picture 5.8). However, if the dispersion relation is quite flat the orientation of the resolution ellipsoid relative to the dispersion relation is not so important.
By changing the point $(\vec{K}, \omega)$ in reciprocal space the resolution ellipsoid changes the directions of its semi axis. This effect can be used by making the measurements at points in reciprocal space where the resolution ellipsoid has the orientation of the focused case. Moreover the choice of the spectrometer parameters will affect the peak widths and intensities. However, there appears often the interchange between intensity and resolution. That means a compromise between both must be found. For example if one increases the order of the monochromator reflection one can

increase the resolution but one reduces at the same time the measured intensity.

5.6 Spurious peaks

If one makes neutron scattering experiments one must beware of so-called spurious peaks or spurions which are no intrinsic feature of the scattering function but which are nevertheless well defined, sharp peaks. These features can lead to confusion even if they are quite weak, if one wants to measure for example phonons with inelastic neutron scattering. As then even weak features can be of comparable intensities to the peaks which are intended to be measured. Therefore in this section different spurions and the explanation of their appearance will be discussed.

5.6.1 Higher-order neutrons

Higher-order neutrons can lead to spurious effects even if the intensity of higher-order neutrons is generally hundreds of times weaker than the first order neutron beam. A perfect monochromator would diffract one beam with well defined initial wave vector. However the diffraction process is given by Bragg's law which gives the initial wave vector k_i depending on the lattice constant d_{hkl} and the scattering angle θ:

$$k = \frac{n\pi}{d_{hkl}\sin\theta}, \tag{5.32}$$

where n is an arbitrary number which gives the explanation for higher-order reflections. These higher-order neutrons are scattered under the same angle than the first order neutrons and are hence within the neutron beam being incident on the sample (if they are not excluded by appropriate filters or velocity selectors). However these neutrons have different energies and wave vectors and can therefore lead to unexpected features.
For inelastic scattering one has to consider higher-order harmonics at the monochromator and the analyzer [2]. In the following a formula will be presented to calculate the energy transfer of potential spurions due to higher-order neutrons from the monochromator and/or analyzer. The higher-order neutrons from the monochromator have the initial energies:

$$E_i(n_M) = n_M^2 E_i, \tag{5.33}$$

where n_M gives the order of the scattered neutrons and the neutrons scattered by the analyzer due to higher harmonics have the final energies:

$$E_f(n_A) = n_A^2 E_f, \tag{5.34}$$

where n_A gives the order of the scattered neutrons at the analyzer.
Especially strong will the spurious peaks due to higher-order neutrons be if the neutrons are scattered elastically on the sample. Then it follows for identical monochromator and analyzer crystals set for the same reflection the energy transfer at which the potential spurion is being observed:

$$\hbar\omega = \left(1 - \frac{n_M^2}{n_A^2}\right) E_i = \left(\frac{n_A^2}{n_M^2} - 1\right) E_f. \tag{5.35}$$

An example for a higher-order peak according to the above formula is if the initial energy is fixed and set to $40meV$ and one wants to measure inelastically at an energy transfer of $30meV$. Then the spurious peak due to second-order harmonic scattering of the analyzer (first order of the monochromator) will also appear at the energy transfer of $30meV$. As the monochromator scatters at first order it is not possible to attenuate this kind of higher order reflections with an appropriate filter. A filter is only useful if both scattering processes at the monochromator and the analyzer crystal are of second or higher order. Especially one can filter higher order neutrons from the monochromator by a PG filter or by a velocity selector. A velocity selector is better, as it can filter out second-order neutrons for different initial wave vectors $\vec{k}_i$. That means the selector follows the initial wave vector if it is changed. With a PG filter one is restricted to a certain range of initial wave vectors.

5.6.2 Accidental Bragg Scattering

A certain spectrometer configuration is not unique in that sense that it corresponds to one well defined scattering event, but that also other scattering events might occur. If the spectrometer angles of the triple-axis spectrometer are set in order to measure an excitation with a given energy transfer and wave vector $\vec{q}$, it is possible that the scattering triangle is also appropriate for a certain Bragg peak $\vec{G}$ of the sample to be scattered, meaning that especially the scattering angle $2\theta_S$ is equal. One has to consider, that the scattering condition for the elastic Bragg peak only has to be fulfilled within the boarders of the resolution function, as the Bragg peaks are very intensive and can lead to spurious peaks in inelastic scattering data even if the intensity is only half the maximal value. Afterwards these neutrons might be scattered incoherently at the analyzer and hence being measured at the detector in addition to the neutrons which had been scattered with the correct energy. This process for accidental Bragg scattering is shown in figure 5.9 for energy loss. A similar situation appears for energy gain, where also the scattering angle is equal for both the inelastic and the accidental elastic scattering process.
Instead of the incoherent scattering at the analyzer crystal, it is also possible that the incoherent scattering occurs at the monochromator. This is also shown in fig

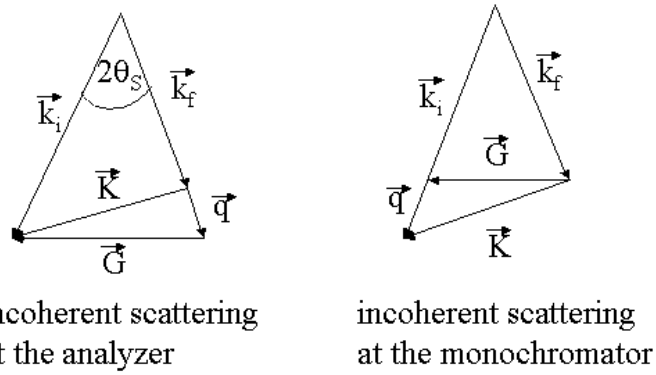

Figure 5.9: Scattering triangles for energy loss spectroscopy where accidental Bragg scattering is shown. At the left accidentally scattered neutrons at the sample are scattered incoherently at the analyzer and hence can contribute to the measured signal at the detector as a spurious peak. At the right incoherently scattered neutrons at the monochromator are accidentally scattered by the sample and can hence contribute to the measured signal. For both cases it was intended to measure only inelastic neutron scattering from the sample.

5.9 at the right side also for energy loss. In this case the monochromator scatters neutrons incoherently in the same direction with the neutrons being scatterers with initial wave vector $\vec{k_i}$ but with the absolute value of the final wave vector $\vec{k_f}$. Then these neutrons are again scattered by accidental Bragg scattering at the sample and arrive at the detector with the neutrons being scattered inelastically.
In order to investigate spurious scattering due to accidental Bragg Scattering further it is helpful to determine the points in $(\vec{K}, \omega)$ space at which they might occur. Therefore we will derive the so-called dispersion relation for these spurions and we will consider the case where the neutrons are scattered incoherently at the analyzer crystal. One condition for accidental Bragg Scattering is, that the scattering angle for the inelastic case is equal to the scattering angle for elastic scattering, which is given by Bragg's law:

$$\sin\theta_S = \frac{G}{2k_i}. \tag{5.36}$$

The relationship between the initial and final wave vectors $\vec{k_i}$, $\vec{k_f}$ and the reciprocal lattice vector $\vec{G}$ is

$$\vec{G} = \vec{k_i} - \left(\frac{k_i}{k_f}\right)\vec{k_f}. \tag{5.37}$$

Moreover one uses the definitions of the scattering vector $\vec{K} = \vec{k}_i - \vec{k}_f$ and the phonon wave vector $\vec{q} = \vec{K} - \vec{G}$ in order to derive the following two relations:

$$q = k_i - k_f \tag{5.38}$$

$$\cos\alpha = sin\theta_B = \frac{G}{2k_i}, \tag{5.39}$$

where α is the angle between the phonon wave vector $\vec{q}$ and the reciprocal lattice vector $-\vec{G}$. For fixed final energy the formal energy transfer for the spurious peaks due to accidental Bragg scattering and incoherent scattering at the analyzer is:

$$\hbar\omega = \frac{\hbar^2}{m_n} k_f q (1 + \frac{q}{2k_f}). \tag{5.40}$$

For $q \ll k_f$ this dispersion relation is linear for fixed final energy:

$$\hbar\omega = \frac{\hbar^2}{m_n} k_f q. \tag{5.41}$$

For inelastic scattering these spurious peaks are especially dangerous because of the much higher intensity of a Bragg peak compared with the intensity for inelastic neutron scattering. Therefore and because of finite resolution effects spurious peaks can be observed even if the condition for accidental Bragg scattering is not exactly fulfilled but some degrees off. Ishikawa, Fincher and Shirane found 1980 [42] that the risk for accidental Bragg scattering can be reduced by tightening the collimation before and after the sample.

5.6.3 Spurious peaks due to the sample holder

Always part of the sample holder is within the beam. Even if it is possible to shield most of the part by cadmium. Moreover the cryostats for low temperature measurements are also within the beam. The sample holder and the cryostats are often made of Aluminium. The reason for this is first of all that aluminium is easy machinable and it is deactivated very fast after being activated when having been in the neutron beam for a longer time. This distinguishes Aluminium from other metals with higher atomic numbers. These metals are often activated for a longer time after having been in the neutron beam.
Aluminium is crystalline and therefore neutrons will be scattered elastically what leads to further Bragg peaks in the measured data. However, these Aluminium peaks are quite weak in intensity. But again if the measured signal is, especially in inelastic neutron measurements, also quite weak Aluminium peaks have to be considered. At

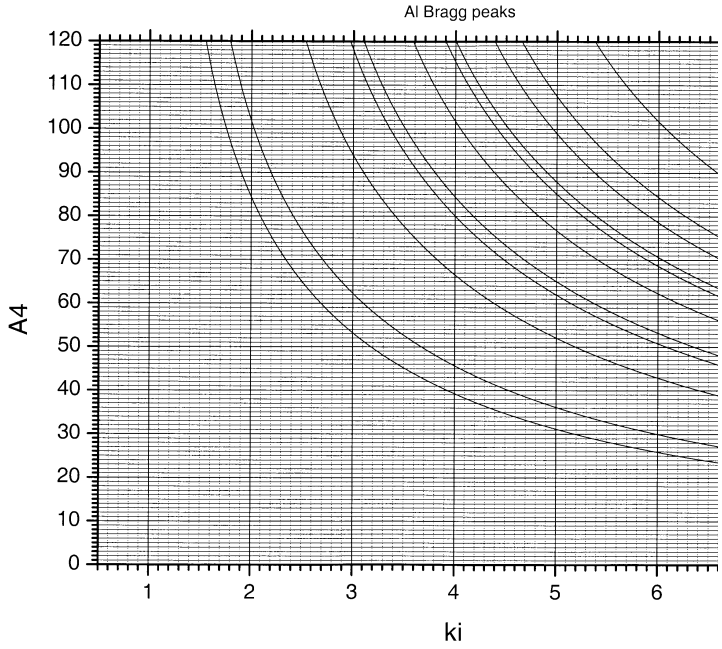

Figure 5.10: Diagram in order to determine aluminium peaks depending from the initial wave vector k_i

least one must know under which angles these peaks can occur. Figure 5.10 shows for given scattering angle 2θ (corresponds to the spectrometer angle A4) and the value of initial wave vector k_i where Aluminium Bragg reflections might occur. If one recognizes a potential spurious peak due to Aluminium one just has to look up that graph for the spectrometer angle A4 and the value of the initial wave vector k_i under which the spurion appeared and knows whether it is a Aluminium spurion or not.

It is also possible that air produces spurious effects due to a condensation process of the different parts of gases within air. One can avoid these effects by using an exchange gas like helium. As for helium gas the condensation effect is also observable but due to the weak scattering cross section of helium this effect might be not important for normal neutron measurements.

Chapter 6

Phonon measurements on $YBa_2Cu_3O_{6+x}$

This chapter contains important research results: high-resolution inelastic neutron scattering measurements on the phonon buckling mode on the system $YBa_2Cu_3O_{6+x}$ ($x = 0.6$ and $x = 1.0$) with fully detwinned samples. Due to these special experimental conditions a qualitatively and quantitatively new superconductivity-induced phonon effect could be observed.
First of all in the sections 6.1 till 6.3 general aspects of $YBa_2Cu_3O_{6+x}$ are reported. In sections 6.4 till 6.8 special topics which are related to our measurements are presented.
Our new experimental data are presented in the sections 6.9, 6.10 and 6.11. For the kind reader with few time especially the subsections 6.9.1 (p.95-p98), 6.9.2, 6.9.5, 6.11.2 and 6.11.3 are recommended. These provide a good overview of most of our data. Moreover, section 6.12 is recommended as it provides a summary and relates our data with previous literature.

6.1 The system $YBa_2Cu_3O_{6+x}$

An interesting review of the history of structure determination of the system $YBa_2Cu_3O_{6+x}$ is given in [43]. This article has been used as a main source of information for the following section: Shortly after the discovery of the first high temperature superconductor $(La, Ba)_2CuO_4$ in 1986 by J. G. Bednorz and K. A. Müeller [44] the system $YBa_2Cu_3O_{6+x}$ was discovered by Wu et al. [45]. Since then $YBa_2Cu_3O_{6+x}$ is probably the most studied high temperature superconductor with a maximal transition temperature of about $93K$ at optimal doping. The reason for this success is the property that it is easy to produce compared with

other high temperature superconducting materials and that it performs very good intrinsic superconducting behavior in an applied magnetic field [43]. These ceramic high temperature superconductors are type II superconductors. Whereas the lower critical field B_{c1} is below $10mT$ the upper critical field reaches for $YBa_2Cu_3O_{6+x}$ $340T$ [46] which is above the value for other high temperature superconductors. Moreover the superconducting transition temperature of the $YBa_2Cu_3O_{6+x}$-system (for optimal doping) lies above the gas liquid transition temperature of Nitrogen ($70K$). This makes it possible to use this substance for technical applications without the need to cool with liquid helium. The $YBa_2Cu_3O_{6+x}$-system can be doped from $x = 0$ up to $x = 1$ in a continuous way (oxygen non-stoichiometry). The maximal doping level ($x = 1$, full stoichiometry) is reached close to optimal doping. This non-stoichiometry occurs in the oxygen chains situated between two CuO_2 double layers, in which superconductivity takes place. The fact that the superconductivity takes place in two-dimensional CuO_2 double layers is also been reflected by the fact, that the coherence length along the c-axis is $\xi_c \sim 3 - 5\mathring{A}$ whereas it is within the double layer $\xi_{ab} \sim 20 - 30\mathring{A}$ in $YBa_2Cu_3O_{6+x}$.

6.1.1 The structure of $YBa_2Cu_3O_{6+x}$ and its self-doping mechanism

The contribution of neutron scattering techniques in the structure enlightment of $YBa_2Cu_3O_{6+x}$ has been considerable and therefore we will concentrate on these techniques in the following when describing the history of the Yttrium Barium Cuprate structure determination: Wu et al. [45] synthesized the first $YBa_2Cu_3O_{6+x}$ samples which were still composed of different phases. The compound was already superconducting but the stoichiometry couldn't be determined exactly. Cava et al. [47] were able to produce single phase samples of $YBa_2Cu_3O_{6+x}$ ($x \sim 0.9$) for the first time. Shortly afterwards small single crystals were available. With these single crystals it was possible ro determine the crystal structure of Yttrium Barium Cuprate by x-ray diffraction measurements [48]-[50] besides the CuO_2 chains in the basal plain which couldn't be identified correctly. Moreover it was difficult to assign the correct space group. The major problem was, that these crystals were heavily twinned.
The first correct structure analysis was obtained by neutron powder diffraction ($x \sim 1$), which is insensitive to macroscopic twinning [43]. The authors of the following papers could identify the right space group and the existence of the CuO_2 chains correctly no matter whether the measurements have been performed at a high flux reactor [51], [52], medium flux reactor [53]-[55] or a spallation source [56], [57]. The right structure of tetragonal $YBa_2Cu_3O_{6+x}$ ($x \sim 0.1$) was also resolved by neutron powder diffraction. This was done independently by Santoro et al. [58],

Hewat et al. [59] and Jorgensen et al. [60].
In order to discuss the structure of the $YBa_2Cu_3O_{6+x}$-system first of all the fully stoichiometric compound $YBa_2Cu_3O_{7.0}$ will be presented. Afterwards it is straight forward to explain the changes in the structure when the oxygen content is lowert from $x = 1$ to $x = 0$. Figure 6.1 was made with Diamond using the crystallographic data from Wu and Gao [61]. It shows the unit cell of $YBa_2Cu_3O_{7.0}$ which consists

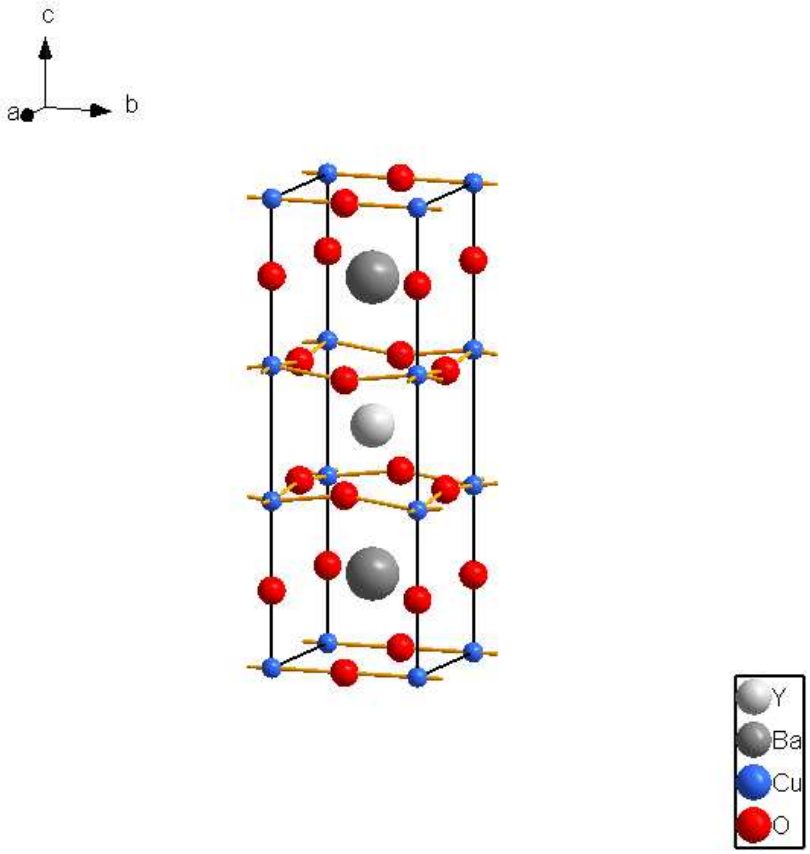

Figure 6.1: Unit cell of $YBa_2Cu_3O_{7.0}$. The light-grey ion is the Yttrium the dark-grey ions are the Barium ions. The blue ions are the copper ions and the red ions are the oxygen ions. The CuO_2 double layer with its puckered structure is shown by orange bonds between the oxygen and copper ions within these layers. The Yttrium ion is in between these two layers. This double layer is encircled by two BaO layers which contain the Barium ions and the apical oxygen. In between two of these BaO layers there is the basal plane, which is the last important building block within the unit cell. This basal plane contains (for the orthorhombic structure valid for the fully stoichiometric compound) the so-called oxygen chains, which are shown with orange CuO bonds. These oxygen chains are responsible for the intrinsic self-doping of the CuO_2 double layer with holes. For more information see text.

of three two dimensional building blocks piled up along the c direction. One of these building blocks is the CuO_2 double layer with the Yttrium in between the two neighboring layers. Yttrium is surrounded by eight oxygen ions. Within these double layers the oxygen and the copper ions are not laying in the same plane. That means these double layers are puckered. Moreover the copper ions within these double layers are surrounded by five oxygen ions four of which are also belonging to the double layer whereas the fifth is the so called apical oxygen. This oxygen belongs to the BaO layer which is the neighboring building block of the double layer in the unit cell. In figure 6.1 the CuO_2 double layer is shown in the middle of the unit cell and the bonds between the oxygen and copper ions have been drawn in orange in order to show their puckered arrangement. The second building block are the BaO planes which are surrounding the CuO_2 double layer. The Barium ion is encircled by eight oxygen ions for $x = 0$ and by ten oxygen ions for $x = 1$. That means the coordination with oxygen of Barium changes with doping. The third building block is the so called "basal plane" which is surrounded by two BaO planes. This plane only contains oxygen and copper ions. This basal plane comprises the oxygen chains which are shown in orange in figure 6.1. These chains run along the b direction. Here the non stoichiometry occurs. When lowering the doping from $x = 1$ to $x \sim 0.4$ the oxygen in these chains become less and less. Around $x = 0.4$ the orthorhombic structure (space group Pmmm) changes to tetragonal (space group P 4/mmm). (Where Pmmm is a subgroup of P 4/mmm, meaning that a second order phase transition is possible.) That means that the oxygens are no longer arranged in chains but that they are randomly placed between the copper ions along the a and the b direction. This change in symmetry is the reason for the orthorhombic to tetragonal phase transition. For $x = 0$ the copper ions in the basal plane are in the formal valence state Cu^{+1}, whereas the valence state of the copper ions within the double layer is Cu^{+2}. These valence states could be found by Hewat et al. [59] using the so-called bond valence sum method [62]. For increasing x the copper within the basal plane changes its valence state from Cu^{+1} up to $Cu^{+2.7}$, however the valence state of the copper ions within the double layer is also increased from Cu^{+2} up to $Cu^{+2.15}$. The valence states of the copper ions in the fully oxygenated compound were found by David et al. [57], who were also using the bond valence sum method [62]. The oxidation process from $YBa_2Cu_3O_{6.0}$ up to $YBa_2Cu_3O_{7.0}$ can be summarized as follows: With increasing doping more and more oxygen ions are incorporated in the basal plane (for the tetragonal structure in an arbitrary way for the orthorhombic structure in so-called oxygen chains along the b direction). This increases the valence state of the copper ions from +1 to +3. However this oxidation is incomplete as part of the charge is transferred to the CuO_2 double layer, where the copper ions change their valence state from +2 up to +2.15 (self-doping). Therefore the oxygen chains act as charge reservoir for the double layer, where the hole concentration is increased. This increase in hole concentration seems to be crucial

for the onset of superconductivity, which is known to take place within the CuO_2 double layers in $YBa_2Cu_3O_{6+x}$.

6.1.2 Further interesting properties of the system $YBa_2Cu_3O_{6+x}$: Oxygen chains and c axis anomaly

Gallagher et al. [63] has shown that it is not possible to produce $YBa_2Cu_3O_{6+x}$ samples for x below zero and above one. Moreover it was established that $YBa_2Cu_3O_{6+x}$ can be produced from $0.1 \leq x \leq 0.95$. In order to get different doping levels one can use different oxygen pressures during the annealing process. Performing system-

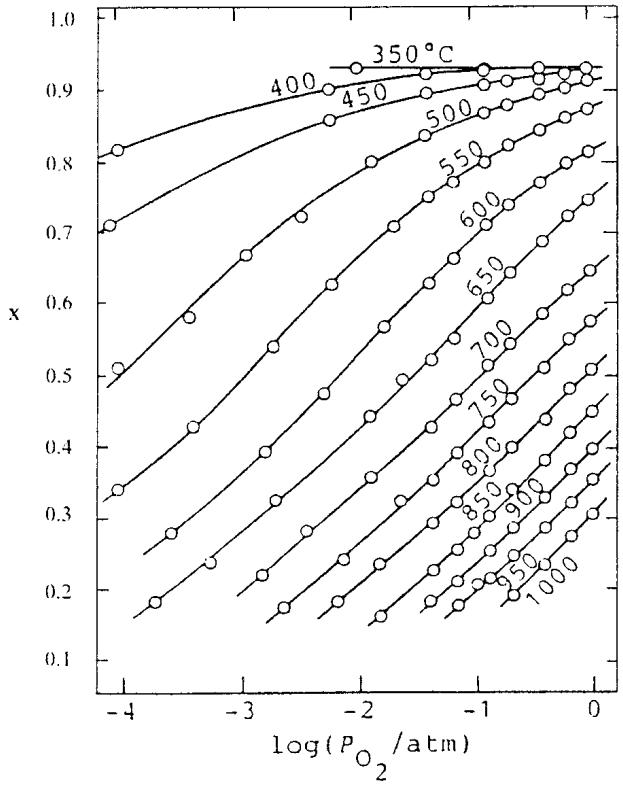

Figure 6.2: Annealing temperatures for $YBa_2Cu_3O_{6+x}$ depending on the oxygen content x and the partial oxygen pressure of the environment during the annealing process. After the annealing process the samples will be quenched in order to prevent further oxygen pick up. The diagram shows that one obtains samples with low oxygen doping x for high temperatures and low oxygen pressures. Whereas (high) oxygen pressures and lower annealing temperatures are necessary in order to get samples with high oxygen doping.

atic studies of the annealing process for different temperatures and oxygen partial

pressures P_{O_2} (see figure 6.2) allowed Kishio et al.[64] to produce Yttrium Barium Cuprate samples with different oxygen content (doping) x. The samples were annealed in an oven with the sample under a constant flow of gasses with a certain concentration of oxygen. With these samples they could observe the tetragonal-orthorhombic phase transition between the symmetric tetragonal phase for low oxygen content and the oxygen rich samples which have orthorhombic unit cells. They could determine this transition to be between $x \approx 0.4$ and 0.5. However these early samples had relatively broad superconducting transition regimes.
Another very important property of $YBa_2Cu_3O_{6+x}$ are the oxygen-ordered superstructures for the orthorhombic phase. That means that the oxygen chains running along the b direction show a characteristic superstructure along the a direction depending on the different oxygen doping level of the sample. The first evidence of these oxygen superstructures were first revealed by transmission electron microscopy and electron diffraction (TEM-ED). Van Tendeloo [65] first observed a doubling of the unit cell along the a direction. These observations were confirmed by Chaillout et al. [66], who used samples with controlled oxygen content. They could assign an arrangements of full and empty oxygen chains according to the scheme full-empty-full-empty for the doping level $x = 0.5$. Later also samples with other oxygen contents with more complicated superstructures were studied by the same group [67]. Apart from the previously mentioned procedure to produce Yttrium Barium Cuprate for different oxygen content Cava et al. [68] and Beyers et al. [69] proposed different methods for doing so. The former one yielded the first samples with especially sharp superconducting phase transitions. The latter could also produce high quality samples and investigated the oxygen superstructure further [69]. He described a tripling of the unit cell at around $x = 0.7$ with an ordering pattern full-full-empty of the oxygen chains. Later on Cava's technique were advanced [70] - [74] with similar success. The initially mentioned method of annealing Yttrium Barium Cuprate in different oxygen pressures was also advanced [75], and it was found that all these samples perform sharp transition temperatures and all superconducting samples were orthorhombic.
Before returning to the oxygen ordering in $YBa_2Cu_3O_{6+x}$ and reporting theoretical models to describe this ordering we'll shortly report some interesting features, especially the c-axis anomaly, concerning structural parameters and its dependence on different samples: For all samples (even for different production processes) it can be observed that the c axis decreases with increasing doping level x (see figure 6.3). However Cava et al. [72] found for his samples (which had been made by an alternative technique compared to the samples from Jorgensen) a sudden step like decrease of the c axis constant at the structural phase transition between the tetragonal and the orthorhombic phase. More detailed measurements could reveal that this sudden change of the c axis is related to the shortening of the distance between the copper ions in the double layer and the apical oxygen [72]. In contrast to Cava's observa-

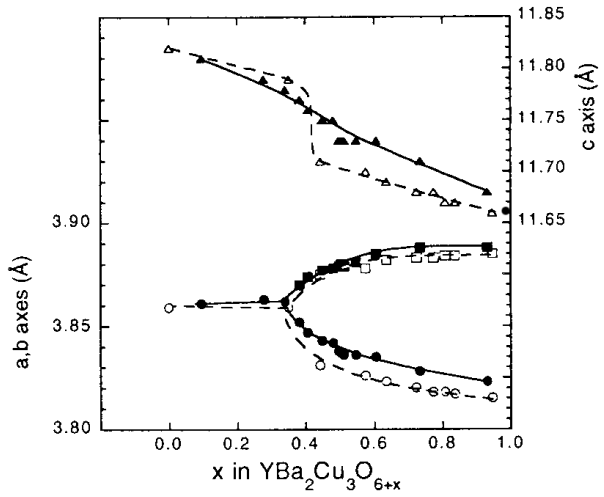

Figure 6.3: Lattice parameters of the system $YBa_2Cu_3O_{6+x}$ for different doping levels x. The change in symmetry due to the tetragonal to orthorhombic phase transition can be well recognized around $x = 0.4$ in the diagram below, meaning that the b axis is larger then the a axis for the orthorhombic phase. This is due to the formation of oxygen chains along the b axis. In the diagram above the sudden (Cava et al.) [72] and the smooth (Jorgensen et al.) [75] decrease of the c axis with increasing doping level is shown. This decrease is related to the increase of the hole concentration in the (superconducting) double layer.

tions Jorgensen et al. [75] observed a smooth decrease of the c axis constant also around the region of the structural phase transition (in detail this decrease of the c-axis is due to the shortening of the distance between the copper ions in the double layer and the apical oxygen. Especially after the tetragonal orthorhombic phase transition the slope of the decrease of this distance increases. That means that in the orthorhombic phase this distance depends more sensitively to the doping level [75] compared to the tetragonal phase). Hence the appearance of the c axis anomaly is still controversial and as other groups also couldn't observe this c axis anomaly it seems that it depends on the special production procedure of the samples from Cava et al. However the charge transfer process suggested by Cava et al. is now universally accepted in that sense that it explains the onset of superconductivity in $YBa_2Cu_3O_{6+x}$. The bond valence sum technique confirmed that the shortening of the c axis is related to the increase of hole doping in the double layer (~ 0.05 holes per Cu-ion in the double layer). Whereas Cava et al. predicts a sudden increase of hole doping the data of Jorgensen et al. may be explained by a smooth increase of hole doping according to their c axis measurements. As mentioned earlier this hole doping is also related to the oxygen chains in the orthorhombic compound. In both

cases this self-doping mechanism leads to a superconducting phase with a T_c that is increasing rapidly after the tetragonal to orthorhombic phase transition. This increase is related to the (sudden) increase of the hole doping in the (then superconducting) double layer. Hence this self-doping mechanism and the hole concentration in the double layer seems to be crucial for superconductivity in $YBa_2Cu_3O_{6+x}$. After this increase around $x = 0.6$ T_c remains constant (T_c around 61K) and forms a first plateau of the T_c versus x diagram of $YBa_2Cu_3O_{6+x}$. A second increase of T_c around $x = 0.75$ is again related to an increase of hole concentration in the superconducting double layer (~ 0.03 holes per Cu-ion in the double layer). Afterwards for increasing x a second plateau is formed around $T_c = 91K$. This is the reason why it is possible to investigate the main doping dependence of the superconducting $YBa_2Cu_3O_{6+x}$-system by investigating the properties at doping levels for both plateaus (for example for $x = 0.6$ and $x = 1.0$).
One important property of the Yttrium Barium Cuprate system are the oxygen chains in the basal plane which act as a charge reservoir for the (superconducting) double layer especially in the orthorhombic phase. This charge transfer seems to be mediated by the apical oxygens whose distance to the copper ions within the double layer depends strongly on the doping level of $YBa_2Cu_3O_{6+x}$ for the orthorhombic phase. A further question is why a gradual increase of the doping level and hence a continuous increase of oxygen chains leads to two pronounced plateaus of the $T_c - x$ diagram. This question leads to the relationship between oxygen ordering in the oxygen chains and the hole concentration in the superconducting double layer. Therefore one has to find first of all a theoretical model of the ordering of the oxygen ions within the oxygen chains for different doping levels. This was especially important as in earlier times (1991) no detailed data on the oxygen ordering for arbitrary doping level was available. However the models which have been made in these times yielded to very important results especially to a understanding of the two plateaus in the $T_c - x$ phase diagram of $YBa_2Cu_3O_{6+x}$. Therefore two different approaches to the problem by Zaanen et al. [43] and Poulsen et al. [76] will be presented here: Zaanen et al. proposes the following model for the oxygen ordering in order to mimic the oxygen ordering in Yttrium Barium Cuprate. First off all they considered the limiting cases. For $x = 0$ no chains are present (tetragonal case), for $x = 0.5$ (already orthorhombic) oxygen chains according to the sequence full - empty - full (doubling of the unit cell along a) are present (the fully-ordered Ortho II phase) and for $x = 1.0$ all chains are full and ordered (the fully-ordered Ortho I phase). For the doping levels in between it was assumed that the chain sequences are empty - partially full - empty for doping levels $x \leq 0.5$ and full - partially full - full for doping levels $x \geq 0.5$. The partially filled chains contain chain fragments with ν copper and $\nu - 1$ oxygen atoms, with $x = 1/2 - 1/(2\nu)$ for $0 \leq x \leq 1/2$ and $x = 1 - 1/(2\nu)$ for $1/2 \leq x \leq 1$ (for incommensurate values a mixture of fragments with different length were considered)[43]. In fact, for $YBa_2Cu_3O_{7.0}$, elec-

tronic charge is transferred from the chains to the planes because both plains and chains give rise to highly dispersive bands crossing the Fermi surface. These structures can be precisely determined by band structure calculations [43], [77]. As these calculations are only possible for well defined (period) structures, for $YBa_2Cu_3O_{6+x}$ with $x < 1$ band structure calculations have been performed using the described model by Zaanen. The main point which came out of these considerations and calculations described above is that only chain fragments which exceed a critical length ($\nu \geq 3$) contribute to the charge transfer process. Whereas smaller chain fragments lead to the remaining of the charge within the oxygen chains (localized states above the Fermi energy). Moreover with this model it was possible to explain the two plateau structure of the $T_c - x$ phase diagram of $YBa_2Cu_3O_{6+x}$. Hence the great achievement of this model was to give a simple explanation to the two plateau structure of the phase diagram just by recognizing that small chain fragments are ineffective dopants. Later, Poulsen et al. [76] also proposed a charge transfer mechanism and combined it with an ASYNNI model. This model is comparable to the asymmetric next-nearest neighbor (NNN) Ising model [43], [78], [79]. The main assumption of Poulsen et al. was to state that only Ortho-I- and Ortho-II-like domains contribute to the charge transfer to the planes. This assumption is similar to the one of Zaanen et al. as it also means that small chain fragments do not contribute to the charge transfer and hence to the doping mechanism. In order to calculate the ground state of the oxygen chain clusters (in this model two dimensional clusters are possible) they used a Monte Carlo calculation. Thus they obtained results which are in good agreement with experimental results. Even so not all details could be explained.
Most of the early experimental work on the superstructure of $YBa_2Cu_3O_{6+x}$ were obtained by TEM-ED. However as the quality of single crystals improved also neutron and x-ray diffraction in order to improve the knowledge on these superstructures became possible. For example Burlet et al. [80] - [82] and Hadfield et al. [83] made extensive studies and found that not only the oxygens in the basal plane were ordered according to a given superstructure but that also the apical oxygen and copper ions within the double layer are involved in the superstructure. In fact the experimental investigations concerning the superstructure of Yttrium Barium Cuprate lasts until nowadays (see chapter 6.6). Here one should explain the difference between coherent Bragg scattering and diffuse scattering. Coherent Bragg scattering is based on the periodic structure of an ideal crystal (given by the unit cell and a Bravais lattice), as such a regular arrangement of atoms leads to well defined (resolution limited) Bragg reflections. In practice coherent scattering occurs (for neutrons and x-rays) within an area in the sample which is called the coherence volume and is characterized by the coherence length which is about some thousands of Angstroms. That means that these techniques average over the structural information within the coherence volume. In the case of long-range ordered structures this leads to coherent Bragg

scattering with sharp (resolution limited) Bragg reflections. However for so-called diffuse scattering the situation is different: The ordered structures are short range (a good example for this type of ordering are the oxygen chains in Yttrium Barium cuprate except for the fully stoichiometric case) ordered and smaller than the coherence volume this leads to diffuse (broad) peaks in the scattering pattern. Nevertheless one can integrate over the volume of these diffuse peaks and treat them afterwards in the same way as normal (coherent) Bragg peaks. In summary the single crystal neutron and x-ray scattering work on the superstructure of oxygen chains in Yttrium Barium Cuprate is diffuse Bragg scattering. Only the fully oxygenated Compound $YBa_2Cu_3O_7$ is considered to be "perfectly" ordered. But even in this case the picture of ideal order should be challenged. Capponi et al. [51] could show that the use of an anisotropic Debye Waller factor for the chain oxygens lead to a significant improvement of the refinement of the diffraction pattern. This was not the case for other atoms. This could be also observed for low temperatures concluding that there exists a static displacements of the oxygen ions within the chains. This observation was further investigated by Francois et al [84]. Instead of refining the anisotropic Debye Waller factor for the chain oxygens he tried the so-called random zig-zag chain pattern. This assumes for the position of the oxygen within the chains in stead of the $1e$ site $(0, 1/2, 0)$ the two-fold position $2k$ $(\pm x, 1/2, 0)$. This position is randomly occupied with the occupancy $1/2$. That means that the oxygen atoms within the chains are randomly shifted along the a axis by $x \cdot a$. This leads to the so-called random zig-zag oxygen chain. In agreement with earlier results from Capponi et al. a large low temperature component could be observed, meaning that there exists a static random zig-zag chain in $YBa_2Cu_3O_{6+x}$. Schweiss et al. [85] made more detailed investigations on single crystals (the former results on the zig-zag chain has been obtained by neutron powder diffraction). In summary he could confirm the results given by neutron powder diffraction. He found that the anisotropic Debye Waller factor along the b axis is comparable to these one of the other atoms. However, for the component along the a axis an extremely large Debye Waller factor appeared which was in addition strongly temperature dependent. He also tried the model from Francois and obtained a temperature independent (low temperature) shift of $x \sim 0.074\mathring{A}$. This zig-zag behavior can be well understood with the following considerations. The formal valence state of the copper ions in the double layer is lower compared to the valence state in the oxygen states. Therefore it follows that the distance between copper ions in the double layer is smaller compared to the same distance within the chains. The buckling of the double layer intensifies this effect. That means the oxygen chains are under a compressive strain which is the reason of the so-called zig-zag chains.

6.1.3 Phase diagram of $YBa_2Cu_3O_{6+x}$

In the previous subsection the T_c curve depending on the doping level x has already been investigated, especially the two plateaus at around $60K$ and $90K$ have been mentioned. In this subsection we will summarize and complete the temperature(T_c)-doping concentration(x) phase diagram of $YBa_2Cu_3O_{6+x}$. Especially the subdivision for different doping levels but also some additional information has been taken from the paper of Regnault et al. [86]. The structure of $YBa_2Cu_3O_{6+x}$ has been discussed in the previous subsection and it has been shown that the differences for different doping levels x occur in the so-called oxygen chains and in the hole concentration in the CuO_2-double layer. The nowadays consensus on the resulting phase diagram of $YBa_2Cu_3O_{6+x}$ depending on the doping level x is summarized in figure 6.4. This

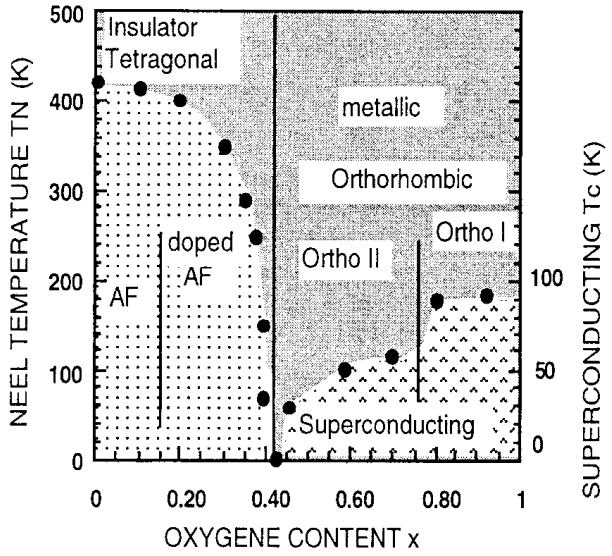

Figure 6.4: This figure shows the superconducting transition temperature T_c versus hole concentration (doping level) x phase diagram of $YBa_2Cu_3O_{6+x}$ on the right side. And the Néel temperature T_N versus hole concentration x phase diagram of the same compound on the left side. For further explanations see the text.

figure shows the division of the phase diagram in two main parts. Below the doping level $x \approx 0.4$ on the left side of the picture the phase diagram of the antiferromagnetic ground state is shown. This ground state persists up to the Néel temperature which depends on the doping level. For these low hole concentrations the crystallographic structure is tetragonal with space group P4/mmm. In that region the substance is more or less an insulator what is explicitly correct for the doping level $x = 0$. At around $x \approx 0.4$ there appears a structural phase transition from the tetragonal phase to the orthorhombic phase with space group Pmmm. From now

on the system behaves more metallic which is explicitly correct for the doping level $x = 1$. This doping range is characterized by a superconducting ground state which appears up to the superconducting transition temperature T_c. The description given above is a highly simplified picture of the system which will be made more and more sophisticated in the following. Concerning the structural aspect the orthorhombic phase is divided further. As described earlier in the previous subsection this is due to the superstructures of the oxygen chains in the basal plane. The superstructure can be characterized by two main (limiting) phases first the Ortho II phase where any second unit cell contains an oxygen ion in the basal plane (strictly spoken this is only the case for $x = 0.5$) and second the Ortho I phase where any unit cell contains a oxygen ion. That means that there are no free places within the unit cell left. Therefore this phase is also called the fully stoichiometric case. And the corresponding crystals are of special quality, as no 'unordered' interstitial places are left. This classification is still quite schematic and further sub-categorization is possible: at $x = 0$ there are no oxygen ions within the basal plane and hence the material is a Mott insulator with an antiferromagnetic spin arrangement. In the underdoped region ($0 < x < 0.2$) the material has been 'doped' with oxygen ions which are installed in the basal plane. They form small Cu_2O-units which are randomly distributed and they already lead to a small net hole concentration in the CuO_2 double layer. However the antiferromagnetic state remains almost unchanged. Within the doped region ($0.2 < x < 0.4$) the oxygen ions are randomly distributed within the basal plane according to the tetragonal symmetry. The charge transfer process from the basal plane to the CuO_2 double layer already increases slightly. This is the so-called doped antiferromagnetic region as the antiferromagnetic order within the CuO_2 double layer still exists, even if more and more holes are present within that layer. This changes at around $x \approx 0.4$. At this doping level preformed oxygen chains (- Cu - O - Cu - O - units) orient along the b axis. That means that the material becomes anisotropic and the tetragonal symmetry changes to an orthorhombic symmetry. At that doping level the doped holes within the CuO_2 double layer are strong enough to suppress the antiferromagnetic arrangement of the spin structure. Slightly above $x = 0.4$ oxygen chain fragments increase and according to the considerations of Zaanen [43] these fragments lead to an increasing hole concentration within the CuO_2 double layer and hence to an onset of superconductivity. Within the slightly underdoped regime ($0.4 < x < 0.5$) the oxygen chains will become longer and longer till the Ortho II state is reached for $x = 0.5$, where every second unit cell a full oxygen chain is present. According to the ideas of Zaanen [43] and Poulsen [76] that is related with a very strong increase of the charge transfer process from the oxygen chains to the CuO_2 double layer. Therefore the hole concentration within the CuO_2 double layer and T_c increases considerably. The doping range ($0.5 < x < 0.94$) is called the strongly underdoped regime. From ($0.5 < x < 0.75$) the first plateau is formed. This can be understood by the simple

models of Zaanen and Poulsen which state that small chains do not contribute to the charge transfer process. Around $x \approx 0.7$ every second oxygen chain becomes again a certain length so that these chains also contribute to the charge transfer process and as a consequence T_c increases again considerable so that around $x \approx 0.8$ the second plateau is reached. This increase is often referred to the 'phase transition' between the Ortho II and Ortho I phase (see figure 6.4). At $x = 0.94$ optimal doping is reached meaning that the maximal superconducting transition is reached: $T_c \approx 93K$. The corresponding samples are called optimally doped. The regime for $(0.94 < x < 1)$ is called the overdoped regime. Within that regime T_c reduces again slightly. For $x = 1.0$ both oxygen chains are completely filled and hence the fully stoichiometric case without any empty places within the basal plane is reached.
Above the underdoped region there appears a so-called Pseudogap. That means that even above T_c the density of electronic states is considerably reduced. This phenomenon is one of the most interesting concerning high temperature superconductors and is still not understood completely (see also 6.3).

6.2 $YBa_2Cu_3O_{6+x}$: a d-wave high T_c superconductor

There are still many things unclear concerning high temperature superconductivity in Cuprates. Especially the underlaying mechanism which leads to the relatively high transition temperatures remains controversial. However a substantial difference between conventional superconductivity in metals like lead ($T_c = 7.2$) and mercury ($T_c = 4.2$) and unconventional superconductivity in ceramics like YBCO ($T_c = 93K$) is the pairing symmetry of the Cooper pairs. Whereas in conventional superconductors this symmetry is of s-wave character, for the high T_c cuprates this pairing symmetry is predominantly of $d_{x^2-y^2}$-wave character. As this difference seems to be important some experiments which give evidence for the d-wave pairing symmetry in high T_c cuprates will be reviewed in this section. Tunnelling spectroscopy [87] as well as angle-resolved photoemission spectroscopy [88] turned out to be strong technics to give that evidence.
Tunnelling spectroscopy is based on the tunnelling effect of quasi-particles and may be performed across a normal metal-insulator-superconductor (NIS) junction. Giaever [89] showed for a standard BCS model that the normalized conductivity in a NIS-junction is proportional to the BCS quasi-particle density of states. Therefore the density of states of a superconductor especially the superconducting energy gab (pairing energy of Cooper pairs, which are responsible for the loss-free super current) can be probed directly by tunnelling spectroscopy. The superconducting energy gap is an energy region above the Fermi level where the density of states

is almost or exactly zero. Within the framework of the BCS theory the value of this energy gap is $2\Delta = 3.54 k_B T_c$ in the weak coupling limit for s-waves. For high T_c the situation is more complicated. Ozyuzer et al. [87] measured the normalized conductivity (normalized to an estimated normal state conductance) of an NIS junction with the optimally doped Tl-2201 ($Tl_2Ba_2CuO_6$, a high T_c cuprate) below T_c. He found very good agreement of his experimental data with a theoretical model assuming $d_{x^2-y^2}$-wave pairing symmetry. Lombardi et al. [90] measured the (critical) Josephson currents (tunnelling of Cooper pairs between two superconductors) of YBCO-YBCO junctions. He tilted the YBCO crystals and thus their macroscopic wave functions with respect to each other. Thus he could measure an angle depending Josephson current related to the d-wave shape of the macroscopic wave functions of both YBCO crystals. By similar experiments Smilde et al. [91] could determined the superconducting gap of YBCO to be of 83 per cent $d_{x^2-y^2}$-wave, 13 per cent isotropic s-wave and 5 per cent anisotropic s-wave pairing symmetry. Moreover, the experiment from Kirtley et al. [92] showed (for YBCO) that the pairing wave function changes sign. This is an important result concerning the fact that this way one can exclude an anisotropic s-wave pairing function for high T_c cuprates. Thus today it is generally accepted that the pairing symmetry in high T_c cuprates is predominantly of $d_{x^2-y^2}$-wave character.

6.3 The pseudogap

The pseudogap has been studied extensively but some questions about it are still under discussion. It is for example controversial whether the pseudogap appears due to competing orders or whether it is a precursor of superconductivity (preformed Cooper pairs without phase coherence). This question might be related to the question whether the pseudogap evolves continuously from the superconducting energy gap or whether the pseudogap and the superconducting gap can coexist. Tunnelling measurements on Bi-2212 ($Bi_2Sr_2CaCu_2O_8$) [93], [94] can be well understood by assuming that the pseudogap originates from the superconducting gap by 'filling in' of states and thus evolves directly from it. However tunnelling [95] and scanning tunnelling spectroscopy [96]-[99] on Bi-2212 support the fact, that the superconducting gap and the pseudogap can coexist. That means that this question has not been studied in a concluding way.

6.4 The out-of-phase phonon buckling mode in $YBa_2Cu_3O_{6+x}$ and superconductivity-induced phonon effects

In that chapter our measurements on the out-of-phase phonon buckling mode will be presented. Here in this section this mode will be introduced and part of the motivation for our measurements will be given. In order to evaluate the strength of the electron-phonon coupling early on after the discovery of the high temperature superconductors phonon neutron measurements have been performed on YBCO.

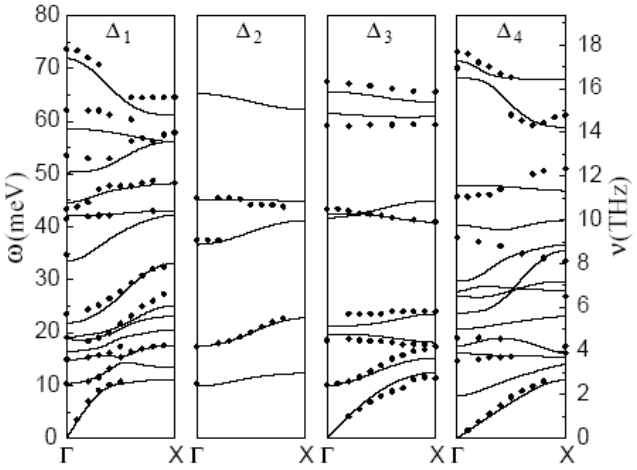

Figure 6.5: This figure gives an overview of the phonon modes with different symmetries (Δ_1, Δ_2, Δ_3, Δ_4) in $YBa_2Cu_3O_{7.0}$. The phonon modes have been measured along the a direction [100] from the center of the Brillouin zone (Γ point) till its boarder (X point). The energy is given in meV on the left and in THz on the right.

Figure 6.5 [100] gives an overview of these measurements. These early measurements have been performed on twinned crystals of $YBa_2Cu_3O_{7.0}$ [100], [101], [102], [103] besides some measurements below 7 THz [101] which have been performed on a quite small detwinned single crystal. Comparable measurements have been made on $YBa_2Cu_3O_{6.0}$ single crystals [100]. This overview on phonon measurements presents most of the phonon modes in YBCO. However there are two special phonon modes which have remarkable properties which are or might be connected to superconductivity. These are the bond-stretching and bond-bending modes where the atoms within the CuO_2 double layer are oscillating. Hence these phonon modes are of special interest as they could be related to interesting phenomena which are connected to superconductivity which takes place within that double layer. Especially the bond-stretching mode have been in the focus of recent research [104]-[108]. In these investigations the energy dispersion relations have been determined. From these investi-

gations [104] and [105] have been inelastic neutron investigations on $YBa_2Cu_3O_{6.6}$ and on $YBa_2Cu_3O_{7.0}$, respectively. The measurements on $YBa_2Cu_3O_{7.0}$ have been performed on an untwinned single crystal, whereas those on $YBa_2Cu_3O_{6.6}$ have been performed on a twinned single crystal. Nevertheless strong anisotropic phonon anomalies could be found for this phonon mode for both materials. The second interesting phonon mode is the bond bending mode (buckling mode) where the Cu-O bounds are bent during the oscillation of the phonon mode. As mentioned above this mode has been investigated on twinned samples on $YBa_2Cu_3O_{7.0}$ [100]. Moreover later more detailed neutron measurements have been performed, where superconductivity induced phonon softening [102] and superconductivity induced line width broadening [103] have been found. All these measurements have been performed on twinned singly crystals.
Recently this phonon mode has garnered attention due to a possible connection to the 'kink' in ARPES measurements [109]. Theoretical calculations revealed the possibility of anisotropic electron-phonon interactions between the buckling mode and antinodal electronic states [110]. However, up to now no anisotropic neutron measurements on the buckling mode have been performed on $YBa_2Cu_3O_{7.0}$ due to the lack on untwinned samples. Moreover one has to state that up to now this mode has only been investigated for $YBa_2Cu_3O_{7.0}$, whereas there does not exist data at the second plateau of the YBCO phase diagram for example for $YBa_2Cu_3O_{6.6}$. We addressed that problem by the preparation of fully detwinned samples for doping levels connected to the two plateaus of the phase diagram of Yttrium Barium Cuprate: $YBa_2Cu_3O_{6.6}$ and $YBa_2Cu_3O_{7.0}$. Thus we could investigate anisotropic superconductivity induced effects of the buckling mode for different doping levels. These new and very interesting results on the buckling mode will be presented in the sections 6.11 and 6.9. In addition to fully detwinned samples these investigations benefit from very high resolutions of the spectrometers (measurements by Reznik et al.: $2meV$, our measurements: 1T1 $1.2meV$, Puma $0.6meV$ FWHM).
After having summarized the motivation for our recent set of measurements on the buckling mode in $YBa_2Cu_3O_{6+x}$, we will give some information about the buckling mode and will summarize elder data on that mode. The phonon buckling mode is a bending mode of the Cu-O bonds within the CuO_2 double layer. The oscillation is maintained by the out-of-phase transversal motion (along the c axis) of the plane (ab plane) oxygens in the CuO_2 double layer. That means that the oxygens along the a direction oscillate with phase shift of 180 degrees with respect to the oscillation of the oxygen ions along the b axis. This is true for both layers of the double layer independently. Moreover oxygen ions of different layers of the double layer oscillate also with a phase shift of 180 degrees (see figure 6.6 [111]). In principle the eigenvectors and frequencies of the buckling mode (at the Brillouin zone center) have been calculated by the use of lattice dynamics models [112], [113]. As the buckling phonon mode is a transversal c axis polarized phonon mode one expects

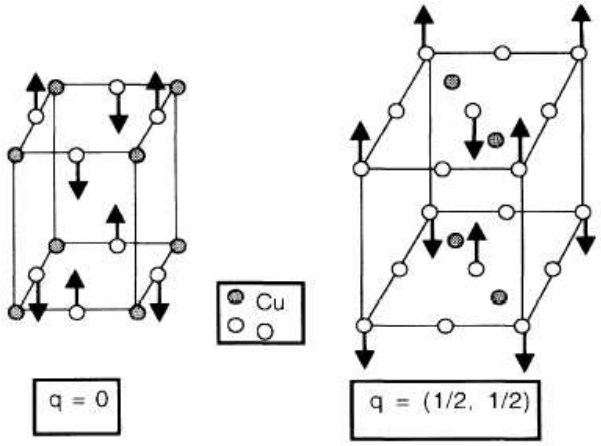

Figure 6.6: In this figure a simplified picture of the unit cell of Yttrium Barium Cuprate is shown. Only the ions within the CuO_2 double layer have been printed as these are the only ions which are involved in the movements of the buckling mode. The phonon eigenvectors (oscillation of the oxygen ions) are given by black arrows for $q = 0$ at the left and $q = (1/2, 1/2)$ at the right.

strong dynamic structure factors for large K_c components. This is due to the factor $[\vec{K}\vec{\varepsilon_j}(\vec{q})]$ in the formula 5.18 of the dynamic structure factor. Moreover, a detailed calculation of the structure factor is given in [111]. There one recognizes that the structure factor is oscillating with respect to K_c and is maximal at around $K_c = 10$, $K_c = 11$ and $K_c = 14$. This dependency has also been investigated experimentally (see figure 6.37).
The buckling mode is a quite flat mode that means it has an almost flat dispersion around $42meV$. That corresponds to 340 cm^{-1} and 10.2 THz. For the orthorhombic compounds the symmetry of the buckling mode is A_{1g}. In the tetragonal compounds its symmetry is given by B_{1g}. Even for the orthorhombic compounds sometimes in the literature one speaks about the B_{1g}-phonon mode by addressing the buckling mode. This is due to the fact that orthorhombic distortions in the lattice structure might be considered as small.
We want to continue with reviewing the most important results on superconductivity induced phonon effects (phonon softening and line width broadening by cooling below T_c) on $YBa_2Cu_3O_{7.0}$. These effects were first observed by Raman scattering [114] - [117]. Altendorf et al. [118] investigated these superconductivity induced phonon effects for different phonon modes with Raman measurements at the center of the Brillouin zone. In addition he compared different doping levels. He found the strongest effects for the 340 cm^{-1} phonon mode which is the phonon buckling mode. This is the reason why this phonon mode attracted special attention in following experiments (including this PhD thesis) which investigated superconductivity in-

duced phonon effects. Altendorf et al. reports a strong phonon softening (around 8 cm^{-1}, 0.99 meV) and a strong line width broadening (also around 8 cm^{-1}) of this mode when cooling below T_C for $YBa_2Cu_3O_{7.0}$. These effects sharply reduce when decreasing the doping level. For $x = 0.95$ the effect is already very weak, whereas for $x = 0.7$ no effect can be observed. For doping levels between $0.7 < x < 0.95$ the line width of the phonon even sharpens when cooling below T_c. This effect is in addition to the line width sharpening due to anharmonic decay of the phonon mode. Phonons usually broaden by heating up due to anharmonic interactions with other phonon modes [119]. Obviously the superconducting phase transition leads to a redistribution of electronic states around the Fermi surface. This redistribution may also affect the electron-phonon coupling and will therefore lead to a shift in the phonon energy (phonon softening) and a line width broadening [103], [120]. The phonon broadening can be understood by the fact that phonons with energies greater than 2Δ can decay by Cooper pair breaking [118], [120] and [121]. Comparison of strong coupling models [121], [122] with the buckling mode lead to the result that the superconducting gap is around the energy of that mode: $2\Delta = 5.4 k_B T_c \approx 340 cm^{-1}$. This might explain the superconductivity induced phonon effects observed for the buckling mode.
In order to investigate these superconductivity induced effects within the whole Brillouin zone the following inelastic neutron measurements have been made. Pyka et al. [102] was the first who observed the energy shift for different phonon wave vectors away from the Brillouin zone center (see figure 6.7). He used a twinned single

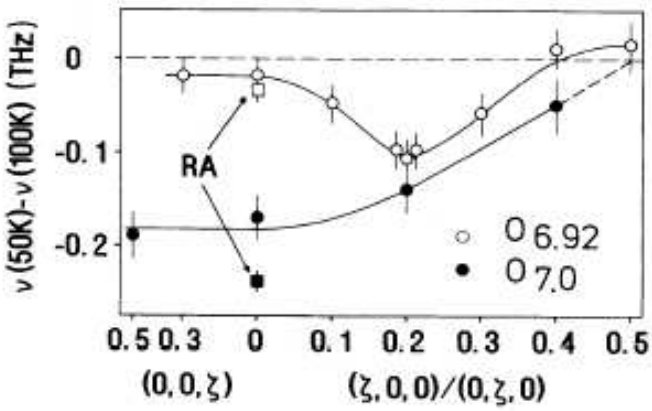

Figure 6.7: This figure shows the superconductivity induced phonon softening (frequency shift) of the buckling mode for different phonon wave vectors which are given in reciprocal lattice units: in-plane [1 0 0], [0 1 0] and along the c axis [0 0 1]. The energy shifts are given by subtraction of the phonon energy at $100K$ and $50K$. Energies are given in THz ($1THz = 4.136\ meV$).

crystal with 0.3 cm^3. Therefore no anisotropic measurements could be made. As the

spectrometer was optimized for high intensity the energy resolution was limited to about 1 THz (FWHM). This is the reason why the phonon line width could not be determined. By investigating the phonon energy for several temperatures between $100K$ and $10K$ he could prove that the energy shift occurs in a narrow range below T_c. Moreover he investigated this energy shift for different doping levels namely for $x = 0.92$ and $x = 1.0$ (see figure 6.7). The full and open squares refer to $x = 1.0$ and $x = 0.87$, respectively. For the optimally doped sample he obtained an energy shift around 0.2 THz at the Brillouin zone center which gradually reduces to zero at the boarder of the Brillouin zone. However for a small decrease in the doping level namely for $x = 0.92$ the energy shift at $q = 0$ reduces to zero. For that doping level the maximal energy shift ($0.1THz$) was found to be at $q = 0.2$ and decreases in both directions towards the center and the boarder of the Brillouin zone. Moreover it was found that this energy shift is independent of q_z, what is shown at the left part of figure 6.7. Reznik et al. reinvestigated this energy shift of the buckling mode. However, due to a much better resolution (around $2meV$) he could also investigate the wave vector dependency of the phonon line width (see figure 6.8). In agreement with the measurements of Pyka et al. they found an energy shift at the center of the Brillouin zone of about 0.8 meV, which decreases gradually towards the boarder of the Brillouin zone along the a axis. Along the diagonal the decrease seems to take place within the first half of the Brillouin zone. This might be a first hint towards an anisotropic behavior of this energy shift. These measurements along the diagonal of the Brillouin zone have been made as Reznik et al. also measured with a twinned single crystal. The second picture below the first one shows the results for the phonon line width within the Brillouin zone along the a direction. One recognizes a clear (superconductivity induced) line width broadening of the buckling mode in the middle of the Brillouin zone around $q = 0.25$. The inelastic neutron measurements on the buckling mode reported here were all made with twinned single crystals.
The following three reason finally justified the reinvestigation of the buckling mode presented in this thesis. First, the superconductivity induced phonon effects have not been investigated upon a possible anisotropy. Second, no doping dependent investigations away from the Brillouin zone center have been made. And third, all the raw data shown in [102] and [103] show only one peak between the energies $37meV$ and $47meV$, namely the buckling mode. However, our measurements with detwinned samples and a resolution of 0.6 meV showed that at least three modes are important within that energy range. And the buckling mode is only one of these. In addition there is at energies above the buckling mode at around $45meV$ a phonon mode involving the oscillation of the oxygens in the double layer and the chains and there is below the buckling mode the in-plane mode of the apical oxygen at around $40meV$. Both modes couldn't be observed within the previously described experiments due to integral effects of the twinned crystals and resolution effects.
There has been a further motivation for our phonon measurements. R. Heid [123]

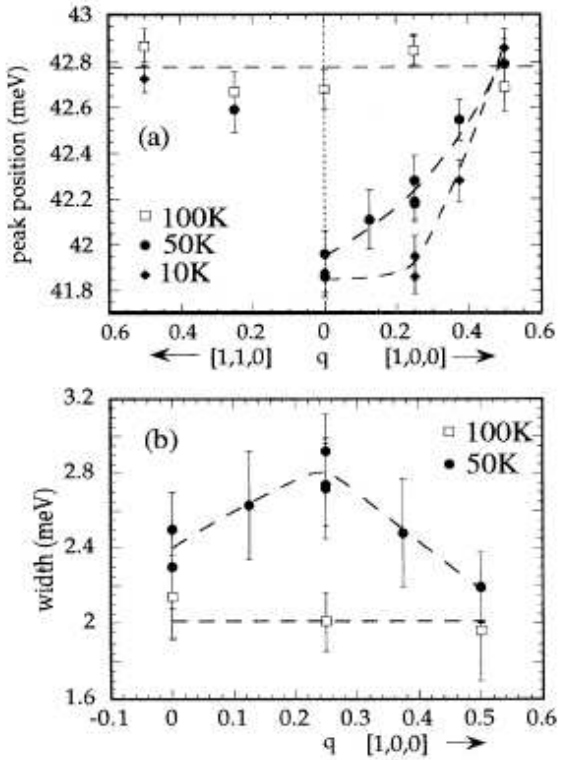

Figure 6.8: This figure shows the dispersion relation (energy shift) and the line width of the phonon buckling mode at different temperatures at $10K$, $50K$ below $T_c \approx 93K$ and at $100K$ above T_c. The measurements have been performed along the a axis [1 0 0] and along the diagonal [1 1 0] within the Brillouin zone. The energies are given in meV. The dashed lines are guides to the eye.

calculated the dispersion relation and the line width of the phonon buckling mode. As a result he obtained a very strong electron phonon coupling and hence a big line width for the buckling mode. This broadening due to the electron phonon coupling is maximal at the center of the Brillouin zone and reduces towards the middle of it considerably. In summary these calculation showed that the buckling mode performs a very strong coupling to electronic states compared to other phonon modes in YBCO.

6.5 Kink in ARPES and possible relation to the phonon buckling mode: electronic states in the cuprates and the electron-phonon interaction

The (strong) electron phonon coupling has already been discussed from the phonon point of view and the corresponding energy shifts and line width broadenings have already been discussed in the previous section. Now the situation will be discussed from the other point of view: is there evidence for strong electron-phonon coupling by the investigation of the self energy of the corresponding electrons?
In order to evaluate this question the review article of Zhou et al. [124] has been used as a source of information. The appropriate technique for these investigations of electronic states in cuprates is angle-resolved photoemission spectroscopy (ARPES). Before reviewing the important research which might give an answer to the above question, ARPES and the electronic structure of the cuprates will be shortly presented. The mechanism of ARPES is quite easy: Photons from the light source (for example synchrotron radiation source) excite electrons in the bulk which are emitted at the surface as photoelectrons. The energy analyzer measures the intensity of the photoelectrons for different energies and emission angles. The corresponding data set is a so-called energy distribution curve (EDC). During the emission process the energy and momentum is conserved. Thus the initial energy of the electron can be calculated by the knowledge of the phonon energy, the work function and the measured kinetic energy of the photoelectrons. The initial momentum of the electron (parallel to the sample surface) depends on the kinetic energy and the emission angle of the photoelectrons. Thus the measurement of the EDC provides in principle the full information on the electronic states of two-dimensional materials (for examples the cuprates). Hence the measured intensity depending on the initial energy and momentum of the electrons in the material $I(k,\omega)$ (given by the EDC) is proportional to the single-particle spectral function $A(k,\omega)$

$$I(k,\omega) \sim A(k,\omega)|M|^2 f(\omega), \tag{6.1}$$

where $|M|$ depends on initial energy and polarization of the phonons, on the measuring geometry and on the instrumental resolution. The Fermi function is given by $f(\omega)$. In the normal state the single-particle spectral function depends on the real and imaginary part of the electron self-energy Σ. In other words the peak position of the EDC determines the real part of the self-energy and the line width of the EDC determines the imaginary part of the self-energy, namely the quasi-particle lifetime. Most of the electronic structure of the cuprates has been investigated by ARPES measurements. In the following paragraph the electronic structure of cuprates will

shortly be summarized. Superconductivity takes place in the CuO_2 double layer of doped cuprates and hence its electronic structure is of special interest. First we will discuss the electronic structure of the undoped cuprates (antiferromagnetic Mott insulators) and afterwards we will generalize the situation for doped compounds. Such a CuO_2 layer consists of corner shared CuO_4-squares. That means a Cu^{2+} ion is surrounded by four O^{2-} ions. Whereas the oxygen ion has a closed 2p-shell the highest 3d-orbital $d_{x^2-y^2}$ of the copper ion is half filled by an electron. The degeneracy of the five d-orbitals is repealed by a crystal field due to the oxygen ions. As the $d_{x^2-y^2}$-orbital points directly to the neighboring oxygen ions which are negatively charged this orbital has the highest energy. Moreover this (half-filled) d-Orbital and the upper most (filled) p-orbitals of the oxygens hybridize with each other. Finally the highest (half-filled) orbital is the σ^* anti-bonding orbital. According to band theory the corresponding valence band is half filled. That means the undoped cuprates should be metals. However they are so called Mott-insulators. The electronic structure of these materials is altered due to the strong electronic correlations. If the highest d-electron which can be considered localized at a copper ion hops to a neighbor and fills the half-filled d-orbital of that neighboring copper ion it needs the Hubbard energy U because of the Coulomb repulsion of both electrons (strong electronic correlations). That means within 'the' highest d-band there are electronic states which are separated by the Hubbard energy U. In other words the highest d-band in strongly correlated electron systems like the cuprates is split in a upper Hubbard and a lower Hubbard band. In between these two bands the highest p-band of the oxygens appears (This is true for the cuprates. For vanadates and titanates it is below the lower Hubbard band), which has a mean energy distance of Δ from the upper Hubbard band. This energy is called the charge transfer energy. The highest p-band and the lower Hubbard band are completely filled, whereas the upper Hubbard band is empty. That means only if electrons can overcome the charge transfer gap the Mott-insulator becomes conducting. Therefor the undoped cuprates are called charge transfer insulators. Now the question appears what happens when these Mott-insulators are doped. As explained in section 6.1.1 the CuO_2 double layer is doped with holes for increasing doping level. Formally the holes appear at the oxygen p-orbitals. Moreover the spins of the oxygen p-orbital and the $d_{x^2-y^2}$-orbital form a bound state a so called Zhang-Rice singlet. The corresponding Zhang-Rice singlet band is located directly above the filled p-band of the oxygen ions. This way the cuprates become metallic and superconductivity can occur. Thus doping in the cuprates leads to a metal-insulator phase transition. The corresponding theoretical model which describes the splitting of the $d_{x^2-y^2}$-band is called the Hubbard model. This is the standard model in order to explain the effects of strongly correlated electron systems.

Electron-phonon coupling in strongly correlated electron systems has not yet been developed [124]. However one can use the undoped cuprate which is a Mott insulator

as a starting point and may consider what happens due to hole doping. The doped holes in these compounds have only very few energy which can be assumed to be smaller than the phonon energy. Then these holes can be considered as polarons, that means holes with a surrounding phonon cloud. The mass of these polarons can become very big (corresponds to strong coupling) so that they can localize at impurities. Due to comparisons with experimental data the coupling constant for undoped cuprates corresponds to that strong coupling regime. Thus one can understand why the slightly doped cuprates are still insulators even if there is a finite doping concentration. However the weak coupling regime can be better understood by perturbation theories (Migdal-Eliashberg theory). In that regime the electron-phonon coupling is due to single phonon excitations (compared to the strong polaron regime, where 'several' phonons couple to one hole) which lead to a renormalization of the bare band dispersion and a finite lifetime of the phonon. This finite lifetime corresponds to the intrinsic phonon line width. To be correct it is the intrinsic line width broadening in addition to the already finite line width due to anharmonic phonon interactions. However for decreasing temperatures this effect becomes smaller (see for example [118]; Altendorf et al. calculated this anharmonic line width broadening and compared it with the measured line width by Raman measurements for different doping levels in the system $YBa_2Cu_3O_{6+x}$. Thus he could show that there appears a pronounced superconductivity induced line width broadening).
Along the nodal direction (the diagonal in the Brillouin zone, where the d-wave gap is zero) in the Brillouin zone the ARPES spectra of hole doped cuprates ($Bi_2Sr_2CaCu_2O_8$ (Bi2212), $Bi_2Sr_2CuO_6$ (Bi2201) and $La_{2-x}Sr_xCuO_4$ (LSCO)) show a pronounced kink in the dispersion relation at around 50-70meV. This kink is present above and below T_c and is observed for various doping levels, whereas it is stronger in the underdoped region compared to higher doping levels [125]-[131]. Figure 6.9 shows this kink for different high temperature superconductors (a-c), different temperatures (d, e) and different doping levels (a-c). Moreover in the final picture (f) the doping dependence of the effective electron-phonon coupling strength λ' along the nodal direction is shown. Lanzara et al. [126] and Zhou et al. [124] relate this kink along the nodal direction to the half-breathing mode, which shows an anomaly in neutron experiments on $La_{2-x}Sr_xCuO_4$ (LSCO) [132], [133]. Similar phonon anomalies have also been observed for $YBa_2Cu_3O_{6+x}$ (see section 6.7). A good argument for that relation are the isotope induced changes of the nodal dispersion in optimally doped ($Bi_2Sr_2CaCu_2O_8$ (Bi2212) [131]). However, there are also good arguments to relate this kink to the magnetic resonance peak or to related magnetic excitations [127], [128]. Therefore this issue is still highly controversial.
Even more interesting for our research and the question above is the recent discovery of a kink within the antinodal region (This is where the superconducting gap is maximal) of the Brillouin zone in Bi2212. This kink appears only below T_c at about 40meV, which is at lower energies compared to the nodal kink [134]. Moreover it is

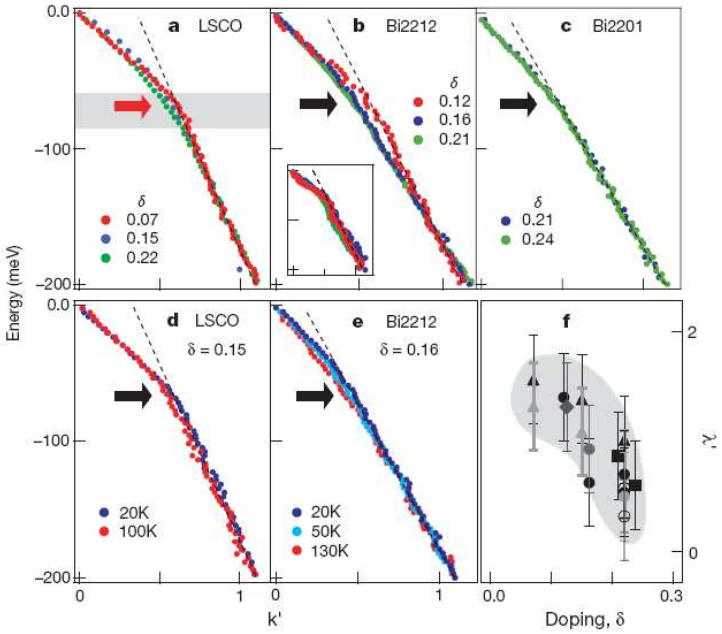

Figure 6.9: This figure shows the kink in the dispersion relation of different high temperature superconductors with different doping levels (a-c) obtained by ARPES. The temperature independency of this kink is shown in figures (d) and (e). Figure (f) shows the effective electron-coupling constant with respect to the doping level for LSCO (filled triangles), Nd-doped LSCO (filled diamonds), Bi2201 (filled squares) and Bi2212 (filled and unfilled circles).

strong near the antinodal point $(\pi, 0)$ and it becomes much weaker if the momentum moves away from this point. The interesting point about that kink is the fact, that it appears at the antinode where the superconducting gap is maximal. Hence this kink may be related to the mechanism of high temperature superconductivity [124]. Again there are at least two possibilities of attributing this kink to excitations in high temperature superconductors. Kaminski et al. [127] and Kim et al. [135] attribute this kink to the magnetic resonance effect. However, Cuk et al. [109] could observe this kink in optimally doped Bi2212 also above T_c and is therefore convinced that it is due to the coupling to the B_{1g} buckling mode instead of the resonance mode. Moreover he found that this kink is more extended within the Brillouin zone then Gromko et al. reported. In summary Cuk et al. and Devereaux et al. related that antinodal kink with the B_{1g} buckling mode by a full Migdal-Eliashberg calculation [110] using a tight-binding model for the band structure. Moreover they claim that therefore the B_{1g} buckling mode is essential in explaining the mechanism of Cooper pair building in high temperature superconductors [124]. These new developments were a main motivation for us to reinvestigate the superconductivity induced phonon

effects of the B_{1g} buckling mode in the system $YBa_2Cu_3O_{6+x}$.

6.6 The oxygen chains in YBCO

In the subsections 6.1.1 and 6.1.2 the important role of the oxygen chains (superstructure, doping reservoir) has already been discussed. Nevertheless they are still a matter of current research. A recent diffuse x-ray study of underdoped $YBa_2Cu_3O_{6+x}$ [136] found an anomaly around the pseudogap temperature which was attributed to charge stripe order. Later a similar study has been performed for optimally doped $YBa_2Cu_3O_{6+x}$ where a four unit cell superstructure could be found. This diffuse x-ray scattering decreases almost linearly and exists up to around $500K$ [137]. These data have also been interpreted in view of a possible charge stripe formation within the CuO_2 double layer. As far as one concerns the experimental evidence these measurements are consistent with those of Strempfer et al. [138], which have been done concurrently and lead also to the result, that there exists a four unit cell superstructure in optimally doped $YBa_2Cu_3O_{6+x}$. However, they attribute this experimental evidence uniquely to the existence of the oxygen chains. This argument is strengthened by the fact that a Calcium doped material with the same intrinsic doping (same oxygen content) shows the same diffuse x-ray pattern, even if the hole concentration within the double layer is different from that of the usual optimally doped $YBa_2Cu_3O_{6+x}$. Moreover they report that this diffuse x-ray scattering does not appear in the high temperature superconductor $YBa_2Cu_4O_8$, which does not have any oxygen chains. Thus it is indeed justified to assume that this diffuse x-ray scattering is due to the oxygen chains and not on account of charge stripe formation within the CuO_2 double layer. However, it is clear that the superstructure involves atomic displacements within the whole unit cell and thus can also affect the CuO_2 double layer.

6.7 Phonon anomalies in high temperature superconducting cuprates

Phonon anomalies in high T_c superconductors have been extensively reviewed by L. Pintschovius in his review article [139] from page 5 up to 13. However here the most important and interesting results will be summarized. It might be that these results are related to our results on the buckling mode presented in this PhD thesis in the following sections 6.9 and 6.11. The anomalous features reported so far on phonon modes in cuprates are observed for the so called bond-stretching modes. This bond-stretching mode has been studied for the system $La_{2-x}Sr_xCuO_4$ for the undoped ($x = 0$) till the overdoped ($x = 0.3$) sample. Anomalous means for that

compound that the energy dispersion softens considerably from the center of the Brillouin zone till its middle and hardens again to the initial value at $q = 0$ towards its boarder. This anomalous softening can not be explained by phenomenological shell models and corresponds therefore to a renormalization of the phonon energy. And it is stronger along [1 0 0] compared to [1 1 0]. It can be observed from the underdoped ($x = 0.1$; around $15meV$ of phonon softening) till the overdoped sample (around $20meV$ of phonon softening) and becomes stronger with increasing doping level [139], [100], [140].

The situation in $YBa_2Cu_3O_{6+x}$ is similar compared to the results reported for

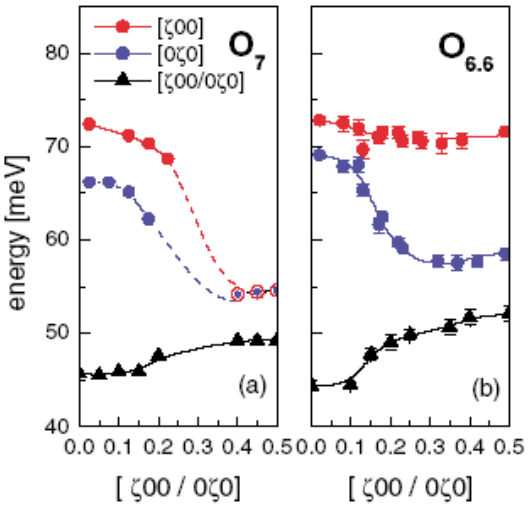

Figure 6.10: This figure shows the anomalous bond stretching vibration in the system $YBa_2Cu_3O_{6+x}$ at $10K$. The measurements for the overdoped compound are shown at the left, whereas those for the underdoped compound are shown at the right. For the underdoped compound this phonon mode is strongly anisotropic.

$La_{2-x}Sr_xCuO_4$. For underdoped $YBa_2Cu_3O_{6.6}$ there could be observed a certain energy renormalization compared to calculations [140] and with respect to the underdoped compound $YBa_2Cu_3O_{6.0}$ [141] for the bond-stretching vibrations. However only along the b direction an even stronger anomalous decrease of the dispersion relation at around $q = 0.25$ takes place [104] (see figure 6.10). This energy renormalization is strongly anisotropic. In figure 6.10 the anomalous bond stretching vibrations measured along the a^* (red) and along the b^* direction (blue) are shown together with a bond bending vibration (black). At the right the results for the underdoped material $YBa_2Cu_3O_{6.6}$ are shown, whereas the left shows the same modes for the overdoped sample $YBa_2Cu_3O_{7.0}$. These measurements for $YBa_2Cu_3O_{7.0}$ show also a strong decrease of the dispersion relation [105]. However for this compound the energy renormalization does not seem to be strongly anisotropic.

6.8 Stripe theory in high temperature superconductors

Tranquada et al. [142] observed static stripe order (spatial modulations of spin and charge density) in $La_{1.48}Nd_{0.4}Sr_{0.12}CuO_4$. Since then the relation between high T_c superconductivity and stripes are discussed. According to Pintschovius et al. [139] the stripe picture for high T_c superconductors can only be uphold if one can find evidence for dynamic stripe order in the cuprates. These dynamic stripes can be observed by their coupling to phonon modes. According to Pintschovius the strong energy renormalizations in the bond stretching modes (see section 6.7) are due to coupling with dynamic stripes. However this assumption and further evidence for spin stripes in high T_C superconductors [143] is highly controversial. However, if dynamic stripes are present in high temperature superconductors, they should be observed due to their coupling to phonon modes which will then and change their intrinsic line width. Moreover these effects should be strongly anisotropic.

6.9 Measurements on $YBa_2Cu_3O_7$

Our measurements of the phonon buckling mode in $YBa_2Cu_3O_7$ has been made at the Puma spectrometer at FRM II. This spectrometer is also a thermal triple axis spectrometer optimized for inelastic neutron scattering in the thermal energy range. Compared to 1T1 at Saclay the Puma spectrometer yields an even better energy resolution (below one meV). This together with a relatively high neutron flux turned out to be crucial for our measurements on $YBa_2Cu_3O_7$.
For our measurements reported in this section our $YBa_2Cu_3O_7$ sample was enlarged, so that it finally consists of 185 crystals with a total mass of 2.63 g. However it should be stated that part of the measurements were made with a 1.8 g sample. In any case the data have been normalized to a sample mass of 1.8 g and a monitor counting rate of 7200000 counts. So the intensities of all our phonon scans within this section may be compared. Besides the higher mass the sample is the same with which the neutron spin echo measurements reported in the next chapter has been performed. Therefore the preparation process and the quality of the sample will be discussed in the following chapter (see section 7.1 for the preparation). In general the quality of our single crystal is relatively high. One reason is that it consists of small single crystals, that means inclusions and homogeneities are improbable compared to bigger single crystals comparable to the total mass of our sample. Moreover, here we dealt with an almost fully stoichiometric sample which can be regarded as a 'perfect single crystal' without defects (in reality our sample has the doping level $YBa_2Cu_3O_{7-\delta}$ with $\delta \leq 0.05$). This leads again to more regular and homogeneous single crystals compared to doped ones. Another important point of the quality of

the single crystals is how good they have been detwinned. This will be shown in section 7.2. Moreover, the observed strong anisotropies of the phonon buckling mode which could be observed, proves impressively that our sample has been detwinned adequately. Here it should be mentioned that the detwinning process becomes more and more difficult for higher doping levels (higher oxygen contents). This is due to the anisotropic oxygen chains. Whereas for lower doping levels one detwinning procedure is often enough to get a detwinned single crystals for our $YBa_2Cu_3O_{7.0}$ sample for each detwinned single crystals two to three detwinning procedures were necessary.

6.9.1 Introduction

The following anisotropic phonon measurements of the phonon buckling mode (42 meV branch) on our $YBa_2Cu_3O_{7.0}$ sample has been made with the triple axis spectrometer Puma at the FRM II from January 29^{th} till February 4^{th} (1.8 g) and from June 8^{th} till June 13^{th} 2007 (2.6 g). The sample consists of small single crystals having been fully detwinned and aligned as a mosaic on an aluminium plate. The mosaicity of the sample is around 1.5 degrees (this value has been determined for the a and the b axis with the TRISP spectrometer for the sample with 2.6 g; the spectrometer resolution of 0.4 degrees has been considered; the exact values were 1.42 along the a direction and 1.59 along the b direction). The lattice constants are $a = 3.82\ (3.79)\mathring{A}$, $b = 3.89\ (3.86)\mathring{A}$ and $c = 11.68\ (11.61)\mathring{A}$ (The values in brackets have been obtained during the sample alignment with the Puma spectrometer for the sample with 2.6 g). The superconducting transition temperature of the sample is $T_c = 90\text{K} \pm 0.5K$ (this is the value which has been determined by susceptibility measurements at the Physical Property Measurements System (PPMS) at MPI; it is the averaged value of some selected single crystals which have been used for our sample).
As described in section 6.4 the phonon buckling mode is a transversal phonon polarized along the c axis, with the in plane oxygens of the CuO_2 - double layer oscillating out of phase. As a consequence the (dynamic) structure factor for this phonon mode has a local maximum around $K_c = 10$ and 11. Therefore we made our measurements adjacent to the reciprocal lattice vector $\vec{K} = (1, 0, 10)$ and $(0, 1, 10)$ for the phonon measurements along the a and b axis, respectively. At $K_c = 11$ we couldn't measure as this position in reciprocal space was not achievable with the Puma spectrometer. It was possible to distinguish between the a and the b direction due to our fully detwinned sample. The phonon wave vectors q_a and q_b for the measurements along the a and b axis, respectively, are measured with respect to the reciprocal lattice vectors given above. The sense of rotation of the spectrometer was (-1 1 -1) and we used the Cu220 Monochromator and the PG 002 Analyzer. Using the Cu220 monochromotor was essential in order to reach resolutions below $1meV$. The spec-

trometer resolution has been calculated with the program RESCAL. Doing so, we obtained an energy value of $0.6 \pm 0.4meV$. This unrivalled spectrometer resolution for our constant $\vec{K}$-scans could be achieved by using a quite small value as fixed final energy: $8meV$. This reduced the spectrometer resolution again compared to higher standard values for the final energy. The error of the energy measurements during our measurements is around $0.3meV$. In order to reach temperatures down to $3K$ we used a CCR cryostat in the first period of our measurements. However in order to have a better temperature control in the second part of our measurements we cooled down to $4K$ using the standard cryostat from the Puma spectrometer. In order to suppress spurious speaks we used two graphite filters and we checked any configuration for lambda half and lambda third spurious peaks from the monochromator and the analyzer, respectively. We even performed temperature dependent spurion checks for $q_b = 0.3$ in order to ensure that there does not occur a temperature dependent spurious peak. This was especially necessary as we observed this time a quite interesting temperature dependency of the phonon buckling mode at that specific reciprocal lattice point.
In January, we made our measurements for the following phonon wave vectors: q_b = 0.15, 0.2, 0.25, 0.3, 0.4, 0.5 along the b axis and q_a = 0.15, 0.25, 0.3, 0.35, 0.4, 0.5 along a. Along the b axis we measured at $3K$, $120K$ and $305K$ and along the a direction at $3K$ and $120K$. In order to complete our measurements from January in June we made measurements for the following phonon wave vectors: $q_b = 0$, 0.05, 0.1 along the b axis and $q_a = 0$, 0.1 along the a axis at $4K$ (below T_c) and $100K$ (above T_c). Where q_a and q_b are the in-plane (within the superconducting double layer) wave vectors with respect to the reciprocal lattice vectors given above. That means for example $q_a = 0.15$ = q = (0.15, 0) and $q_b = 0.15$ = q = (0, 0.15). In summary we now have a full data set of the buckling phonon mode within the whole Brillouin zone for both in-plane directions at temperatures below and above the superconducting transition temperature. In addition to these measurements in June we made a detailed temperature study for the phonon wave vector $q_b = 0.3$ where the T_c - induced broadening effect of the phonon mode was biggest. We made our measurements at $5K$, $10K$, $20K$, $30K$, $40K$, $50K$, $60K$, $65K$, $70K$, $75K$, $80K$, $85K$, $90K$ below T_c and at $95K$, $100K$, $105K$ above T_c . Together with our measurements at $120K$, $200K$ and $305K$ from January we now have a detailed temperature study of the phonon buckling mode with $q_b = 0.3$.
Initially we made the temperature study in order to prove that the anisotropic line width broadening for $q_b = 0.3$ is a T_c - induced effect due to the increase of the electron phonon coupling. However, our temperature study revealed due to the very good resolution of the Puma spectrometer that this is no real broadening but that there are two phonon modes. That means that we have compared to previous measurements [103] three different phonon modes in the energy range from $38meV$ up to $48meV$ (see figures 6.11 and 6.12). At high energies we see a well resolved peak

at around $45meV$. This is a c-axis polarized plane chain mode of the oxygen ions within the CuO_2 - double layer and the chain oxygens. This has been found by comparing the energies of this mode with previous neutron and infra-red measurements, as this mode is infra-red active [144]. Another phonon mode an in-plane mode of the oxygens in the CuO_2 - double layer, has also the correct energy at the Brillouin zone center to account for third phonon mode. However, this mode has been intensively studied by Pintschovius [104] and it was found, that this mode disperses upwards. Moreover, we calculated the structure factor of this phonon mode for our experimental conditions and we obtained a rather low value which could not explain our experimental observations. Therefore we believe that we did not observe this in-plane mode but the previously described plane chain mode. This mode would also explain the fact, that we couldn't observe it for the antiferromagnetic sample and only along the chain direction for the superconducting underdoped sample. As this mode involves the oscillation of the chain oxygens this behavior can be easily understood. For lower energies and $q = 0.3$ a double peak structure can be seen. Here one clearly observes two peaks. Finally the phonon buckling mode is the middle peak of the three observed ones and the mode with lowest energy is the in-plane mode of the apical oxygen (see figure 6.12). This could be found by the comparison of our neutron data with Raman measurements [145](see figure 6.11, this figure shows moreover the eigenvectors of the buckling and the apical oxygen mode).
These new findings mean that the phonon buckling mode for $q = 0.3$ does not broaden below T_c for the b direction and only slightly for the a direction. However this mode behaves strongly anisotropic for $q_b = 0.3$. This has a simple reason: the apical mode along the a direction is at a different energy compared to that of the buckling mode, whereas along the b direction both modes the apical in-plane mode and the buckling mode are in close vicinity [144]. This vicinity has very interesting consequences: the intensity of the buckling mode along the b direction (for $q_b = 0.3$) looses much of its intensity by cooling below T_c whereas the neighboring apical mode at lower energies (for the b direction) hardens and gains a comparable amount of intensity (see figure 6.12). This remarkable effect depends not only on the direction but is strongly q-dependent. The observation of this anisotropic T_c-related interaction of the buckling phonon mode with the apical phonon mode at lower energies was only possible due to two important reasons: first due to the high resolution of the Puma spectrometer and second due to the fully detwinned sample of $YBa_2Cu_3O_7$. In former experiments [103] one could not resolve these three peaks but measured a single broad peak. Thus the situation changed impressively from an anisotropic T_c induced broadening effect to the anisotropic T_c induced change of the phonon eigenvector (of the buckling phonon mode). Up to now and according to our knowledge this has not been reported so far in literature. Our temperature study mentioned above yields a detailed picture of this T_c induced effect for $YBa_2Cu_3O_7$. However, the investigation of the doping dependence of this effect exceeds this the-

sis and remains for further investigations. Unfortunately for the measurements with our $YBa_2Cu_3O_{6.6}$ sample, we cannot make a statement about this effect as we could not resolve all three peaks clearly from each other (see figure 6.24). However these measurements are consistent with the picture described above that there exist three phonon modes. This would mean that the in-plane apical oxygen mode and the buckling mode represent the broad peak at lower energies, whereas the peak at higher energies could be resolved from the buckling mode and represents the plane chain mode.
Besides the anisotropic T_c effect described above with our following measurements we could also confirm another T_c effect which has already been described previously [103]. At $q = 0$ the phonon buckling mode shows a superconductivity induced softening for both in-plane directions. See figure 6.17 for the b direction (below) and the a direction (above), respectively. Moreover these figures show, that away from the Brillouin zone center this effect becomes slightly anisotropic. For increasing wave vector from the Brillouin zone center to its boarder this softening effect reduces towards the boarder of the Brillouin zone.

Resolution of the Puma spectrometer

In analogy to the resolution calculations for 1T1 the resolution of the Puma spectrometer has been calculated with Rescal (see subsection 6.11.2). As result we obtained 0.6 meV, which is half the value of the resolution we calculated for 1T1. This is the value one obtains if one projects the resolution ellipsoid (see chapter 5.5) in four dimensional energy-momentum space onto the energy axis. Similar to the specific parameters of 1T1 here the parameters for the Puma spectrometer will be presented. We calculated the resolution with Rescal according to the method of Popovici. First of all we inserted the monochromator and analyzer d-spacing $d_{mono} = 1.278\mathring{A}, d_{anal} = 3.354\mathring{A}$, which can be calculated knowing the lattice constants and the Bragg reflection. Next the mosaicities of the monochromator, the analyzer and the sample were required. For the monochromator and the analyzer the mosaicity is 27.6 minutes and 47.4 minutes, respectively, and for the sample 90 minutes. The scattering sense of the spectrometer was for all our measurements -1 for the monochromator, 1 for the sample and -1 for the analyzer. We measured with fixed final energy which corresponds to a final scattering vector $\vec{k}$ of $1.97\mathring{A}^{-1}$. All the horizontal collimations were two degrees, whereas the vertical collimations were three degrees. For Popovici's method the following parameters were necessary in addition to these one already mentioned. First we had to specify that we have a rectangular source with a width of 2 cm and a height of 13 cm. We didn't use guides. Moreover we used a flat-plate sample with dimensions $0.2 \times 2 \times 2$ cm^3 and a circular detector with a diameter of 2.54 cm^2. The dimensions of the monochromator are

$0.2 \times 26 \times 16.2\ cm^3$ and the analyzer are $0.2 \times 21 \times 15\ cm^3$. The distances LO (source to monochromator), L1 (monochromator to sample), L2 (sample to analyzer) and L3 (analyzer to detector) were $209, 215, 90$ and $90\ cm$. The horizontal and vertical focussing of the monochromator were $0.236\ 1/m$ and $0.944\ 1/m$, respectively, and for the analyzer the horizontal and vertical focussing were $0.562\ 1/m$ and $0\ 1/m$, respectively.

Fitting function for our constant $\vec{Q}$-scans: Voigt functions

All our measured data have been fitted with Voigt functions. The Voigt function is a convolution of a Gaussian and a Lorentzian function. In general the intensity $I(\omega_0, \vec{K}_0)$ of a triple axis spectrometer is given by equation 5.27:

$$I(\omega_0, \vec{K}_0) \sim \int d\omega d\vec{K} R(\omega - \omega_0, \vec{K} - \vec{K}_0)\ S(\vec{K}, \omega). \tag{6.2}$$

That means the Intensity is proportional to the four dimensional convolution of the spectrometer resolution function $R(\omega - \omega_0, \vec{K} - \vec{K}_0)$ and the scattering function $S(\vec{K}, \omega)$. The resolution function is given by a four dimensional Gaussian distribution 5.29:

$$R(\omega - \omega_0, \vec{K} - \vec{K}_0) = R_0 \exp(-\frac{1}{2}\Delta\kappa M \Delta\kappa), \tag{6.3}$$

(see chapter 5.5 for explanations) which can be visualized by the resolution ellipsoid. The scattering function for phonons can be modelled by the model of the damped harmonic oscillator, where Γ is the intrinsic line width of the corresponding Lorentzian function:

$$S(\vec{K}, \omega) \sim \sum_{s=\{\vec{q},j\}} \sum_{\vec{G}} \frac{F^2(\vec{K}, \vec{q})}{2\omega'_s} \tag{6.4}$$

$$\left[\langle n(\omega'_s) \rangle \frac{1}{\pi} \frac{\Gamma_s}{[\omega + \omega'_s]^2 + \Gamma_s^2}\ \delta(\vec{K} \pm \vec{q} - \vec{G}) \right], \tag{6.5}$$

where $F(\vec{K}, \vec{q})$ is the dynamic structure factor:

$$F(\vec{K}, \vec{q}) = \left| \sum_d \frac{b_d}{\sqrt{M_d}} \exp(i\vec{K}\vec{r_d}) [\vec{K}\vec{\varepsilon_j}(\vec{q})] \exp -W_d(\vec{q}) \right|, \tag{6.6}$$

(see equation 5.16 - 5.19).
The Bose factor

$$\langle n(\omega'_s) \rangle = \frac{1}{1 - exp(-\hbar\omega'_s / k_B T)} \tag{6.7}$$

depends on the energy and on the temperature. It was considered by correcting the raw data, so that it hasn't to be considered for the fitting function. Now it is

necessary to remind Bragg's law. Considering the spectrometer resolution function and inelastic scattering it reads

$$\vec{K_0} = \vec{G} + \vec{q}. \tag{6.8}$$

Here $\vec{K_0}$ is the momentum where the spectrometer measures best. So aligning the sample means assigning this point to (which is here modified because of inelastic scattering) a reciprocal lattice vector (see chapter 5.1). As our measurements were constant $\vec{K_0}$-scans (see chapter 5.3) that means that this quantity is kept constant during the whole measurement. This is not true for the energy, ω_0 is lower than ω_s at the start of the scan and is higher than it at the end of the scan. Our phonon mode is almost not dispersing that means ω_s can be considered as a constant. Than the intensity during the energy scan (for one phonon mode and except the Bose factor and proportionality constants) is given by the following equation depending on ω_0:

$$I_{\omega_s}(\omega_0) \sim \int d\omega S(\omega + \omega_s) \tag{6.9}$$

$$\int d\vec{K} R(\omega + \omega_0, \vec{K} - \vec{K_0})\, F(\vec{K}, \vec{q})\, \delta(\vec{K} \pm \vec{q} - \vec{G}). \tag{6.10}$$

ω_0 is considered to be negative as ω_s is. This intensity distribution $I_{\omega_s}(\omega_0)$ is the quantity which has been measured during our measurements of the phonon buckling mode on the triple axis spectrometer Puma. Solving the integral over $d\vec{K}$ using the property of the δ-function yields directly

$$I_{\omega_s}(\omega_0) \sim \int d\omega S(\omega + \omega_s)\;\; R(\omega + \omega_0). \tag{6.11}$$

However this needs as a precondition that the excitation in $\vec{K}$-space is perfectly sharp. However if one assumes a finite length scale, this leads to a $\Delta\vec{K}$ in the resolution function. To estimate this effect the resolution ellipsoid has been calculated by Rescal for spectrometer conditions during the scan. The axis of the resolution ellipsoid for the momentum directions are much smaller than the energy axis. That means the ellipsoid is cigar-shaped with the longest axis the energy axis. However this axis is not parallel to the energy axis of the coordinate system. This is due to the fact that the resolution matrix M is not diagonal but has off diagonal elements which couple the momentum space with the energy. However this tilting of the resolution ellipsoid relative to the energy axis is rather independent of $\vec{K}$ and only slowly varying with the energy (as calculated with Rescal). So it seems to be appropriate by using the projection of the resolution ellipsoid onto the energy axis for the Gaussian energy distribution to account in first order to the neglected coupling between momentum space and energy. Thus using the momentum independent projection

of the resolution ellipsoid onto the energy axis (phonon width, 0.6meV in our case) leads to the good approximation:

$$I_{\omega_s}(\omega_0) \sim \int d\omega S(\omega + \omega_s)\ R(\omega + \omega_0), \tag{6.12}$$

where S is the one-dimensional Lorentzian energy distribution accounting for the finite life-time of our phonon mode and R the one dimensional Gaussian distribution accounting for the energy resolution of the triple axis spectrometer. In general the energy resolution depends on ω_0. This effect is 10 per cent around a mean value. If one considerers that the estimate of collimations (we didn't use collimators) is quite difficult and may lead to errors of 10 up to 20 per cent of the energy resolution it seems tolerable to use a mean value of the energy resolution for the Gaussian width in R. With $\omega' = \omega + \omega_0$ and $x = \omega_0 - \omega_s$ we get

$$I(x) = \int d\omega'\ R(\omega')\ S(x - \omega') \tag{6.13}$$

which is the definition of the Voigt function (Convolution of the Gaussian function with the Lorentzian function.) The Gaussian width is assumed to be given in units of FWHM and the Lorentzian width is assumed to be given in units of HWHW. All our constant $\vec{K}$-scans which are showed in the following are fit with such a Voigt (or two for the double peaks) function. The Gaussian width was assumed to be the calculated spectrometer resolution of 0.6 meV and the Lorentzian width was used as a refinable parameter. This refinement gives for any fit the intrinsic line width of the phonon (considering the damped harmonic oscillator as the decisive model). Moreover during these fits also the mean energy value of the phonon (zero point for ω_0) and its amplitude were treated as a refinable parameter. In addition a linear background was assumed for these fits leading to two more refinable parameters: the slope and a constant.

6.9.2 Three phonon peaks and a new superconductivity-induced effect

In this subsection the appearance of three phonon modes and a new superconductivity-induced effect which have already been mentioned will be summarized by giving meaningful and significant data in order to illustrate them. Figure 6.11 above shows the buckling mode (eigenvector see inset above) in the middle, the plane chain mode (at higher energies) and the (in-plane) apical oxygen mode (at lower energies, eigenvector see inset below) for $q_b = 0$ at $4K$. The plane chain mode is clearly resolved from the other two, which are also almost resolved with respect to each other, even if the apical oxygen mode forms a small shoulder on the buckling mode. Figure 6.11 below shows the Raman spectra for comparable energies at $10K$ for B_{3g} symmetry.

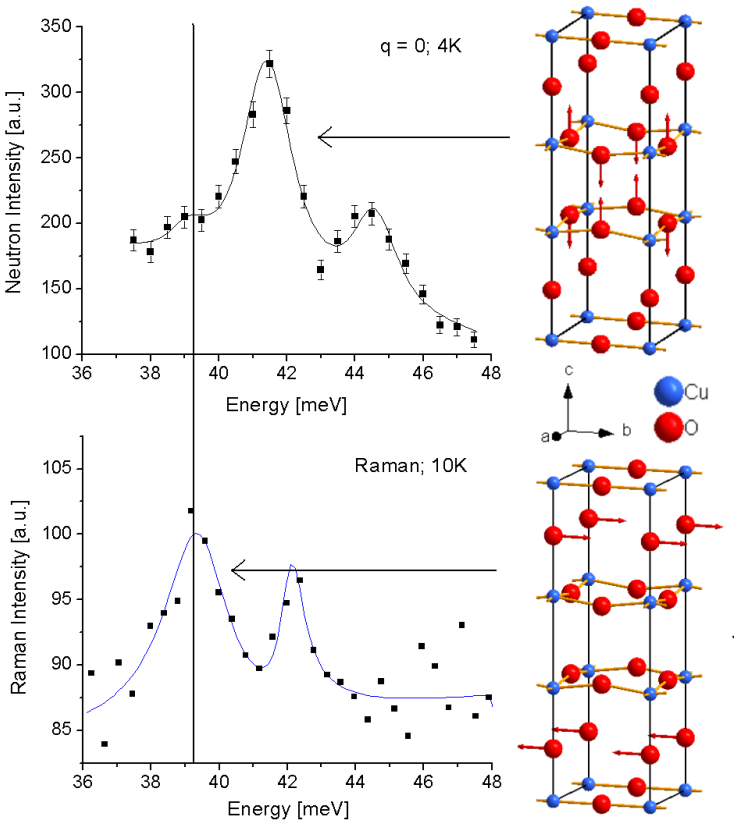

Figure 6.11: The figure above shows the three phonon peaks in an energy range where previous measurements only showed the buckling mode measured by inelastic neutron scattering. The buckling mode is in the middle, the plane chain mode at higher energies and the (in-plane) apical oxygen mode at lower energies for $q_b = 0$ at $4K$. Moreover it shows a refined fitting function consisting of three Voigt functions and a linear background. The figure below shows Raman data which identify the low energy peak as the in-plane apical oxygen mode with B_{3g} symmetry. This is indicated by the vertical line. Moreover in the inset at the right the eigenvectors of the buckling mode (above) and the in-plane apical oxygen mode (below) are shown.

The apical oxygen mode around $39meV$ can clearly be observed. The second smaller peak at higher energies polarization leakage of the buckling mode. The vertical line demonstrates that the third peak in 6.11 (above) is indeed the B_{3g} apical oxygen mode. The arrows relate the eigenvectors with the corresponding phonon peak in the raw data.

The new superconductivity-induced effect we could observe during our measurements is shown in figure 6.12. This figure compares the phonon buckling mode and the (in-plane) apical mode for temperatures below and above T_c. This figure shows

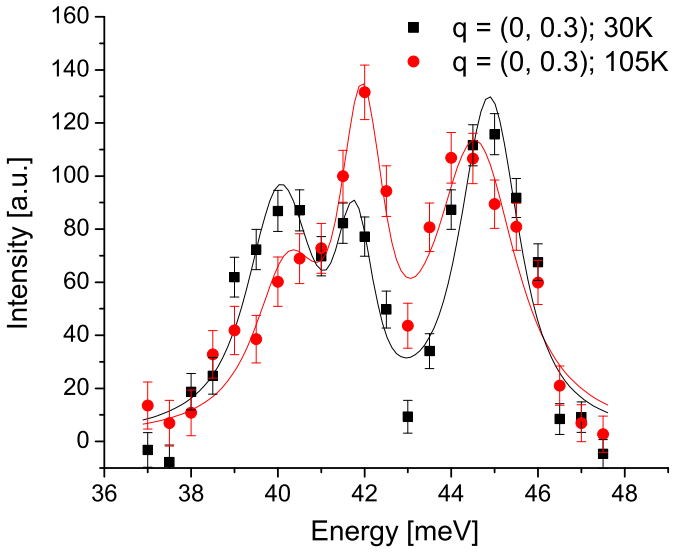

Figure 6.12: This figure shows the superconductivity-induced interaction of the buckling mode at $q_b = 0.3$ with the in-plane mode of the apical oxygen (superconductivity-induced transfer of spectral weight between both modes). Therefore both phonon modes are shown above (at $105K$) and below (at $30K$) the superconducting transition temperature. The black squares show the buckling mode well below the superconducting transition temperature. The red circles represent the buckling mode above the superconducting transition temperature. Moreover, in order to compare both graphs with each other directly we subtracted the background.

clearly the transfer of spectral weight between these two phonon modes due to the superconducting transition. Moreover this effect is anisotropic as nothing comparable can be observed along the a^* direction (see figure 6.13).
This anisotropic superconductivity-induced transfer of spectral weight between the buckling mode and the in-plane apical oxygen mode which can be clearly identified in figure 6.12 is a new and very interesting effect. These new measurements reported here are in contrast with previously measured data [103]. There it was claimed that the buckling mode broadens considerably due to superconductivity. However, these data have been obtained with a poorer spectrometer resolution and on twinned samples so that the broadening effect is not real but is simply a consequence of the mixing of different domains and phonon modes. Our data on untwined samples with a very good spectrometer resolution, however, show that the buckling mode even sharpens a little bit when cooling below T_c (see figure 6.20). In the next section (6.10) we will show by data on underdoped antiferromagnetic YBCO that

the buckling mode and the apical oxygen mode already hybridize without superconductivity. However, by comparing the data on underdoped and overdoped YBCO we can further conclude, that superconductivity strongly enhances this interaction between both modes.

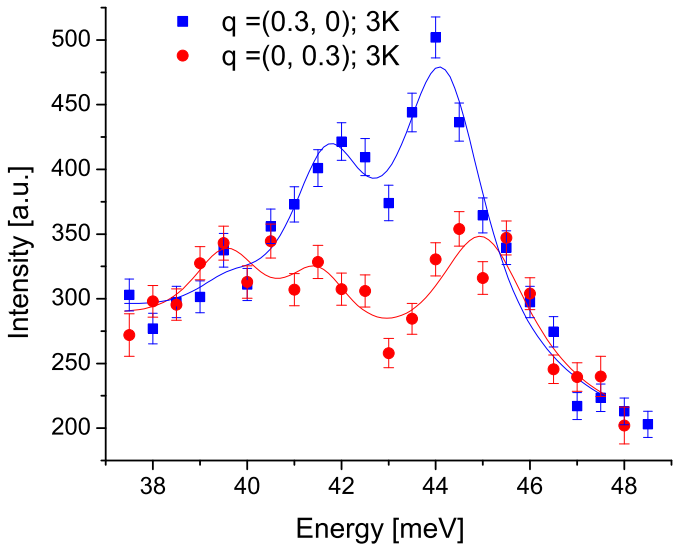

Figure 6.13: This figure presents the raw data of our phonon measurements of the buckling mode at $3K$ for both in-plane directions and the corresponding fitting functions. These graphs show impressively the anisotropy of the phonon buckling mode for $q = 0.3$ at $3K$.

Figure 6.13 compares the measurements of the buckling mode between both in-plane directions at $3K$. It clearly shows the remarkable intensity difference of the buckling phonon mode (peak in the middle of the figure). It is the first time that this anisotropy has been reported as earlier measurements of the buckling mode had been made with twinned samples [103]. The (in-plane) apical oxygen mode also shows anisotropic behavior: whereas it is very weak (actually zero) along the a^* direction, it shows an even higher amplitude than the buckling mode along the b^* direction. Actually there is no in-plane apical oxygen mode at energies just below the energy of the buckling mode for the a^* direction, however, it was possible to refine such a mode with a very small amplitude. This is due to the fact that the sample was not perfectly detwinned. The plane chain mode at energies above the energy of the buckling mode shows also a very pronounced anisotropy. Compared to the b^* direction this mode is softer and much stronger in intensity along the a^* direction. This is a rather temperature and phonon wave vector independent trend.

A comparison of the intensities of the plane chain mode for different in-plane directions and temperatures at $3K$ and $120K$ shows that the intensities along the b^* direction are much weaker than those along a^*. Only the center of the Brillouin zone is an exception. This can be understood by the fact that this phonon mode involves the chain oxygens and therefore shows a pronounced anisotropy.

As mentioned earlier the discovery that there exist three phonon modes (for

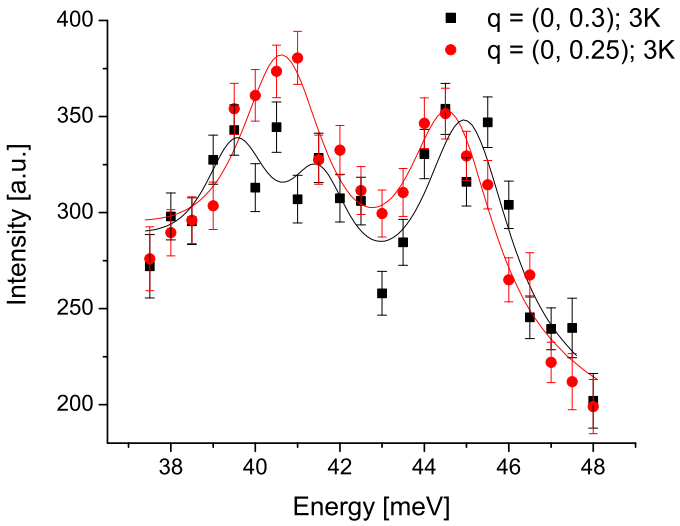

Figure 6.14: This figure presents the raw data of our phonon measurements of the buckling mode at $3K$ for the phonon wave vectors $q_b = 0.25$ and $q_b = 0.3$. We believe that the in-plane apical oxygen mode is superimposed to the buckling mode for $q = 0.25$ even if we cannot resolve both peaks for that phonon wave vector.

$q_b = 0.3$) in the energy range $37meV \leq E \leq 48meV$ which can be addressed by neutron scattering and not only the buckling mode is one of the main advances of this PhD thesis. And its validity has been remarkable shown by our temperature study especially by figure 6.12. Unfortunately the role of the apical oxygen mode along b^* is difficult to interpret for other points within the Brillouin zone. To discuss this issue figure 6.14 has been included within this PhD thesis. Figure 6.14 compares the raw data between the phonon wave vectors $q_b = 0.25$ and $q_b = 0.3$ at $3K$. The "buckling mode" at $q_b = 0.25$ has been fitted with a relatively broad line shape, whereas at $q_b = 0.3$ the fitting function consists of a double Voigt function, where the buckling mode is the mode at higher energies and a second, the in-plane apical oxygen mode appears. Therefore we believe that this broad peak also consists of the buckling mode and the apical oxygen mode which could not be resolved completely. This might be an interesting point for further investigations.

6.9.3 A further interesting effect

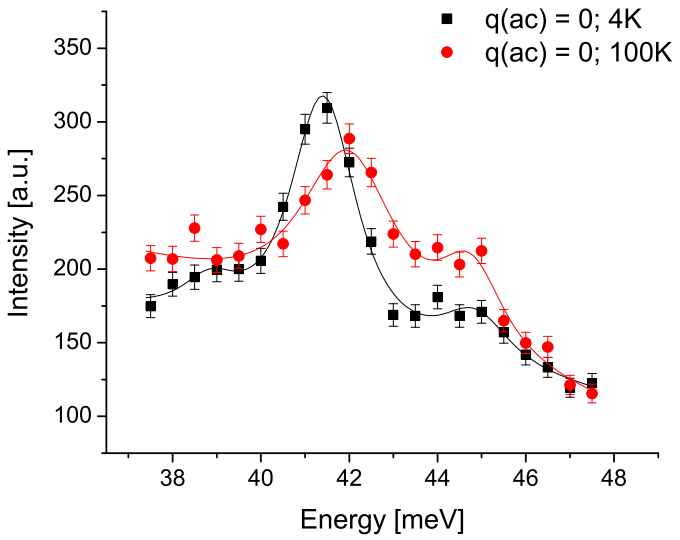

Figure 6.15: This figure shows the buckling mode at the center of the Brillouin zone (aligned in the a^*c^* plane) for different temperatures at $4K$ and $100K$. One observes a superconductivity phonon softening consistent with previous phonon measurements on that phonon mode [103]. Moreover these data reveal a very interesting effect: a superconductivity-induced transfer of spectral weight between the Raman active buckling mode and the plane chain mode.

After having discussed the new superconductivity-induced transfer of spectral weight between the buckling mode and the apical oxygen mode, now a similar effect concerning the plane chain mode at higher energies will be discussed. Figure 6.15 compares the buckling mode at the center of the Brillouin zone (aligned in the a^*c^* plane) at $4K$ and $100K$. With respect to the phonon line width this phonon behavior is usual, as the phonon broadens due to anharmonic effects for increasing temperature. And the phonon softening can be explained due to the superconducting transition [103]. However, these data show a further interesting superconductivity-induced effect concerning the plane chain mode. It can be observed that the plane chain mode exchanges spectral weight with the buckling mode when cooling below T_c. This is an interesting effect as both modes should not show this behavior as they have different symmetries, the buckling mode is Raman active whereas the plane chain mode is infra-red active.

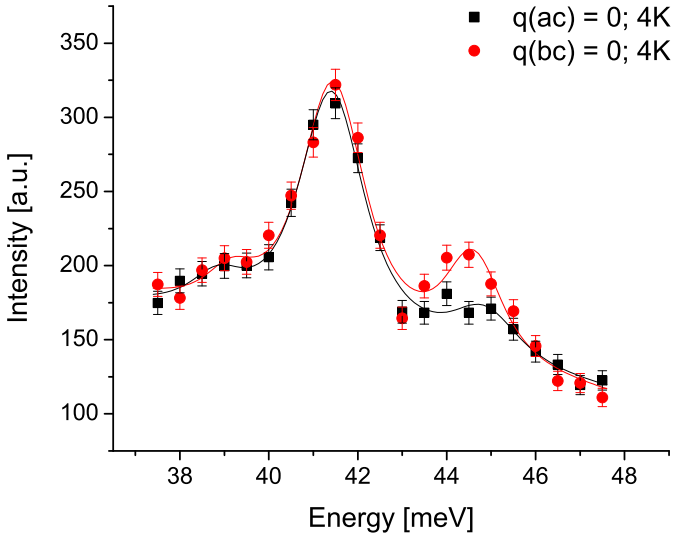

Figure 6.16: This figure shows all three phonon modes at $4K$ measured at the center of the Brillouin zone. The difference between both figures is the fact that the sample has been oriented within different scattering planes. For q_a it has been oriented in the a^*c^* plane and for q_b it has been oriented within the b^*c^* plane. Nevertheless both graphs show the phonon modes at the same point in reciprocal space. Therefore it is interesting that the plane chain mode has different intensities for both measurements. This can be understood by the fact, the oxygen chains are involved in that phonon mode. This is another hint, that we attributed the correct phonon eigenvector to this mode.

Besides this superconductivity-induced transfer of spectral weight between the buckling mode and the plane chain mode, this plane chain mode shows further interesting properties at the center of the Brillouin zone. Figure 6.16 shows the plane chain mode at the center of the Brillouin zone measured at $4K$. The black data were obtained by aligning the sample in the a^*c^* plane, whereas the red data were obtained when the sample was aligned within the b^*c^* plane. Even so for both measurements the phonon wave vector of the plane chain mode was $q = 0$ the intensity differs remarkably. These data means that this phonon mode has a eigenvector which is not symmetric in a and b. This is the case for the plane chain mode as it involves the oxygen ions of the chains. This effect means, that we have assigned the correct eigenvector for this phonon mode.

6.9.4 Energy dispersion of the buckling mode in $YBa_2Cu_3O_7$

In the previous subsection our measured data set was presented as raw data and appropriate fits with Voigt functions. In the following subsection the results of these fits namely the energy of the phonons and the intrinsic phonon temperature-dependent line width Γ of the interesting phonon at $q = 0.3$ will be shown. Figure 6.17 compares the energy dispersion of the phonon buckling mode measured along the a^* and b^* direction for different temperatures below the superconducting temperature at $3K$ and above T_c at $120K$. Moreover the energy of the apical oxygen mode is also shown for these phonon wave vectors where it was observable. First of all it should be mentioned that the dispersion is quite flat at $120K$. A comparison of the dispersion relations for both temperatures above and below T_c shows that the phonon mode softens considerably at the Brillouin zone center. The magnitude of the softening reduces for both in-plane directions towards the middle of the Brillouin zone. However, along the b^* direction this trend is superimposed with the interaction of the buckling phonon mode with the apical oxygen mode. Therefore this mode is also included in graphic. For $q = 0.3$ both phonon modes could be clearly resolved from each other. However, for $q = 0.25$ only one broad peak was observable instead of two peaks. Therefore the error bar of the buckling mode is quite big, as the energy is probably strongly affected by the interaction with the apical oxygen mode. Considering this effect the dispersion relations along both in-plane directions are more or less isotropic within the error bars.

6.9.5 Temperature study of the intensity of the buckling mode and the apical oxygen mode.

As described in the introduction the main (anisotropic) effect revealed by our measurements is the superconductivity-induced interchange of spectral weight between the buckling mode and the in-plane apical oxygen mode for q_b=0.3. In order to prove this effect a detailed temperature study of the intensities of both phonon modes has been made, which will be presented in this subsection. Figure 6.18 compares the intensities of the buckling mode and the in-plane apical mode at $q_b = 0.3$ for several temperatures. At room temperature the buckling mode has a relatively high intensity and is well pronounced, whereas the in-plane apical mode has a very low intensity and is hardly visible. For decreasing temperature the intensity of the buckling mode decreases considerably till $120K$, whereas the intensity of the in-plane apical oxygen phonon mode increases. However most of the effect takes place around T_c: the buckling mode looses considerably in intensity around T_c, whereas the intensity of the in-plane apical oxygen mode increases considerably. Whereas

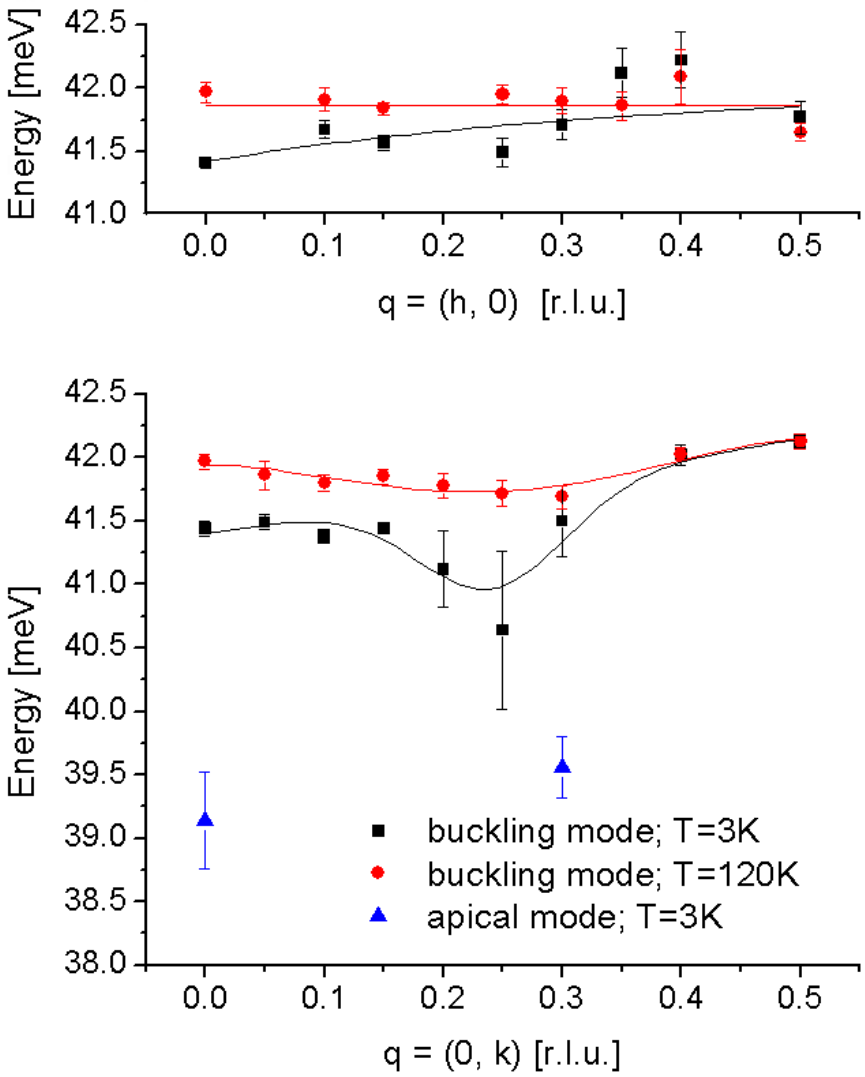

Figure 6.17: This figure shows the energy dispersion of the phonon buckling mode measured along the a^* (above) b^* (below) direction for different temperatures at $3K$, $120K$. Moreover at these wave vectors where the apical oxygen mode could be observed, in addition the energy values of this mode are shown for $3K$. Almost all the phonons within the Brillouin zone show superconductivity induced phonon softening when one cools below T_c. At $q_b = 0.25$ we couldn't resolve the buckling mode from the apical oxygen mode. That explains the big error bar within our figure. The lines are guides to eye.

above T_c the intensity of the phonon buckling mode is much higher compared to the intensity of the in-plane apical oxygen mode for $T < T_c$ the situation is inverse.

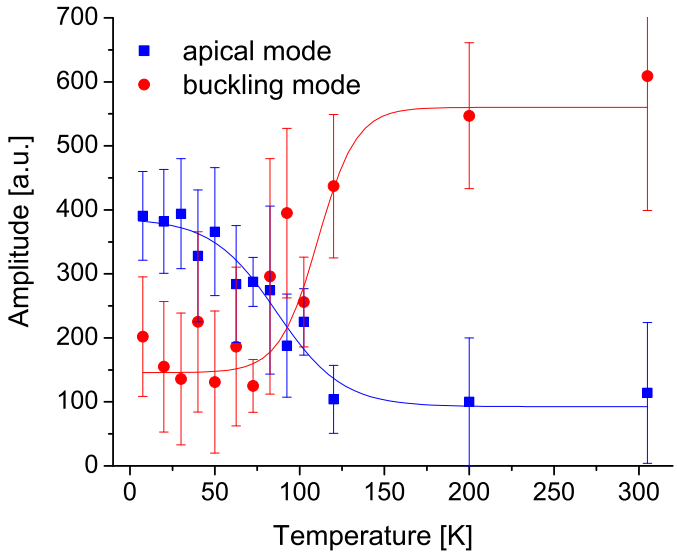

Figure 6.18: This figure shows a detailed temperature study from $5K$ up to $305K$ in different temperature steps measured at $q_b = 0.3$ for the intensities of both phonons the buckling mode and the in-plane apical oxygen mode. This figure gives the answers to several questions which can be posed concerning the anomalous effect described above for $q_b = 0.3$. It shows that it is a superconductivity-induced effect and it explains the anisotropy of the effect due to an interaction of the buckling mode with the neighboring apical oxygen mode. And this mode is only in close vicinity to the buckling mode along the b^* direction. This figure finally approves the anisotropic superconductivity-induced phonon effect described above. The lines are guides to the eye.

Here it has to be mentioned that the buckling mode and the in-plane apical oxygen mode are in close vicinity ($1.5meV - 2meV$ apart from each other). So figure 6.18 proves that there exists a superconductivity-induced exchange of spectral weight for these two phonon modes. That means especially that the phonon eigenvectors of both modes change during this process. This is an important and interesting fact which was not been reported in literature so far.
This transfer of spectral weight between the buckling mode and the in-plane apical oxygen mode should be connected with the energy difference ΔE of both phonon modes. This energy difference ΔE is shown in figure 6.19. On recognizes that the energy difference of both phonon modes first increases for decreasing temperature from $305K$ towards $120K$. However then for decreasing the temperature further both modes approach each other. Especially from T_c down till $50K$ both modes are

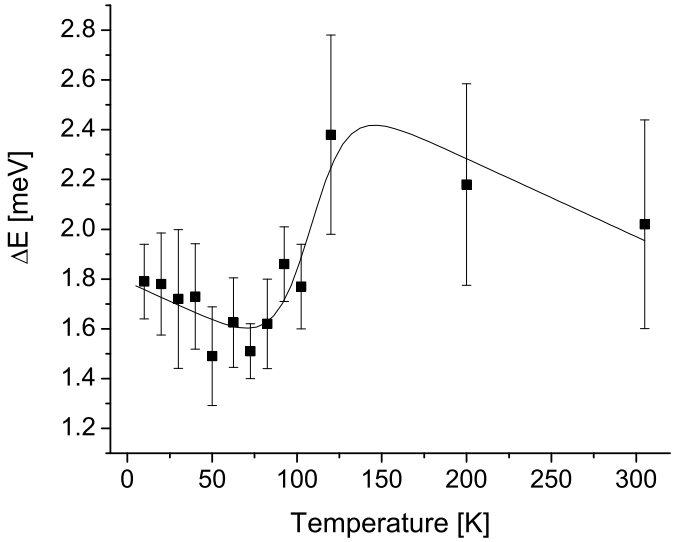

Figure 6.19: This figure shows the energy difference of the buckling mode and the in-plane apical oxygen mode at $q_b = 0.3$ for several temperatures. One observes that the both modes are especially below T_c in close vicinity. This is consistent with the picture that then both modes are interacting with each other. The line is a guide to the eye.

in very close vicinity. This confirms the fact that both modes interact strongly with each other.

Previous measurements on the buckling mode with twined samples revealed a line width broadening at around $q = 0.25$ [103]. However, due to the high resolution of the Puma spectrometer, we could resolve the buckling mode from its neighboring phonon modes and could hence determine the real line width. Figure 6.20 shows the line width of the buckling mode for different temperatures from above to below T_c. In contrast to the previous measurements mentioned above one observes that the line width reduces from 1.75 ± 0.5 above T_c till 0.75 ± 0.5 below T_c. Figures 6.19 and 6.20 show that the buckling mode softens and sharpens when cooling below T_c. This is due to an unusual electron-phonon coupling. As usually a phonon broadens due to a coupling to continuous electronic excitations. Instead such a unusual electron-phonon coupling could be explained due to a coupling to a collective mode. Such collective modes appear in high temperature superconductors below T_c. The most prominent examples are the "so-called" magnetic resonance mode [146] and Josephson plasmons [149].

In summary, the figures 6.12, 6.18, 6.19 and 6.20 describe a consistent story: figure 6.12 shows the transfer of spectral weight between the buckling mode and the apical

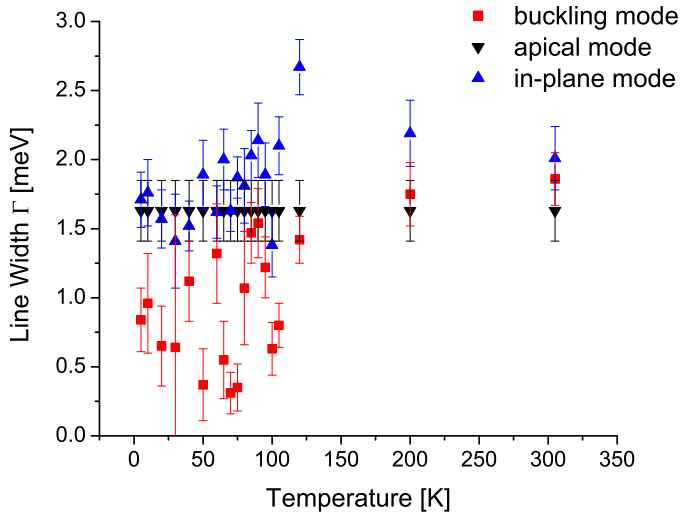

Figure 6.20: This figure shows the line width of the three phonon peaks: the buckling mode (red), the apical oxygen mode (black) and the plane chain mode (blue) measured at $q_b = 0.3$ for different temperatures. As the buckling mode and the apical oxygen mode can not be resolved completely, it was not possible to to refine both modes with all parameters being free. Instead the line width of the apical mode was assumed to be constant. This way the phonon line width of the buckling mode could be determined depending on the temperature.

oxygen mode. Together with figure 6.18 it shows that this effect is superconductivity-induced. Figure 6.19 shows, that due to the superconducting transition both phonon modes approach each other. As the buckling mode sharpens during this approaching 6.20 this phonon softening can be explained as unusual electron-phonon interaction, where the buckling mode interacts with a collective mode rather then the quasi-particle continuum of electronic states. This also explains the strong q-dependency and the anisotropy of the effect. Due to this superconductivity induced approaching (one forth of the initial distance) between the buckling mode and the apical oxygen mode the strong interaction of both modes can naturally be explained. The change of the intensity in neutron scattering is directly related to the eigenvector of the phonon via the dynamic structure factor. Therefore we can describe our effect finally as a superconductivity-induced change of the eigenvector of the buckling mode due to unusual electron-phonon interaction. This is a qualitatively and quantitatively new effect.

6.10 Measurements on $YBa_2Cu_3O_{6.1}$

In addition to the measurements on the superconducting samples of $YBa_2Cu_3O_{6.6}$ and $YBa_2Cu_3O_7$, we also made comparable measurements on an underdoped antiferromagnetic sample of $YBa_2Cu_3O_{6.1}$. This sample is not superconducting. The sample mass was around 25 grammes and the experiments were performed at 1T1 in Saclay. The experimental conditions were the same as for the 6.6-compound being described in section 6.11.2.
These measurements on this underdoped compound which are shown in figures 6.21 and 6.22 serve as a reference to the data which we obtained on the superconducting samples and which were described above. Both figures show that for the antiferro-

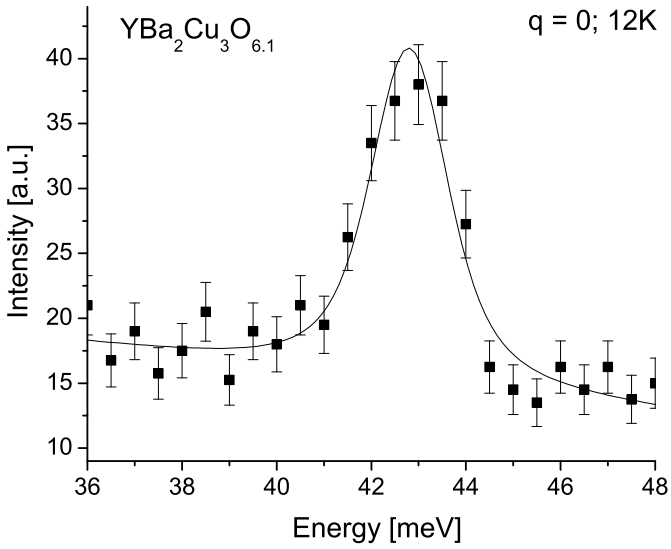

Figure 6.21: This figure shows the buckling mode at the Brillouin zone center measured at $12K$ for an underdoped sample. No plane chain mode at higher energies and no apical oxygen mode at lower energies can be observed.

magnetic compound no plane chain mode at higher energies is observable. This can be understood, as for this doping level no oxygen chains exist. Therefore only the buckling mode and the apical oxygen mode can be observed. Whereas the buckling mode can be observed for all q values, the apical oxygen mode is - similar to the situation in the overdoped compound - especially strong in the second half of the Brillouin zone. That means that the buckling mode and apical oxygen mode hybridize (mix) in the second half of the Brillouin zone due to an anti-crossing of both phonon modes. For the underdoped compound this is shown for $q = 0.4$ and at $12K$ in figure 6.22. The low temperature situation in the antiferromagnetic compound

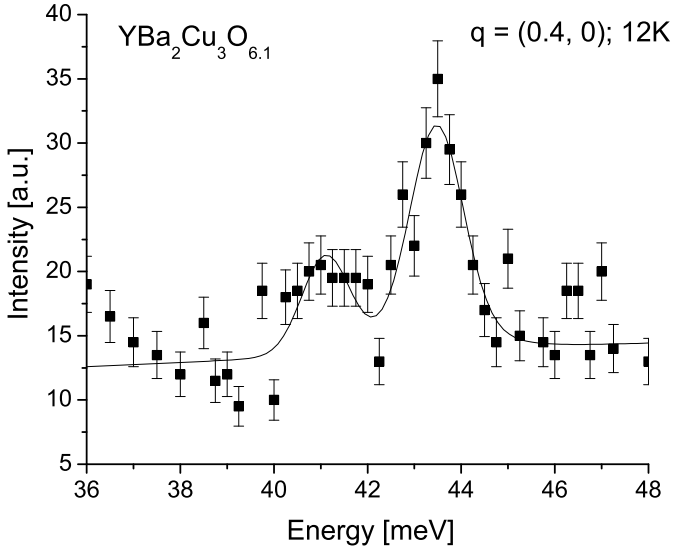

Figure 6.22: This figure shows the apical oxygen and the buckling mode at $q = 0.4$ measured at $12K$ for an underdoped sample. It indicates the coupling of the buckling and apical oxygen mode. Usually an in-plane mode (apical mode) should be very weak in the Brillouin zone where we measured. That means it already mixes with the buckling mode even without superconductivity. However, superconductivity enhances this effect strongly (see figure 6.12).

is therefore comparable to the high temperature (above T_c) data of the superconducting overdoped sample. That means that the buckling mode is much stronger in intensity compared to the apical oxygen mode. However, for the overdoped sample ($YBa_2Cu_3O_7$), at temperatures below T_c the buckling mode and the apical oxygen mode are comparable in intensity. That means that the hybridization of both modes in the superconducting sample is strongly enhanced by superconductivity. Thus our data on the antiferromagnetic sample also support that we discovered a new superconductivity-induced effect in the superconducting sample with doping level $x = 7$.

6.11 Measurements on $YBa_2Cu_3O_{6.6}$

The entire phonon measurements on $YBa_2Cu_3O_{6.6}$ has been performed at the thermal three axis spectrometer 1T1 at LLB. The reactor Orphée at LLB is a fission source amongst others for thermal neutrons. The spectrometer 1T1 is especially well suited for our experiments as it is optimized for inelastic phonon scattering and

one can obtain a very good energy resolution. This was especially necessary for our measurements as here we will report inelastic neutron scattering data of the phonon buckling mode in $YBa_2Cu_3O_{6.6}$. Our sample consists of small single crystals which has been annealed [64] in order to get the right oxygen content, afterwards they have been detwinned [147] so that we could perform anisotropic measurements and finally they have been oriented on a small aluminium plate. The total crystal mass of the whole sample was around 2.5 gramme. The space group of the orthorhombic $YBa_2Cu_3O_{6.6}$ is Pmmm and the unit cell parameters are $a \sim 3.83\mathring{A}, b \sim 3.88\mathring{A}$ and $c \sim 11.72\mathring{A}$. The good quality of the sample has been proven by earlier measurements [148].

6.11.1 Early measurements and spurion checks

Our (my) first triple axis measurements have been made without tests for spurious peaks. As pointed out in the previous chapter in inelastic neutron scattering spurious peaks can play a major role and falsify the intrinsic data considerably. Therefore later on we checked our spectrometer configurations for spurious peaks and indeed we had to conclude that our data might be contaminated by spurious peaks for most of the points in reciprocal space where we have measured. However at the boarder of the Brillouin zone our phonon measurements were not contaminated. Especially these measurements were quite interesting as they already showed the two peak structure of the phonon buckling mode along the b^* axis. Ironically it was this double peak structure which led us to the belief that spurion checks are necessary in order to exclude that the second peak is a spurious one. Later on we proved that this second peak is an in-plane mode of the in-plane oxygens in the CuO_2 double layer and that this mode is closely related to the phonon buckling mode. Therefore these early measurements will be shortly reported here: we measured the energy dispersion and the line width of the transverse out-of-phase phonon buckling mode of $YBa_2Cu_3O_{6.6}$ which is polarized in the c-direction. The sample was oriented successively by aligning the reciprocal lattice vectors a^*, c^* and b^*, c^* in the scattering plane (of the spectrometer) to investigate the anisotropy of that phonon mode. In order to maximize the structure factor the phonons were measured adjacent to the reciprocal lattice vectors $\vec{K}$ = (-1, 0, 10) and (0, -1, 10) for the a^* and b^* axis respectively, which are predominantly along the direction of the polarization. We measured this phonon at the center of the Brillouin zone ($q = 0, K_h = K_k = -1$) and moreover for different wave vectors q depending on the temperature and the scattering plane. As the phonons within the Brillouin zone except for the boarder ($q = 0.5, K_h = K_k = -0.5$) were contaminated by spurious peaks the complete data set won't be presented here. The measurements were made with fixed final energy ($8meV$). As monochromator the 220 reflection of an array of Cu crystals (Cu220) and as analyzer the 002 reflection of an array of graphite crystals (PG002) were

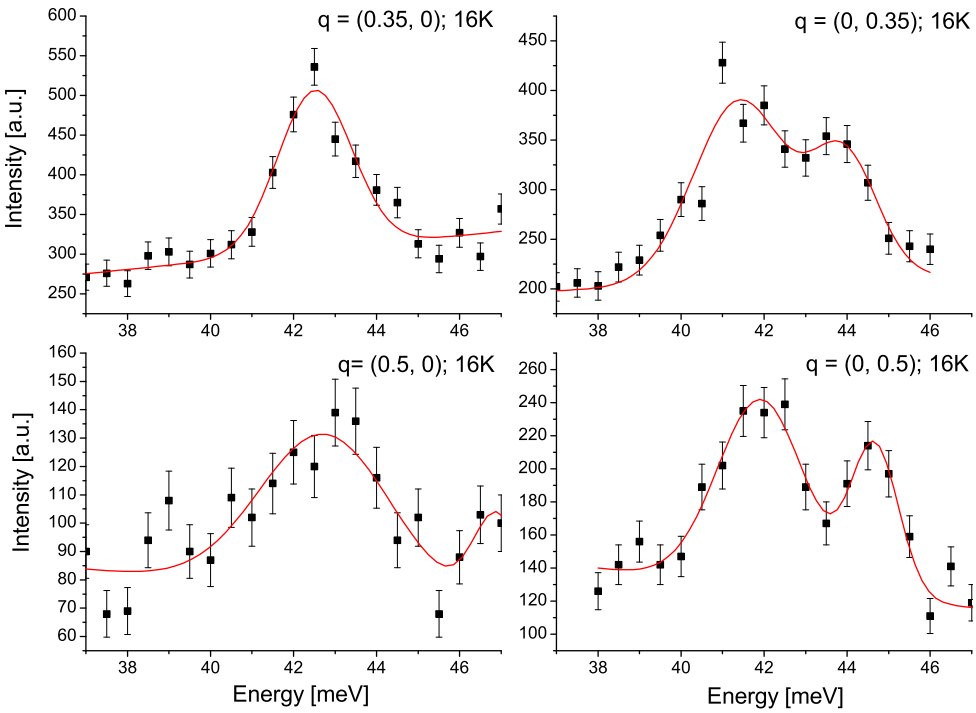

Figure 6.23: Early measurements of the phonon buckling mode in $YBa_2Cu_3O_{6.6}$ at $16K$ (below the superconducting transition temperature) for $q = 0.35$ and 0.5 along both in-plane directions a^* (on the left) and b^* (on the right). The red line is a Gaussian fit above a linear background to our measured data. The measurements at $q = 0.35$ might be contaminated by an intensive spurious peak, whereas for $q = 0.5$ the configuration was clean. Along the b^* axis there can be clearly observed two peaks, whereas along the a^* direction only one peak is visible. This second peak is no spurious peak but belongs to the phonon buckling mode. Therefore this mode is strongly anisotropic. Due to our fully detwinned sample we were able to measure anisotropic effects.

used. Both, the monochromator and the analyzer were horizontally and vertically focusing. We didn't use collimators. In order to suppress higher order contaminations we used two PG filters. For reaching temperatures down to $16K$ we used a displex. That the air around the sample couldn't freeze out and spurions due to the air could be prevented we used helium as an exchange gas as a local sample environment.

Figure 6.23 shows the phonon buckling mode in $YBa_2Cu_3O_{6.6}$ below the transition temperature for both in-plane directions a^* and b^*. A clear anisotropy can

be observed. Especially along the b^* direction two peaks could be observed. By our spurion test we showed that this second peak is no spurious peak, however the phonon with wave vector $q = 0.35$ might be contaminated by a spurious peak.
We found that all the phonons are contaminated by a spurious peak besides the phonon with wave vector $q = 0.5$. This result is valid for both in-plane directions a^* and b^*. Especially third order spurious peaks from the analyzer had been contaminating the data. Therefore we searched for equivalent positions in reciprocal space without spurious peaks and made for any of these positions a detailed spurion check. Meaning that we searched for higher order spurions from the analyzer and the monochromator. In order to test for the analyzer spurions we set the spectrometer to an elastic scattering condition and then fixed the monochromator θ and 2θ angle. Afterwards we checked all the configurations. In order to check for monochromator spurions we set the analyzer 2θ angle to 0 and fixed it. Afterwards we checked all the configurations again. We found clean positions adjacent to the reciprocal lattice vectors $\vec{K} = (1, 0, 10)$ and $(0, 1, 10)$. So all the measurements we will present in the following and which were presented in section 6.9 has been performed at points in reciprocal space without contamination. Details are given in the next subsection.

6.11.2 Introduction

In the following sections our energy dispersion and line width measurements of the transverse out-of-phase phonon buckling mode on $YBa_2Cu_3O_{6.6}$ (around $42.5meV$) for both in-plane directions a^* and b^* and different temperatures (above, below T_c and at room temperature) will be presented.
Notably we measured adjacent to the reciprocal lattice vector $\vec{K} = (1, 0, 10)$ and $(0, 1, 10)$ in order to maximize the dynamic structure factor. These points define centers of the Brillouin zones and with respect to these points the phonon wave vectors $q_a = 0.15, 0.25, 0.35$ along a^* and $q_b = 0.15, 0.25, 0.3, 0.35, 0.4$ along b^* were measured. Due to spurious peaks two exceptions were necessary: the boarder of the Brillouin zone $q = 0.5$ was measured at $\vec{K} = (-0.5, 0, 10)$ and $(0, -0.5, 10)$, and the center of it was measured at $\vec{K} = (1, 0, 9.9)$ and $(0, 1, 9.9)$ for the a^* and b^* direction, respectively. In addition the phonon with wave vector $q = 0.35$ was measured also at the points $\vec{K} = (0.65, 0, 11)$ and $(0, 0.65, 11)$. This was necessary as for the other configuration our phonon showed a very strong anomaly (see figures 6.24 and 6.25). We made our measurements above and below the superconducting transition temperature $T_c = 61K$ at $16K(12K)$ and $70K$, moreover for the b^* direction we also made room temperature measurements at $300K$.
Our scans were so-called $\vec{K}$-scans (meaning that the point in reciprocal space is kept constant, see chapter 5.3) with an energy varying around $42meV$. The final energy was fixed at $8meV$. As monochromator the 220 reflection of an array of Cu

crystals (Cu220) and as analyzer the 002 reflection of an array of graphite crystals (PG002) were used. By using that monochromator reflection we could obtain an energy resolution of about $1.2meV$. Moreover we used two graphite filters in order to reduce contamination from spurious peaks. Further spectrometer and environment conditions were equal to these reported for the early measurements in section 6.11.1. Moreover resolution calculations have been made and the important spectrometer parameters for these calculations are given in the next subsection. It should be stressed that our sample was fully detwinned this was especially important to measure the anisotropic effects described below. All our raw data have been fitted with a Voigt function above a linear background. This will be explained in some detail in a following subsection.
During the experiments described above we observed two interesting features of this phonon mode. First of all in general we observed a two peak structure for the phonons measured along the b^* direction, whereas along a^* only one peak could be observed. The two peak structures were fitted with a double Voigt function above a linear background. A good example for the double peak structure is the $q = 0.5$ phonon shown in figure 6.28. In order to investigate the two-peak structure observed along b^* further, we made l-scans $\vec{K} = (0, -0.5, l)$ for the energies where the two peaks appear: $44meV$ and $41.5meV$. Thus we could follow the l-dependence of the dynamic structure factor of these phonon modes. We observed for both energies the characteristic minimum of the structure factor for $l = 8$ and the increase between $l = 8$ and $l = 11$. Concerning these results the second peak should be related to the phonon buckling mode (often referred to be the main peak in the following). Later on we identified this second peak (smaller peak) as an c-axis polarized phonon mode of the oxygens in the CuO_2 double layer and the oxygen chains(see section 6.9). The second feature is quite interesting, as it concerns the line width of the phonon buckling mode (main peak with lower energy), which is a measure for the electron-phonon coupling. We observed a superconductivity induced "line width broadening" around wave vector $q_b = 0.35$ along the b^* direction (see figure 6.31) whereas "this broadening" couldn't be observed along the a^* direction (see figure 6.32). So this effect is strongly anisotropic. The phonon at $q_b = 0.35$ was measured at $\vec{K} = (0, 0.65, 11)$ as the corresponding phonon at $\vec{K} = (0, 0.65, 10)$ showed a strong anomaly. This is the most interesting feature of our measurements and is shown in figures 6.24 till 6.27. The strong damping of the $q_b = 0.35$ phonon leads to the assumption that the phonon line width is extraordinary big for that particular phonon. This coincides with the observation shown in figure 6.31 that the line width is maximal at around $q_b = 0.3$ till 0.35. However, for $YBa_2Cu_3O_7$ we observed around that wave vector a third phonon mode in the vicinity of the buckling mode. Hence we are convinced, that this broad feature is reality a superposition of this phonon mode with the buckling mode. It turned out (see below in the section for

the measurements on $YBa_2Cu_3O_7$) that this phonon anomaly can be explained by a superconductivity induced interaction of the buckling mode with this third phonon mode, which involves the oscillation of the apical oxygen. Therefore this phonon anomaly is consistent with the picture we developed in order to explain our data on $YBa_2Cu_3O_7$. Concerning our raw data, it was correct to fit the data with two peaks along b^* and with one peak along the a^* direction. Moreover we want to state that we carefully checked for spurious peaks and that we therefore believe that we measured real effects.

Resolution of 1T1 calculated with Rescal

For all the points in reciprocal space for which measurements have been made also the triple axis resolution function have been calculated using the computer program Rescal. Anyway it should be stressed that the resolution was independent of the point in reciprocal space $\vec{K}$ where we made our measurements within an accuracy of two digits. That means the resolution for all our measurements was $1.2meV$. This is the value one obtains if one projects the resolution ellipsoid (see chapter 5.5) in four dimensional energy-momentum space onto the energy axis. Now the specific parameters of the triple axis spectrometer 1T1 at Saclay, which has been necessary as an input to Rescal for calculating the resolution, shall be presented. We calculated the resolution with Rescal according to the method of Popovici, that means it was especially essential to know the dimensions of the neutron source, the monochromator, the sample and the analyzer. First of all we inserted the monochromator and analyzer d-spacing $d_{mono} = 1.278\mathring{A}, d_{anal} = 3.354\mathring{A}$, which can be calculated knowing the lattice constants and the Bragg reflection. See also [2], p. 61. Next the mosaicities of the monochromator, the analyzer and the sample were required. For the monochromator and the analyzer the mosaicity is 36 minutes and for the sample 90 minutes. The scattering sense of the spectrometer was for all our measurements a W configuration, meaning that it was 1 for the monochromator, -1 for the sample and 1 for the analyzer. We measured with fixed final energy which corresponds to a final scattering vector $\vec{k}$ of $1.96\mathring{A}^{-1}$. Moreover the horizontal and vertical collimations for the distances source to monochromator, monochromator to sample, sample to analyzer and analyzer to detector were required. All the horizontal collimations were two degrees. The vertical collimation for the first two distances were 110 minutes and for the last two distances 100 minutes. Moreover the program needs the information of the lattice constants, the scattering plane and the initial and final point of the scan (in four dimensional energy-momentum space). For Popovici's method the following parameters were necessary in addition to these one already mentioned. First we had to specify that we have a rectangular source with a width of 4 cm and a height of 7 cm. We used guides with horizontal divergence of 60 minutes and vertical divergence of 120 minutes. Moreover we used a flat-plate sample

with dimensions $0.2 \times 2 \times 2\ cm^3$ and a rectangular detector with a width of 1.5 cm and a height of 10 cm. The dimensions of the monochromator are $0.2 \times 36 \times 70\ cm^3$ and the analyzer are $0.2 \times 24 \times 90\ cm^3$. The distances LO (source to monochromator), L1 (monochromator to sample), L2 (sample to analyzer) and L3 (analyzer to detector) were $387, 180, 90$ and 90 cm. The horizontal and vertical focussing of the monochromator were 0.27 $1/m$ and 0.01 $1/m$, respectively, and for the analyzer the horizontal and vertical focussing were 0.42 $1/m$ and 0.01 $1/m$, respectively.

Fitting function for our constant $\vec{Q}$-scans: Voigt functions

In analogy to our measurements for $YBa_2Cu_3O_{7.0}$ all our measured data on $YBa_2Cu_3O_{6.6}$ which will be presented in the next sections have also been fitted with Voigt functions. The Gaussian width is again assumed to be given in units of FWHM and the Lorentzian width in units of HWHW. All our constant $\vec{K}$-scans which are showed in the following are fit with such a Voigt (or two for the double peak) function. The Gaussian width was assumed to be the calculated spectrometer resolution of 1.2 meV and the Lorentzian width was used as a refinable parameter. This refinement gives for any fit the intrinsic line width of the phonon (considering the damped harmonic oscillator as the decisive model). Moreover during these fits also the mean energy value of the phonon (zero point for ω_0) and its amplitude were treated as a refinable parameter. In addition a linear background was assumed for these fits leading to two more refinable parameters: the slope and a constant. In the following the most interesting features of the buckling mode, the anomaly at $q = 0.35$ and the anisotropy of the in-plane oxygen mode will be presented.

6.11.3 The phonon anomaly at $q_b = 0.35$

The intensity anomaly at $q = (0, 0.35) = q_b = 0.35$ at $16K$ is the most amazing feature of our data on the buckling mode. The phonon at this specific wave vector

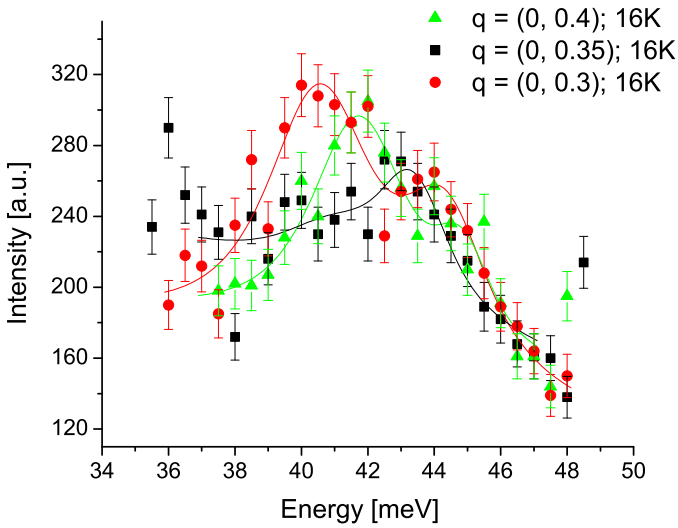

Figure 6.24: This figure shows the buckling phonon mode along the b^* axis for wave vectors $q = 0.3, 0.35, 0.4$ at $16K$ measured with $K_c = 10$. This graph clearly shows the intensity anomaly at $q = 0.35$. That means the buckling mode doesn't have intensity.

seems to be extremely broad. However it is probable that this "broadening" is due to a second (third) phonon mode the Raman active B_{3g} apical oxygen mode. As this would be consistent with the effect which we found for comparable experimental conditions in $YBa_2Cu_3O_7$. It seems furthermore to be interesting, as this intensity anomaly is very different depending on l. For $l = 10$ the buckling phonon mode vanishes almost which is again consistent with our data on $YBa_2Cu_3O_7$, whereas it can be clearly observed for $l = 11$.
Figure 6.24 shows the buckling phonon mode along the b^* axis for wave vectors $q = 0.3, 0.35, 0.4$ at $16K$ measured with $K_c = 10$. For higher energies a second mode an in-plane mode of the copper oxygens can be observed. As mentioned earlier these phonons have been fitted according to the Levenberg-Marquardt-gradient method with Voigt (double Voigt) functions. The fits of the two phonons show that the main peak almost vanishes for $q = 0.35$ whereas for neighboring wave vectors this buckling mode can be clearly seen. For $q = 0.3$ one can clearly distinguish two peaks the buckling mode at $40.6meV$ and the plain-chain mode at $44.3meV$. For $q = 0.4$ one observes a clear peak at $41.8meV$ with a pronounced shoulder at

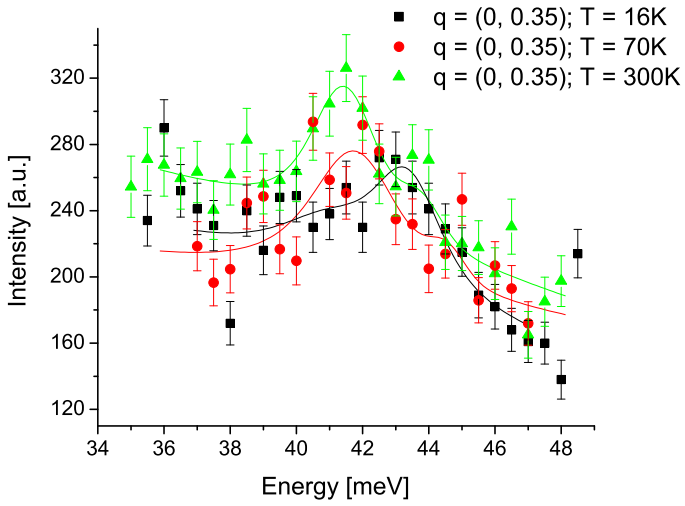

Figure 6.25: This figure shows the phonon buckling mode for $q = 0.35$ at different temperatures. Above T_c at $70K$ and $300K$ one observes a clear peak (the buckling mode) at around $41.5meV$, whereas at $16K$ no peak can be seen. Only for higher energies a smaller peak is visible. See also text.

$44.9meV$. One would expect for the phonon with wave vector $q = 0.35$ for the main peak an energy around $41meV$. However at that energy value the intensity is rather small. One observes a peak around $43meV$ which is probably s superposition of a very weak buckling mode and the plain chain mode. That means the intensity of the buckling mode changes dramatically when changing the wave vector from $q = 0.3$ to $q = 0.4$. As mentioned earlier that anomaly can only be observed along the b^* direction and it can be explained in a natural way by assuming that there exists a third phonon at an energy below but close to that of the buckling mode which interchanges spectral weight at T_c with the buckling mode. So that intensity anomaly for the $YBa_2Cu_3O_{6.6}$ sample is consistent with the observations from $YBa_2Cu_3O_7$. Figure 6.25 shows the buckling mode for wave vector $q = 0.35$ for different temperatures at $16K$ (black), $70K$ (red) and $300K$ (green). Again one recognizes the anomaly for that phonon. For temperatures above the superconducting transition temperature this phonon is well defined and one recognizes a peak at around $41.5meV$. Moreover these peaks possess a shoulder at high energy values. These shoulders indicate the second peak (plane chain mode), which is only present along the b^* direction. At $16K$, however, one cannot recognize a peak at that position. In summary this figure again demonstrates the intensity anomaly of the buckling mode at $q = 0.35$.

Figure 6.26 shows the phonon mode for wave vector 0.35 at different temperatures

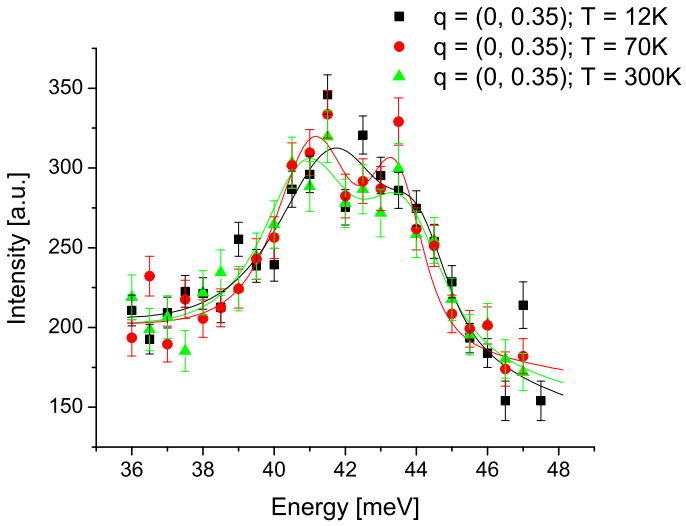

Figure 6.26: This figure shows the phonon buckling mode for phonon wave vector 0.35. This time it has been measured for $K_c = 11$. It is really interesting that the intensity anomaly of the buckling mode cannot be observed for that reciprocal lattice vector. However, these measurements strengthen the fact, that the buckling mode seems to be quite broad. This effect can again be attributed to the fact, that there exists a third phonon mode at an energy below and close to the buckling mode.

($12K$ (black), $70K$ (red) and $300K$ (green)). But this time we measured adjacent to the reciprocal lattice point $\vec{K} = (0, 0.65, 11)$. There the dynamic structure factor is also relatively high. For $K_c = 11$ there appeared a strong buckling mode and the in-plane mode which could be fit very well with two Voigt functions. This is shown in figure 6.26. One clearly recognizes that the buckling mode is much broader at $12K$ than at $70K$ or at $300K$. This effect is superconductivity induced and is probably due to an enhancement of the intensity of a third phonon mode (apical oxygen in-plane oscillation) which is for the b*-direction below but close to the buckling mode.

The anisotropy behavior of the intensity anomaly of the buckling mode is one of the most interesting features we could observe. The observation of this anisotropy was only possible due to our fully detwinned sample. Along the b^* direction this mode seems to be broadened due to an intensity increase of the nearby apical oxygen mode for temperatures below T_c. This is in contrast to the a^* direction where no superconductivity induced "broadening" can be observed. This is shown in figure 6.27. This figure shows the phonon mode for $q = 0.35$ measured along a^* at $16K$ and $70K$. Clearly one observes that the peak for lower temperature is sharper than

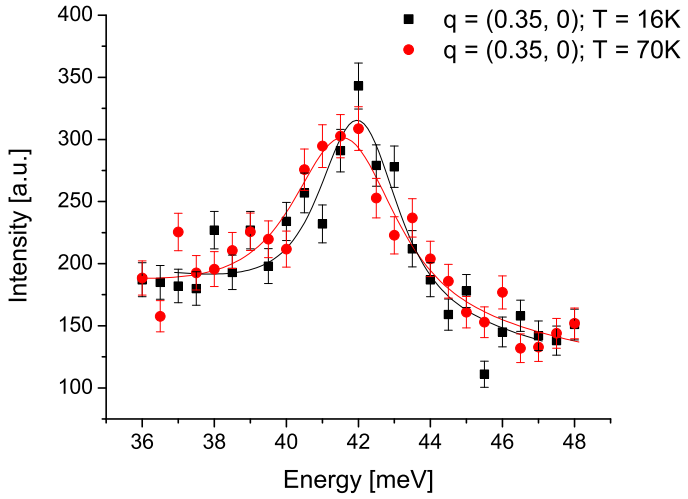

Figure 6.27: This figure shows the buckling mode again for $q = 0.35$ but this time measured along the a^* axis at $16K$ and $70K$. Here we clearly observe that this mode at $16K$ is sharper compared to the phonon measured at $70K$. This is the reason why we claim that the phonon anomaly at $q = 0.35$ is anisotropic. This fact can easily be interpreted by the explanation of this effect by a third phonon mode (in-plane mode of the apical oxygens) as along the a^*-direction this mode is not in contrast to the b^*-direction in close vicinity to the buckling mode. Moreover, the anisotropy is not only reflected by that anomaly but also by the fact, that along the a^* direction no plane chain mode can be observed.

this one for higher temperature. This is the normal behavior expected due to anharmonic effects. Therefore the phonon anomaly described above can only be observed along b^*. Moreover, along a^* no plain chain mode at higher energies can be observed. This can be explained ba the fact that this modes involves the chain oxygens, which are situated along the b direction. This naturally explains the disappearance of this phonon mode along the a^* direction.

6.11.4 Anisotropy between the a^* and b^* axis of the phonon buckling mode: two peak structure along the b axis

In the last subsection we showed and described the anomaly at $q = 0.35$ and its remarkable anisotropy. However, there appears another interesting anisotropy: concerning the plain chain mode for energies above that of the buckling mode. This phonon mode can only be observed along the b^*-direction. This anisotropy will be showed in the following subsection.

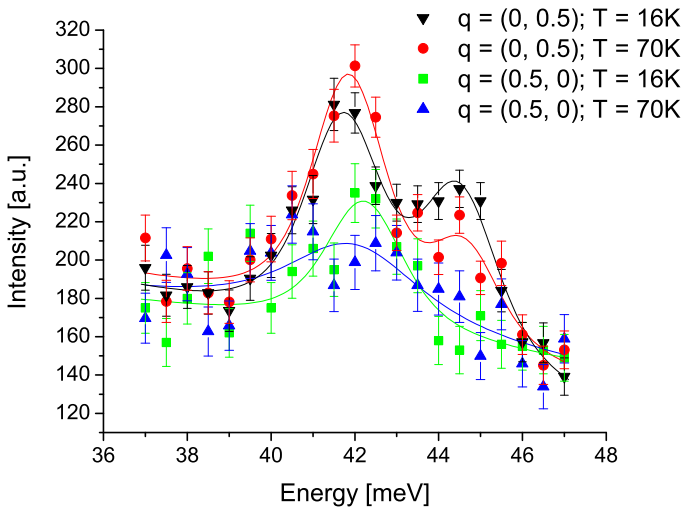

Figure 6.28: This figure shows the phonon buckling mode at $q = 0.5$ for the b^* direction at $16K$ (black) and at $70K$ (red). Moreover it shows also the measurements along a^* at $16K$ (green) and at $70K$ (blue). Along the a^* direction the plain chain mode at around $44.5meV$ cannot be observed, whereas along b^* it is definitely there. This is an remarkable anisotropy of the phonon spectra at this doping level.

Figure 6.28 shows the phonon buckling mode and the plain chain mode at $q = 0.5$ for both scattering directions and at temperatures below and above T_c. The phonons at $16K$ are shown in black and green and are measured along b^* and a^*, respectively. The phonons at $70K$ are shown in red and blue and are measured along b^* and a^*, respectively. First of all a remarkable anisotropy can be observed: along the b^* direction the plain chain mode at around $44.5meV$ is clearly visible, whereas along a^* it does not appear. Moreover, the plane chain mode becomes smaller for increasing temperature, whereas the main peak becomes stronger in intensity. This behavior can not be observed for all the other phonons in the Brillouin zone measured along the b^* direction and is a hint for a superconductivity-induce interaction of both phonon modes. The phonons measured along the a^* axis are much weaker in intensity compared to these one measured along b^*. Moreover these phonons show a normal temperature behavior as the phonon broadens when the temperature is increased. Along the b^* axis the plane chain mode is observed and the buckling mode shows an almost equal line width at $16K$ and $70K$.

Figure 6.29 shows the very strong anisotropy of the $q = 0.35$ phonon at $16K$. This anisotropy is really amazing. Whereas along the a^* direction only the buckling mode can be observed, along b^* direction we observe the buckling phonon mode in the middle, the plane chain mode of the layer and chain oxygens at higher energies

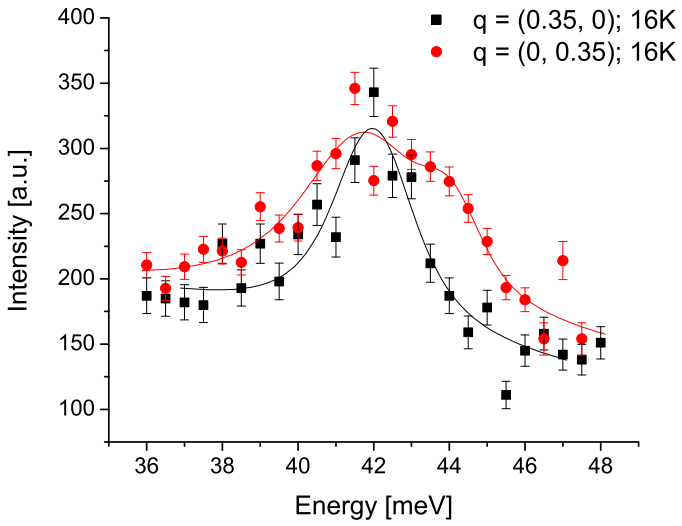

Figure 6.29: This figure shows the phonon buckling mode at $q_b = 0.35$ for both scattering directions at $16K$. This picture shows the anisotropic phonon anomaly of the phonon buckling mode very nice. On the one hand one observes a single sharp phonon peak along the a^* direction as one expects it for one phonon. On the other hand there are at least two phonon modes along the b^* direction: the buckling mode and the plane chain mode (at $44.5meV$) of the layer and chain oxygens which appears only along the b^*-direction. Moreover we believe that there is even a third phonon the apical oxygen mode for lower energies which can not be resolved from the buckling mode.

and probably the in-plane apical oxygen mode at lower energies. Here one can imagine how important it was to measure with a detwinned sample in order to observe this anisotropy.

Figure 6.30 shows the phonon mode for wave vector $q = 0.25$ for both scattering directions at $16K$. It shows two relatively sharp phonons as expected for low temperatures. It is interesting that the plane chain mode appears only along the b^* direction. That means it is independent from the phonon anomaly described above and is a second very interesting feature, which is also strongly anisotropic.

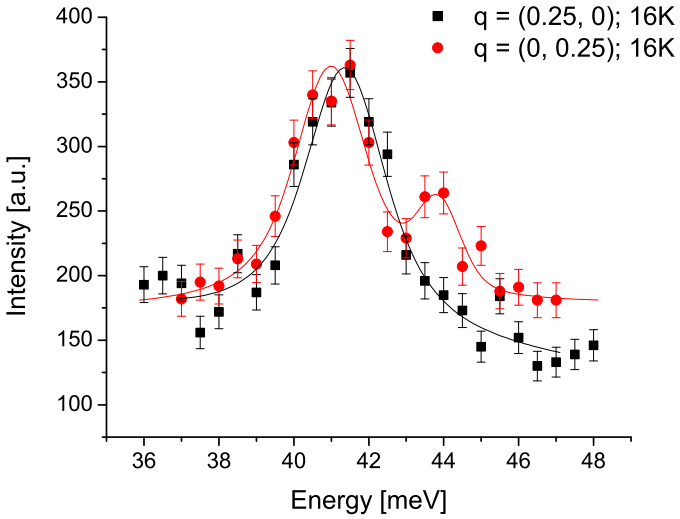

Figure 6.30: This figure shows the phonon mode for $q = 0.25$ at $16K$. It compares the phonons for both scattering directions. The main peaks are equal in intensity and are quite sharp. However, along the b^* direction a second peak at higher energies the plane chain mode of the layer and chain oxygens can be observed. This reflects again the fact, that this second phonon mode is only observable along the b^* direction.

6.11.5 Line width and energy dispersion of the phonon buckling mode in $YBa_2Cu_3O_{6.6}$

After having described the intensity phonon anomaly of the buckling mode and the anisotropy of the plane chain mode, we want to present the results of the refinement procedures, where all phonon peaks were fitted with Voigt functions. First we will present the anisotropic line width of the buckling mode and afterwards the also anisotropic dispersion relation. The error bars are given as they were calculated by the fitting program Mfit (for Matlab) distributed online by the ILL. Although we believe that there exist three phonon modes (the buckling mode, the plane chain mode and the in-plane apical oxygen mode), we could only observe the two main phonon peaks (the buckling mode and the plane chain mode). Therefore a possible increase in intensity of the apical oxygen mode at $q = 0.35$ along b^* could only be observed by a "broadening" of the buckling mode. Along the a^* direction, for most of the phonon wave vectors the buckling mode shows the usual phonon behavior, that means it broadens when increasing the temperature. However for the phonon wave vector $q = 0.15$ a clear broadening for cooling down below T_c can be observed.

Figure 6.31 shows the phonon line width of our phonon mode measured along the b^* direction for different temperatures. Below T_c at $16K$ (black), above T_c at

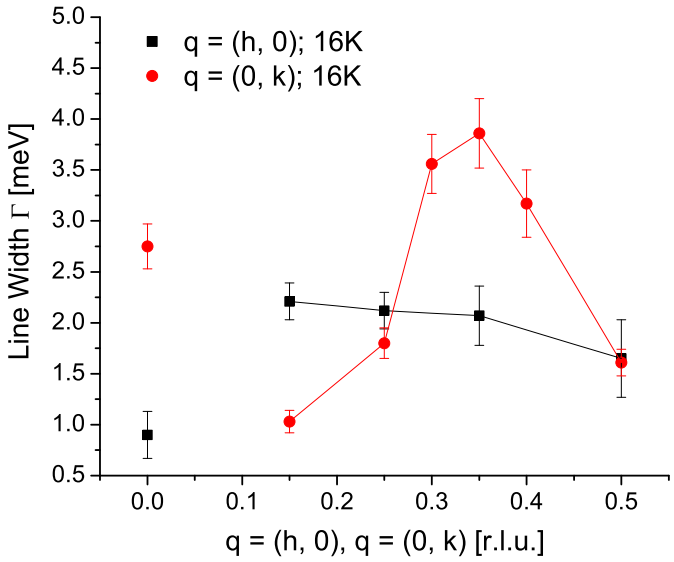

Figure 6.31: This figure shows the phonon line width Γ of the phonon buckling mode measured along the b^* direction and it compares the temperature below T_c ($16K$, black), above T_c ($70K$, red) and at room temperature ($300K$, green) with each other. A clear phonon anomaly can be observed for these measurements along b^*. This is being indicated in the figure by a connection between the points of the same temperature. This clearly shows that the line width at $16K$ is bigger than the line width at $70K$ within most of the whole Brillouin zone. This effect can be understood by a superconductivity-induced exchange of spectral weight between the buckling mode and the in-plane apical oxygen mode. See text below and corresponding data for $YBa_2Cu_3O_7$ (figure 6.12).

$70K$ (red) and at room temperature at $300K$ (green). Here we observed a real phonon anomaly at around phonon wave vector $q = 0.35$, which can be explained by a superconductivity-induced interaction of the buckling mode with the in-plane apical oxygen mode. Due to that coupling the latter mode increases in intensity and constitutes together with the buckling mode a broad feature. In order to observe this anomaly more clearly we measured for $16K$ in addition to the standard wave vectors the phonon line width also at $q = 0.3$ and $q = 0.4$. These measurements affirm the anomaly. This is a completely different story compared to the effect along a^* where only one phonon mode could be observed. The phonons at the center of the Brillouin zone show for both temperature very high phonon line widths. This might be due to the coupling of the buckling mode to the oxygen chains which is much stronger along the b^* direction compared to the a^* direction (we want to re-

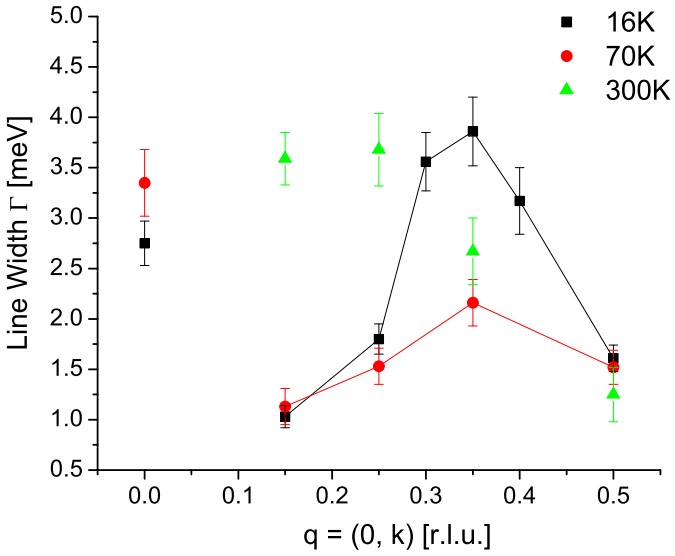

Figure 6.32: This figure shows the phonon line width Γ of our phonon mode measured at $16K$ and it compares the different scattering directions a^*(black) and b^*(red) with each other. Connecting lines between points of the same scattering direction show the pronounced anomaly: the "broadening" of the buckling mode can only be observed along b^* and is hence strongly anisotropic. Together with figure 6.31 we can state that we have a superconductivity induced strongly anisotropic phonon anomaly around wave vector $q = 0.35$. This anisotropy can be understood by the fact, that the in-plane apical oxygen mode is only in close vicinity to the buckling mode along the b^* direction.

mind that we measured this phonon at $K_c = 9.9$ instead of $K_c = 10$). Along a^* this phonon has a line width of around $1meV$ for $16K$ and $1.75meV$ for $70K$, these values seem to be more appropriate and will fit nicely in the whole picture. Last but not least it shall be discussed the line width for $300K$. Here the line widths of the phonon with $q = 0.5$ is remarkable. As it is comparable in line width with the much lower temperatures at $70K$ and $10K$. This is also not explainable easily. However the very broad line width for smaller wave vectors are again well understood.
Figure 6.32 compares the line width of the phonon buckling mode for different in-plane directions a^*(black) and b^*(red) at $16K$. It demonstrates again the phonon anomaly which can be observed along the b^* direction. Along this direction a pronounced "broadening" can be observed, whereas the phonon line width remains almost constant along the a^* direction. To stress this effect points for different phonon wave vectors and the same scattering directions are connected with straight

lines in figure 6.32. The most important fact about this anomaly is that it is superconductivity-induced, meaning it can only be observed at $16K$ and not at $70K$, and maybe more interesting it is only observed along the b^* direction and not along a^*, meaning that it is a strongly anisotropic effect. This "broadening effect" can be understood by the superconductivity-induced intensity increase of the in-plane apical oxygen mode, which is along the b^* direction in close vicinity to the buckling mode. Most probably this phonon mode could not be resolved from the buckling mode. After having shown the interesting anomaly in the phonon line

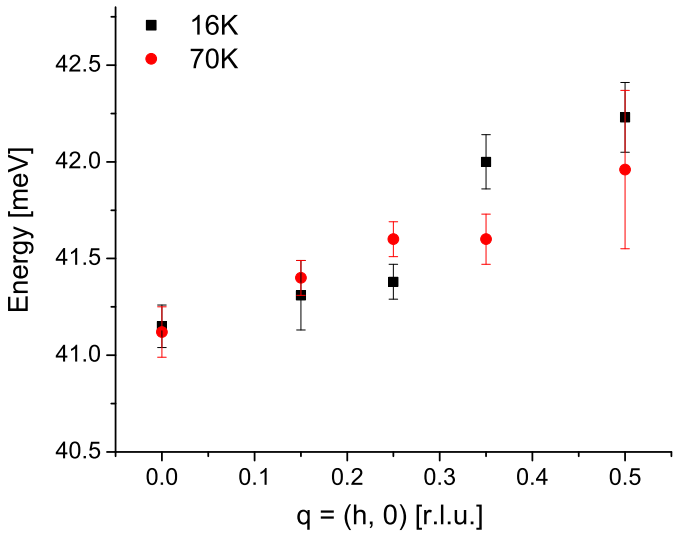

Figure 6.33: This figure shows the dispersion of the phonon buckling mode for measurements along the a^* axis for different temperatures: at $16K$ (black) and at $70K$ (red). The main tendency of the q-dependency is that the energy increases towards the boarder of the Brillouin zone for both temperatures. Therefore the dispersion seems to be rather temperature independent between $16K$ and $70K$.

width of the buckling mode in $YBa_2Cu_3O_{6.6}$ which is probably related to the apical oxygen mode, it is also worth looking at the energy dispersion.
Figure 6.33 shows the energy dispersion of the phonon buckling mode along the a^* direction and compares the temperature at $16K$ (black) with the temperature at $70K$ (red). It can be recognized that the phonon hardens from the center of the Brillouin zone towards its boarder. This effect seems to be rather independent from the temperature as it can be observed for both temperatures above and below T_c.

Figure 6.34 presents the energy dispersion of the phonon buckling mode which was obtained by measuring the mode along the b^* direction. The graph shows the measurements for the whole Brillouin zone at temperatures $16K$, $70K$ and $300K$.

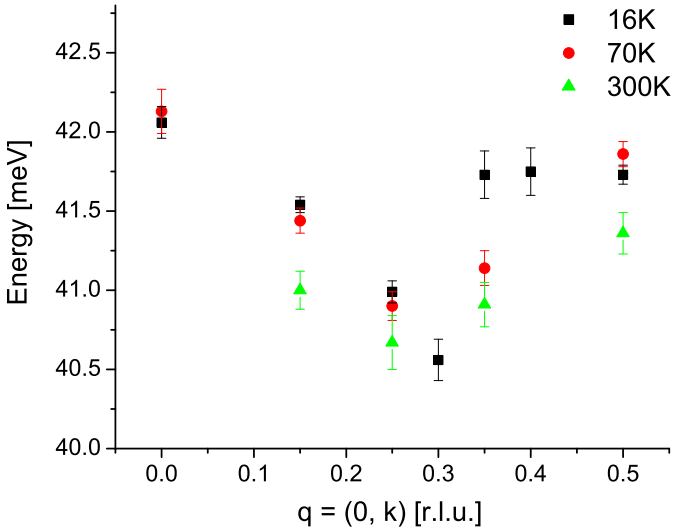

Figure 6.34: This figure shows the dispersion of the phonon buckling mode for measurements along the b^* axis for different temperatures: at $16K$ (black), $70K$ (red) and at $300K$ (green). The energy for this phonon along b^* is almost the same as along a^* for the boarder of the Brillouin zone. And for decreasing wave vector the phonon also begins to soften, however at around $q = 0.3$ the phonon hardens again considerably. This can only be observed along b^*. Except for $q = 0.35$ there can no temperature dependency be observed. See text for a further discussion.

however, at the center of the Brillouin zone no measurement for $300K$ was possible. The phonon shows a pronounced "softening" from the center of the Brillouin zone towards its middle at around $q = 0.3$. Then the phonon hardens again till the boarder of the Brillouin zone. This effect is again almost temperature independent. However, at $q = 0.35$ a certain difference appears as the phonon hardens when cooling down from $70K$ to $16K$. This "softening" ot the buckling mode is related to the phonon anomaly at around $q = 0.35$.
In summary we can conclude that the phonon bucking mode shows a pronounced "broadening" at $q = 0.35$ along b^* for $16K$. This "broadening" is superconductivity-induced and it is strongly anisotropic. It is most probably related to the interaction of the buckling mode with the apical oxygen mode (at lower energies), as it was described for $YBa_2Cu_3O_7$. The "softening" of this phonon mode around $q = 0.3$ might be related to that "broadening" effect. In any case this phonon anomaly seems to be very interesting. Another interesting fact is that we observe two peaks along the b^* direction and only one along a^*. This is again a pronounced anisotropy of the phonon spectra which was not expected, but can be understood by the eigenvector

of this plane chain mode (at higher energies).

6.11.6 Intensities of the phonon buckling mode for both directions a^* and b^*

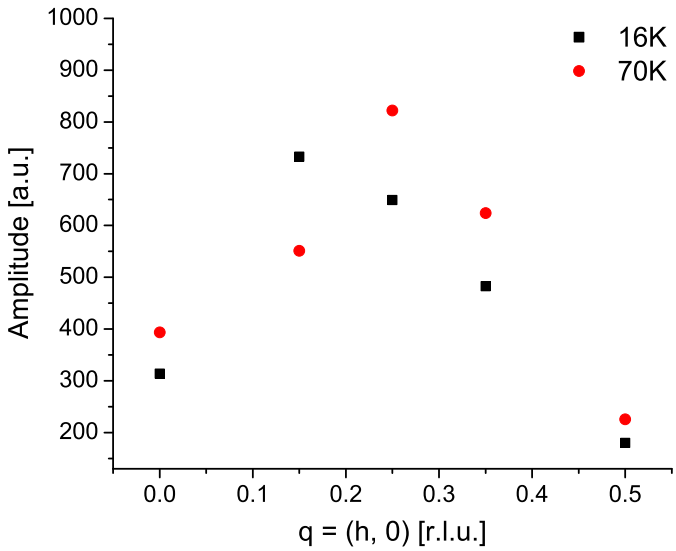

Figure 6.35: This figure shows the intensity (amplitude of the Voigt function) of the phonon buckling mode. The intensity increases towards the middle of the Brillouin zone where it is maximal. This can be observed for both temperatures above and below T_c.

As mentioned earlier the anisotropy of the intensity of the buckling mode between both in-plane directions a^* and b^* and the corresponding anomaly at $q_b = 0.35$ is an very interesting feature. Therefore the intensity of the buckling mode will be investigated and presented in detail. The intensity is given by the formula 6.13. If we don't consider the shape of the phonon but are only interested in the maximal intensity depending on temperature T and $\vec{K}$ this formula tells us that we have to consider the corresponding dependencies of the scattering function 6.4. As mentioned earlier we have corrected the experimental data (intensities) with the Bose factor. Therefore the obtained maximal intensities by the fits should be independent of temperature. For the $\vec{K}$-dependency of the intensity we have to consider the dynamical structure factor 6.6. Our phonon is polarized along the c axis. That means the factor $\vec{K}\vec{\epsilon}$ depends only on K_c, which is the same for all measured phonons (the exception $K_c = 11$ is not considered in this subsection). And the phase of

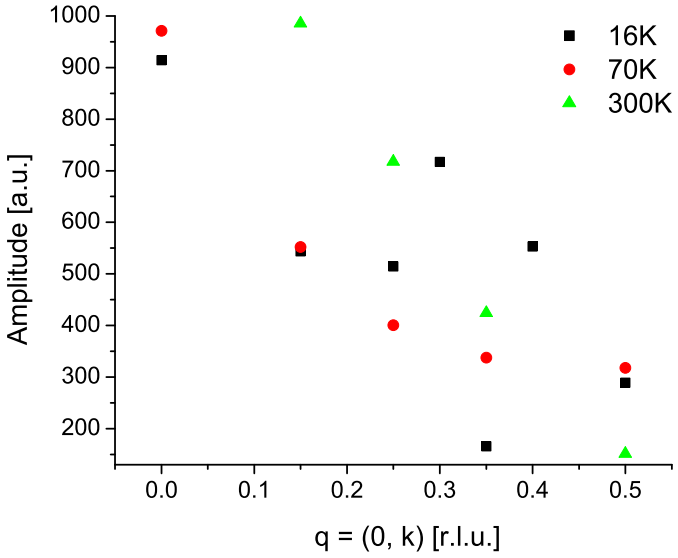

Figure 6.36: This figure shows the intensity (amplitude of the Voigt function) of the phonon buckling mode. The intensities decrease from the center of the Brillouin zone towards the boarder for all temperatures. Moreover for $10K$ the intensity anomaly is been observed at $q = 0.35$. See more details in the text.

the dynamical structure factor is symmetric in a and b (see 6.4) at least in first approximation. Therefore the differences between the measurements along a^* and b^* should be comparable. However this is not the case.
Figure 6.35 shows the maximal intensities of the phonon buckling mode along the a^* direction for different temperatures, that means the amplitude of the Voigt function with which the peaks were fit. The intensities are quite low for the phonons at the center and the boarder of the Brillouin zone. And in the middle there seems to be a pronounced maximum. This behavior can be observed for both temperatures above and below T_c.
Figure 6.36 shows the maximal intensity of our phonon mode along the b^* direction for different temperatures. The overall tendency within the Brillouin zone (from center to boarder) is a pronounced decrease in intensity for both temperatures. However, as for $70K$ (and $300K$) this decrease is the only feature for $10K$ the situation is more complicated. Around $q = 0.35$ there can be observed the intensity anomaly. The intensity for this wave vector is extremely reduced, whereas the intensities of the neighboring wave vectors are enhanced. This feature is superconductivity-induced. As explained earlier this behavior is probably due to an interaction of the buckling mode with the apical oxygen mode which is concerning the mean energy of

the phonons in close vicinity to the buckling mode. For $YBa_2Cu_3O_7$ a correlated increase in intensity of that apical oxygen mode can be observed. Therefore we assume that the intensity anomaly for $YBa_2Cu_3O_{6.6}$ reported here is due to a similar process.

6.11.7 $\vec{K}$-dependence of the phonon buckling mode in $YBa_2Cu_3O_{6.6}$

In the previous subsections we already mentioned that there appears the plane chain mode apart from the phonon buckling mode in $YBa_2Cu_3O_{6.6}$ along the b^* direction. Until now we didn't investigate the relation of the plane chain mode to the buckling

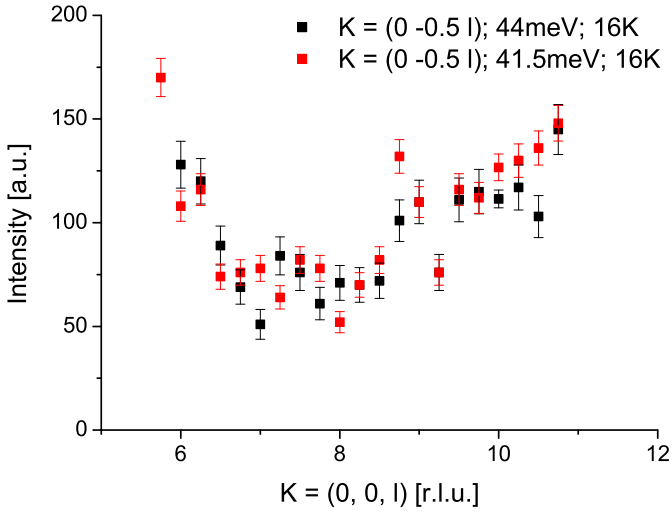

Figure 6.37: This figure shows the $K_c = l$ -dependence of the two peaks being observed. The red graph gives the dynamic structure factor for the main peak at $41.5meV$ (buckling mode). And the black graph gives the same factor for the energy equal $44meV$ which is related to the maxima of the second peak (plane chain mode). The graph shows that both structure factors are very similar what shows the relationship between both phonon modes. See also text.

mode. Therefore we measured the maxima of both peaks (the main peak at lower energies and the smaller peak at higher energies) depending on the $K_c = l$ -value. That means we determined the dynamical structure factor for both peaks. The dynamical structure factor of the phonon buckling mode shows a characteristic l-dependency: it has a pronounced minimum at around $l = 8$ and a strong maximum at $l = 10$ or 11. Figure 6.37 shows the l dependent measurements for both peak

energies: at $41.5meV$ for the main peak in red and at $44meV$ for the small peak in black. Both graphs show a very similar if not identical behavior. Both the minimum are around $l = 8$ and the maximum beginning at around $l = 10$ can be observed for both energies. This means that the plane chain mode seems to be related to the buckling mode. In any case both modes originate due to a c-axis oscillation of the oxygen ions within the CuO_2 double layer. Moreover, it could be that the buckling mode is not only interacting with the apical oxygen mode but also with its second neighbor the plane chain mode at higher energies.

6.12 Comparison and discussion of our measurements on $YBa_2Cu_3O_7$ and $YBa_2Cu_3O_{6.6}$

The first sections of this chapter especially 6.4 and 6.5 are a kind of motivation for the neutron measurements on the buckling mode in this thesis. Moreover, they present a useful basis in order to discuss our measured data from sections 6.11 and 6.9 which will be in addition to its discussion shortly be summarized here.
As we measured the phonon buckling mode on $YBa_2Cu_3O_7$ and $YBa_2Cu_3O_{6.6}$, we first of all observed three independent phonon modes within the energy range where earlier measurements only observed one peak namely the phonon buckling mode. This can be understood by considering that these measurements were performed with twinned single crystals and a spectrometer resolution around $2meV$, whereas we used detwinned crystals and spectrometer resolutions around or below $1meV$. Moreover, these three peaks could be identified. Starting from the lowest energy these phonon modes are the in-plane apical oxygen mode, the out-of-plane buckling mode of the in-plane oxygens and the c-axis polarized plane chain phonon mode of the plane and chain oxygens. For $YBa_2Cu_3O_7$ we observed all of these three modes at the Brillouin zone center and at $q = 0.3$. However, for other phonon wave vectors and for the measurements on $YBa_2Cu_3O_{6.6}$ we only observed the buckling and the plane chain mode of the plane and chain oxygens. For $YBa_2Cu_3O_{6.6}$ the plane chain mode could only be observed along b^* direction, whereas for $YBa_2Cu_3O_{7.0}$ this phonon mode could be observed for both in-plane directions. That means for $YBa_2Cu_3O_{6.6}$ this phonon mode behaves strongly anisotropic, whereas for $YBa_2Cu_3O_{7.0}$ the behavior is symmetric. This might be related to chain oxygens and the superstructure of the oxygen chains.
In addition to this effect, we could confirm the superconductivity-induced phonon softening of the buckling mode at $q = 0$ for $YBa_2Cu_3O_{7.0}$ and we excluded that this effect appears for $YBa_2Cu_3O_{6.6}$. This is consistent with earlier measurements [103], [118].
However, the main effect, a very interesting and completely new effect could be

observed in $YBa_2Cu_3O_{7.0}$, where we observed a superconductivity-induced transfer of spectral weight between the buckling mode and the in-plane apical oxygen mode at $q = 0.3$. This effect can only be observed along the b^* direction, as the apical mode along the a^* direction is not in the vicinity of the buckling mode. Moreover, in $YBa_2Cu_3O_{6.6}$, we could also observe an anisotropic superconductivity induced intensity loss of the buckling mode at $q = 0.35$. However due to statistics or the resolution, there we could not prove the relationship with the apical oxygen mode. In any case we showed the important fact, that superconductivity-induced phonon effects are also present in doping levels far away from the optimally doped case. There is a certain wave vector within the Brillouin zone where the buckling mode shows strong anisotropic anomalies related to superconductivity independent from the doping level.

This superconductivity-induced loss of intensity of the buckling mode in the underdoped superconducting sample and the transfer of spectral weight in the overdoped sample, can be understood by considering the electron-phonon interaction. Due to the electron-phonon interaction the buckling mode and the in-plane apical oxygen mode approach each other, see figure 6.19. This happens around T_c. Then being close enough together both phonon modes interact strongly with each other and exchange spectral weight. That means we have a superconductivity-induced crossing of two phonon modes, which means that the eigenvectors of the phonon modes change. Normally superconductivity renormalizes the energy and the line width broadens, without changing the eigenvector of a phonon mode. However, in our case the phonon line width sharpens, therefore here we observe unusual electron-phonon coupling. This shows especially that the electron-phonon coupling in high temperature superconductors is strong enough in order to lead to very interesting effects which appear in the superconducting phase for different doping levels. As the Fermi surface of $YBa_2Cu_3O_7$ is only weakly nested, we can exclude nesting as a reason for the unusual electron-phonon coupling we observed. However, a possible explanation for such an unusual electron-phonon coupling is that the phonon mode does not interact with the quasi-particle continuum of the electronic states, but with superconductivity-induced collective modes. The most prominent examples for such collective modes are the spin-1 resonance mode [146] and Josephson plasmons [149]. However, both modes do not have the correct dispersion in order to be able to interact with our phonon modes. Therefore it should be investigated whether further predicted collective modes [150], [151], [152] and [153] could be candidates which explain the unusual electron-phonon coupling which we observed for the buckling phonon mode.

A further interesting fact is that the distance of the apical oxygen to the CuO_2 double layer in $YBa_2Cu_3O_{6+x}$ plays an important role in the hole doping process leading to superconductivity (see section 6.1.1). This is further evidence that the interaction of these two phonon modes are closely related to electronic states close

to the Fermi level. In summary our data show, that the superconducting phase transition has important consequences on the buckling mode. This is not controversial. The following question is still highly controversial: why shouldn't be the buckling mode via this unusual electron-phonon interaction in addition to antiferromagnetic fluctuations also be important for the formation of the Cooper pairs.
In order to discuss this question further it might be interesting to consider the electron-phonon interaction from the other point of view namely from that one of the electron. In section 6.5 ARPES measurements have been discussed which relate the phonon buckling mode with the kink of the electron dispersion along the antinodal direction. At the antinode the superconducting gap is maximal. Therefore Cuk et al. and Devereaux et al. are convinced that the buckling mode is important to explain the formation of Cooper pairs [124]. However, this is still controversial. Additional neutron and ARPES measurements are necessary in order to elucidate this issue more conclusively. Especially ARPES measurements on our $YBa_2Cu_3O_{7.0}$ sample should be performed as the ideas from Cuk and Devereaux rely on data on LSCO. Then one could compare ARPES and neutron data for the same sample and strengthen or weaken the relationship between the buckling mode and antinodal electronic states. Moreover, it is known that the phonon buckling mode, which modulates the buckling of the copper-oxide layers, supports d-wave pairing in high temperature superconductors [154], [155], [156] and [157]. However, other phonon modes especially the bond stretching modes are considered to weaken d-wave superconductivity. Therefore the overall effect of phonons in high $T_c's$ should only be weak. However, it is very important to investigate this situation again, by considering the unusual electron-phonon coupling which was uncovered by the data which we presented. Moreover, the buckling mode should be investigated by neutron spectroscopy for other high temperature superconductors, in order to investigate whether these superconductivity-induced intensity effects can also be observed in other compounds. It would be especially interesting to investigate this effect in Hg1234 where for a phonon mode concerning the oxygens in the CuO_2 layers also a superconductivity-induced phonon softening could be observed [158], [159].
However, independent from the question whether these superconductivity-induced intensity effects are related to Cooper pair formation or not, they are interesting phonon anomalies and might be related to other phonon anomalies observed in high temperature superconductors. In section 6.7 phonon anomalies in $YBa_2Cu_3O_{6+x}$ have been described for the bond stretching mode around $q = 0.25$. Therefore these phonon anomalies in $YBa_2Cu_3O_{6+x}$ might have similar reasons. Pintschovius et al. (see section 6.7) relate these anomalies with the formation of dynamical stripes. However, we could explain our phonon anomalies with electron-phonon interaction and the interaction of the buckling mode with the (in-plane) apical oxygen mode. So this anisotropic anomaly can be explained in a natural way without considering stripe effects. So we cannot support the idea of stripe formation in Yttrium Barium

Cuprate. However, both phonon anomalies could be related to strong electron-phonon coupling. In $YBa_2Cu_3O_{6+x}$ the bond stretching mode might be related to the kink in ARPES measurements at the nodal direction of the Brillouin zone, whereas the buckling mode is related to the antinodal kink. The anomalies of the bond stretching mode related to the nodal electronic states are not explicitly superconductivity induced, whereas the anomalies of the buckling mode, which is related to the antinodal electronic states where the gap is maximal, is a clear superconductivity induced effect. This relation would be analogous to the situation in LSCO where a similar relationship between phonon anomalies and the kinks in ARPES measurements have been made (see section 6.5).
In summary we presented an anisotropic phonon anomaly of the intensity of the buckling mode in $YBa_2Cu_3O_{6+x}$, which can be related to a superconductivity-induced transfer of spectral weight between the buckling mode and the in-plane apical oxygen mode in $YBa_2Cu_3O_{7.0}$. This is strong experimental evidence that there appears unusual electron-phonon interaction in $YBa_2Cu_3O_{6+x}$. Moreover a relation to the antinodal electronic states at the Fermi surface, where the superconducting gap is maximal, seems possible. This could mean that the buckling mode in $YBa_2Cu_3O_{6+x}$ is necessary to explain the formation of Cooper pairs. This is in contradiction to the usual opinion that only antiferromagnetic correlations should be responsible for the Cooper pair formation in high temperature superconductors. However, we hope that our measurements are a small but interesting contribution to the controversial discussion whether these magnetic correlations are uniquely responsible for Cooper pair formation or not.

Chapter 7

Neutron spin echo measurements on $YBa_2Cu_3O_7$

7.1 Preparation of the sample

In order to compare the electron phonon coupling for different doping levels a slightly overdoped sample of YBCO has been made: $YBa_2Cu_3O_7$. That means that the Cu-O chains are completely filled with oxygen atoms.
First of all the crystals have been made by the crystal growth service group at MPI. These crystals didn't have the right oxygen content. Afterwards good crystals have been selected for the annealing process. During this process the crystals get the right oxygen content while being in an oven under pure oxygen pressure of 1 bar.
The annealing procedure within the oven, that means the temperature profile was the following: First of all the temperature rises with a rate of 150 K/h for 4.1 h so that the oven reaches a maximal temperature of 630 degree Celsius. This temperature remains for 5h before the temperature decreases by a rate of 30 K/h for 5.3h. Afterwards the oven remains at a temperature of 470 degree Celsius for 100 hours. The temperature is decreased further by a rate of 2K/h for 25 hours, so that the oven reaches a temperature of 420 degree Celsius. This temperature remains the same for 48 hours. Then the temperature is again decreased now by 0.7 K/h for 78 hours. Afterwards the oven has a temperature of 365 degree Celsius which remains the same for several days. This happens so that the Cu-O chains can be filled. The whole annealing procedure happens under oxygen atmosphere. So that the crystals are not exposed in a hot state in the air the crystals are cooled down to the temperature of liquid nitrogen immediately after leaving the oxygen atmosphere in the oven. If the crystals would remain in air under a high temperature it could be that part of the oxygen which has been built into the crystal by the annealing process would diffuse out of the crystal again.

After this process the crystals are slightly overdoped that means the maximal doping with oxygen has been reached. In order to check this for some of the annealed crystals of each batch the transition temperature, which changes with the doping level, was measured with the PPMS (Physical Property Measurement System). Therefore the magnetization of the crystals was measured depending on the temperature. The transition temperature of the measured crystals was $90 \pm 0.5K$. This is slightly below the temperature for the optimally doped $YBa_2Cu_3O_{6.93}$.
The space group of $YBa_2Cu_3O_7$ is orthorhombic and the ab-plane is nearly quadratic. That means that the length of the a and the b axis only differ by around 2 %. Therefore after the growing process the crystals are fully twinned. That means that there exist domains within the crystal where the a and the b axis are interchanged compared with neighboring domains. Therefore the single crystals had to be detwinned. In order to detwin the crystals they are stressed between two small glass plates (with a gold foil between the glass plates and the crystal) which are compressed with a force up to $57N$ and they are set again under oxygen atmosphere. Under these circumstances the crystals are heated again for two hours up to 470 degree Celsius. After this procedure the crystal has been detwinned with a certain probability. We could detwin single crystals of $YBa_2Cu_3O_7$ with a mass up to around $50mg$. The smaller the single crystal was the easier it was to detwin. However certain single crystals with a certain internal structure, meaning that they were no perfect single crystals, couldn't be detwinned at all. Even if the above procedure was repeated two or sometimes even three times. For the experiment, whose results are reported in this chapter, we detwinned more than 100 single crystals which yielded a total mass of $1.5g$.

7.2 Quality of the sample

After having aligned our sample with the Trisp spectrometer we made some measurements in order to check the quality of our sample. These measurements were done in the tree axis mode, that means without the spin echo option. Moreover the spectrometer was operating in the elastic mode, that means the initial and the final wave vector were equal $k_i = k_f = 2.1\mathring{A}^{-1}$. One of the points in reciprocal space we used for the alignment was the strong (2 0 0) reflection of the sample and the energy transfer was also set to zero. Therefore first of all we made a longitudinal scan around the (2 0 0) reflection in order to check how good our sample is detwinned. In figure number 7.1 the resulting graph can be seen. The distance between the small and the large peak corresponds to the difference in the lattice constants a and b. So the small peaks reflects the parts within the sample which are not detwinned. From the ratio of the intensities of both peaks one can determine the degree of detwinning of the sample. This consideration yields that 86 % of the crystal is detwinned. If

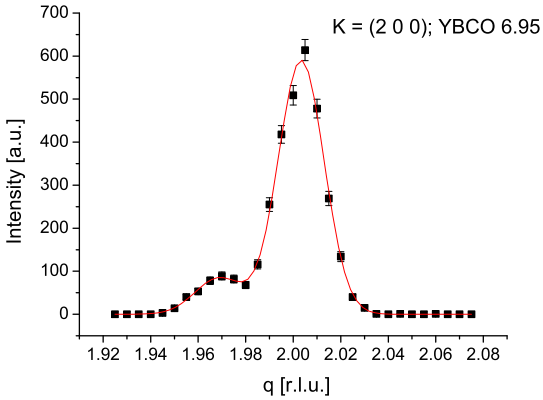

Figure 7.1: Longitudinal scan around the reciprocal lattice point (2 0 0) with the energy also set to zero of our $YBa_2Cu_3O_7$ sample. This scan was made in order to investigate how good our sample is detwinned. The red line is a double Gaussian fit to the experimental data. 86% of the corresponding crystal were detwinned.

one considers that it is quite difficult to detwin $YBa_2Cu_3O_7$ as the Cu-O chains are completely filled, this is a good result.
Except the degree of detwinning for our crystal we also checked the mosaicity (FWHM of a elastic peak measured by an A3 scan) of our crystal. The mosaicity of our crystal is of special interest as we built up our sample out of small single crystals. These single crystals have been aligned with a Laue machine. Thus the mosaicity is an important value in order to characterize our sample. We measured the mosaicity for two reciprocal lattice points within the scattering plane. This was the a^*c^* plane. We didn't measure the mosacity for a point along the b^* axis as we aligned our sample only within the a^*c^* plane of the sample. For the mosacities along the a* and the c^* direction we obtained a similar value for both directions: 1.6 degrees (FWHM). This value was obtained after deconvolution of the spectrometer resolution. Considering that our crystal consists out of several small single crystals that is also a good value.

7.3 Three axis measurements

Before we made our neutron spin echo scans we tried to identify the phonon without the spin echo option that means we performed normal triple axis experiments. However for most of the temperatures and points within the Brillouin zone we couldn't identify the phonon. The reasons could have been that the resolution was around $6meV$ and the signal to background ratio was quite small. Therefore it could be

that a relatively broad peak vanished in high background. However our spin echo scans were much more successful and for two of the three measured temperatures it was consistent with previous Raman measurements made with comparable samples. Another reason could have been that our spectrometer wasn't optimized for normal triple axis measurements.

7.4 The neutron spin echo technique

In this section the neutron spin echo technique will be presented shortly by a classical model, which is enough to understand the technique so far that one can describe and analyze the spin echo data. For a semiclassical and quantum mechanical treatment one can read the paper of Thomas Keller [160] with the title "Neutron Spin Echo - A technique for high resolution neutron scattering". This title reflects the main advantage of the spin echo technique as the energy resolution is much higher compared with standard triple axis spectrometers.
This high energy resolution can be obtained by the use of neutron spin echo coils which polarize the neutrons. One of these coils is situated between the monochromator and the sample and the other one between the sample and the analyzer. Besides these two coils the set-up of the neutron spin echo spectrometer TRISP in Munich, with which we made the following experiments, is equal to the set-up of a normal triple-axis spectrometer for unpolarized neutrons (see figure 7.2). In order to protect the measured spectra from higher order contamination of the monochromator a velocity selector (VS) is used. This velocity selector changes with the wave vector $\vec{k_i}$ of the initial neutrons being selected by the monochromator and hence filters out higher order contaminations for a certain $\vec{k_i}$.

In order to understand the principle of neutron spin echo it is important to know what happens with the neutrons within the coils. The coils exert a magnetic field on the neutrons. Therefore they begin to precess according to their velocity. The neutrons travel with a given velocity v parallel to the y axis through the coils. The exerted magnetic field B is along the z axis and the polarization P is along the x axis (see figure 7.2). The angle ϕ_1, which is the angle of precession of the neutrons travelling through the first coil, is given by the following formula [160]:

$$\phi_1 = \frac{2\omega_{z,1} L_1}{v_1} \tag{7.1}$$

where the Larmor frequency is given by

$$\omega_{L,1} = 2\omega_{z,1} = 2\mu B_1/\hbar, \tag{7.2}$$

with L_1 being the length of the first coil (between the monochromator and the sample), B_1 is the magnetic field of the first coil, v_1 is the velocity of the neutrons

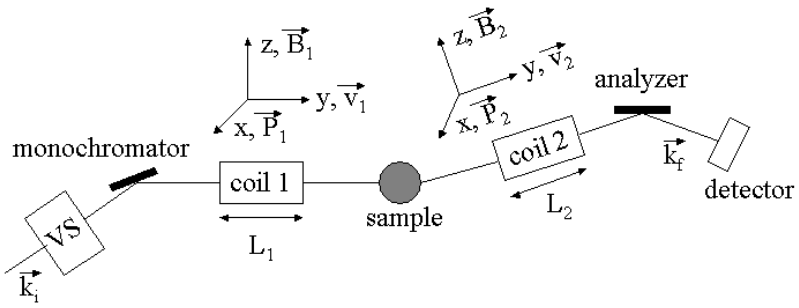

Figure 7.2: Spectrometer set-up of the neutron spin echo spectrometer Trisp in Munich. This set-up is similar with the set-up of a triple-axis spectrometer besides the two coils, which are situated between the sample and the monochromator or the analyzer respectively. When the neutron beam is travelling with v_1 along the y direction within the first coil, it is exposed to a magnetic field along the z direction and it is polarized along the x direction. Within the second coil the neutron beam is exposed to the same magnetic field but along the minus z direction.

travelling within the first coil (this value depends on the wavelength of the neutrons and hence on their wave vector), μ is the magnetic moment of the neutron and $\hbar$ is Planck's constant.
After leaving the first coil the neutrons are polarized and they are travelling through the sample. If one measures phonons the corresponding neutrons change their energy by exciting or annihilating a phonon within the sample. That means the change of the neutron wavelength or the wave vector depends on the energy of the excitation. After having left the sample the neutrons come through the second coil between the sample and the analyzer where they are again exposed to a magnetic field, which is antiparallel to the magnetic field from the first coil. The corresponding angle of precession is given by

$$\phi_2 = -\frac{2\omega_{z,2}L_2}{v_2}, \tag{7.3}$$

where the index 2 stands for the second coil or for the neutrons travelling through the second coil. Assuming that the coils are identical ($B_1 = B_2 = B, L_1 = L_2 = L$) the total angle of precession depends especially on the two different neutron velocities before and after the sample:

$$\phi = \phi_1 + \phi_2 = 2\omega_z L \cdot \left[\frac{1}{v_1} - \frac{1}{v_2}\right]. \tag{7.4}$$

Within the quasi-elastic approximation one can assume $v_2 = v_1 + \delta v, \delta v \ll v_1$ and hence it follows for the precession angle:

$$\phi = \frac{2\omega_z L}{v_1^2}\delta v. \tag{7.5}$$

Together with the neutron energy transfer $\hbar\omega$

$$\hbar\omega = \frac{m}{2}(v_2^2 - v_1^2) = mv_1\delta v, \tag{7.6}$$

where m is the neutron mass, we have the final equation for the precession angle:

$$\phi = \left(\frac{2\hbar\omega_z L}{mv_1^3}\right)\omega = \omega\tau_{NSE}. \tag{7.7}$$

This equation defines the neutron spin echo time τ_{NSE}. τ_{NSE} gives a measure, how fast the precession angle changes with the energy. It can thus be considered as a measure for the "resolution" of a spin echo experiment. And we can write for the neutron spin echo time:

$$\tau_{NSE} = \left(\frac{2\hbar\omega_z L}{mv_1^3}\right) = 1.863 \times 10^{-16} B[Gauss]L[cm]\lambda^3[\mathring{A}]. \tag{7.8}$$

This equation reflects the advantage of long wavelength for high resolution. As a large neutron spin echo time means that the resolution is quite high.
The scattering function $S(q,\omega)$ gives the probability with which a neutron is scattered inelastically by the sample with the energy transfer $\hbar\omega$. The value of the polarization P is then given by the mean value of the cosine of the precession angle:

$$P = \langle\cos\phi\rangle = \int d\omega S(q,\omega)\cos\omega\tau_{NSE} \tag{7.9}$$

That means that the polarization is the cosine Fourier transform of the scattering function $S(q,\omega)$. To be correct one should not only integrate over the distribution of the energy transfer but also over the incident velocity spectrum given by the incident neutron flux from the reactor.
Due to the finite lifetime of the phonons their energy distribution has a Lorentzian line shape. That means the scattering function $S(q,\omega)$ is a Lorentzian function:

$$S(q,\omega) = S(\omega) = \frac{\Gamma}{\pi(\Gamma^2 + \omega^2)}, \tag{7.10}$$

where Γ is the half width at the half maximum (HWHM). with a Lorentzian line shape one can rewrite the dependence of the polarization P from the spin echo time τ_{NSE} (equation 7.9):

$$P = \int d\omega S(q,\omega)\cos\omega\tau_{NSE} = \exp(-\Gamma\tau). \tag{7.11}$$

That means that the dependence of the polarization from the spin echo time and the line width is an e-function. For simplicity for τ_{NSE} it is written in the following τ.

7.5 Neutron spin echo measurements

As shown in the last section for phonons with a finite lifetime the dependence of the polarization, which is been measured with the spin echo spectrometer (Trisp), from the neutron spin echo time is an e-function. In order to measure the phonon line width one measures for different τ-values the polarization of the neutron beam and makes afterwards an fit with the following fitting function through the measured points:

$$y = P0 \cdot \exp(-0.0015185 \cdot \Gamma \cdot x), \tag{7.12}$$

where y corresponds to the polarization, $P0$ is the polarization at the origin, and x corresponds to the neutron spin echo time. This way the phonon line width Γ is treated as free parameter and therefore obtained from the fit. The numerical constant ensures that the spin echo times are given in picoseconds. The polarization is given in per cent of the full polarization. That means in order to measure the phonon line width one has to measure the polarization for different spin echo times. According to equation 7.8 the spin echo time depends on the magnetic field exerted from the coil the length of the coil and the wave length of the neutrons passing through the coil. Moreover the magnetic field depends on the current which flows through the coil:

$$B \cdot L = c \cdot I, \tag{7.13}$$

where I is the current through the coil of length L and with a magnet field B. In order to determine the constant one considers the elastic signal of a coil for one Larmor precession (see figure 7.3). If one considers the precession angle for one Larmor precession this yields the following equation:

$$B \cdot L = \frac{v}{\gamma} = c \cdot I, \tag{7.14}$$

where v is the neutron velocity depending on the wave vector of the neutrons and γ is the gyromagnetic ratio $\gamma = 2920 \cdot 1/(Gauss \cdot s)$. The period of the polarization signal in figure 7.3 corresponds to the current given in equation 7.14. With a polarization signal due to elastic scattering one can determine this period or in other words the corresponding current very accurately whereas this isn't the case for the signal due to inelastic scattering as there the statistics is worse. With that knowledge finally one can calculate the constant in equation 7.14. That the magnetic field depends linear on the current flowing through the coil is also true for inelastic measurements,

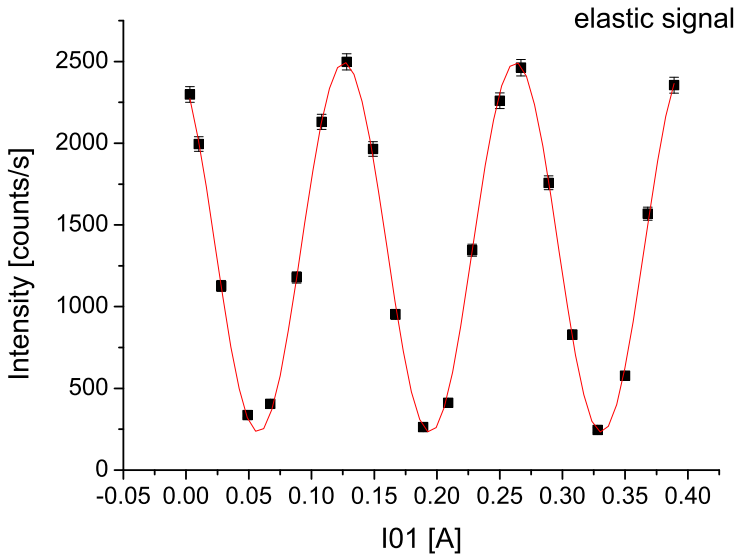

Figure 7.3: Elastic spin echo signal for the coil in the first spectrometer arm (between the monochromator and the sample). The measurement of the elastic signals for both coils are important for the analyzes of the spin echo data. For more information see the text. The measured data have been fitted by a formula like equation 7.15. One can understand the sinusoidal shape of the elastic scattering signal with formula 7.11, if one considers a very sharp (δ-like) scattering function.

thus we have determined the relation between the magnetic field and the current for a given coil. Now we can calculate the spin echo time with equation 7.8 and 7.14 depending on the current which is flowing through the coils. One has only to measure the polarization depending on the current for elastic scattering for both coils. That means we can now calculate the current for both coils such that the resulting spin echo times τ are equal. This is the condition for inelastic spin echo measurements. And a precondition for useful data. In order to obtain a polarization scan (see figure 7.4) one has to scan the current around the mean value in one coil, whereas this mean value corresponds to the fixed current in the second coil so that the spin echo times are equal. Finally one obtains the polarization by fitting the scans like figure 7.4 with the formula

$$y = I0/2 \cdot (1 + P \cdot \cos(2\pi \cdot (x - x0)/dl)), \tag{7.15}$$

with y corresponding to the total intensity, which is measured during the experiment and x the corresponding current, $I0$ the initial intensity, P the polarization, $x0$ the initial current and dl the period of the polarization. The polarization curve

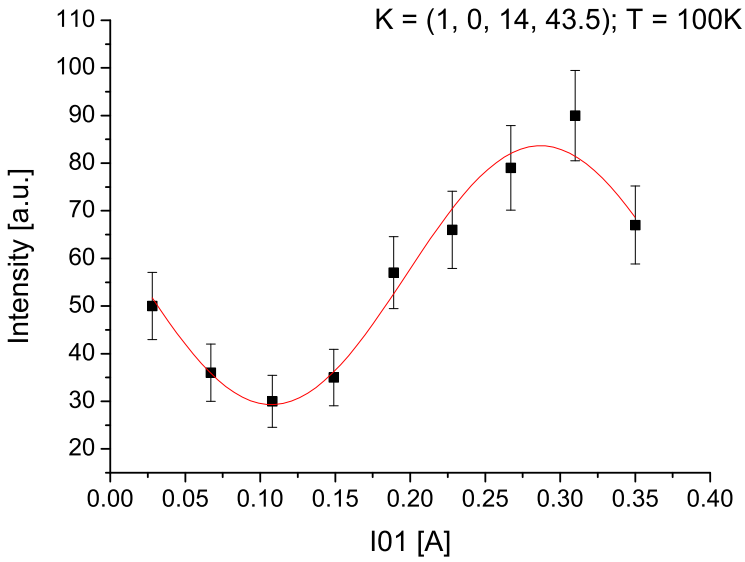

Figure 7.4: Inelastic spin echo scan. That means the polarization (dependence of polarization from the intensity see equation 7.15) is measured for different currents within the first coil. Within the second coil a current flows so that the spin echo time is equal to the mean value of the first coil. We measured within the ac-plane at reciprocal lattice point (1 0 14) and with an energy 43.5 meV at 100K. The measured data have been fitted by a formula like equation 7.15. The fit has been weighted for each point according to the value of the error bar.

in figure 7.4 corresponds to one measuring point of the polarization depending on the spin echo time. That means in order to determine the phonon line width one has to make several such measurements with different spin echo times. The maximal current through the coils limits the measuring points which can be obtained.

7.6 Neutron spin echo measurements on $YBa_2Cu_3O_7$

With the neutron spin echo technique explained in the last two sections we measured the phonon buckling mode (42.5 meV phonon mode) in our untwinned $YBa_2Cu_3O_7$ sample (which has a superconducting transition temperature T_c of around 90 degrees) for different phonon wave vectors q. First off all we made measurements at the Brillouin zone center ($q = 0$) and afterwards for $q = 0.25, 0.4, 0.5$. We made

these measurements for different temperatures. For the phonon wave vectors $q = 0$ and $q = 0.25$ we measured above the transition temperature T_c at $T = 100K$ and below the transition temperature T_c at $T = 70K$ and $T = 10K$. For the phonon wave vectors $q = 0.4$ and $q = 0.5$ we measured only one temperature above and below T_c for $T = 100K$ and $T = 10K$. The measurements were performed so that the a^*c^*-plane of the sample was coincident with the scattering plane of the spectrometer. For the measurements in the following section we used the same sample of $YBa_2Cu_3O_7$ with a superconducting transition temperature of about $90K$.
As monochromator a pyrolytic graphite crystal was used with the (002) reflection. As analyzer we used a Heussler crystal with the (111) reflection. The monochromator crystal was horizontally and vertically bent but the analyzer was only bent horizontally.
We made the following spin echo experiments with the spectrometer configuration (- + +). That means that the direction of rotation for the monochromator was negative whereas the directions of rotation for the sample and the analyzer were positive. We measured with fixed final energy and $k_f = 3.5\mathring{A}^{-1}$. In order to maximize the dynamic structure factor we measured at the reciprocal lattice point (1 0 14) and the energy at which we measured was $43.5meV$. So that we could follow the weakly dispersing phonon buckling mode through the Brillouin zone.

Figure 7.5 presents the measured data for $Q = (1, 0, 14, 43.5)$ at $100K$. We performed eleven inelastic spin echo scans comparable to the scan shown in figure 7.4. The fit for each scan to a sinusoidal polarization function described in the previous section yielded the polarization for a given τ -value. All polarization points depending on the neutron spin echo time were plotted in one diagram and a least square fit to the e-function given in the last section was performed in order to determine the line width of the measured phonon. From that plot we obtained for $Q = (1, 0, 14, 43.5)$ at $100K$ a half width of half maximum (HWHM) of $807 \pm 236\mu eV$. One recognizes that the polarization for small τ-values decreases faster than the fitted function and that the neutron beam was almost depolarized for τ-values around 0.4. For larger τ values the polarization increases again. This can be due to fact that we didn't measure only one phonon but two phonons, which couldn't be resolved due to the triple-axis spectrometer resolution. A second phonon which is close enough in energy to the other one yields an oscillation in the polarization-τ-diagram. However the envelope of the points and our fitted function should yield the right value for the phonon line width.
From the corresponding plot for $70K$ of figure 7.5 we obtained for $Q = (1, 0, 14, 43.5)$ at $70K$ a half width of half maximum (HWHM) of $1353 \pm 393\mu eV$. In the polarization-τ diagram one could also observe an oscillation, which is not as strong as for $100K$.

Figure 7.6 presents the measured data for $Q = (1, 0, 14, 43.5)$ at $10K$. Again we performed for eleven τ-values the polarization scans and performed also an least square fit to the e-function given above. From that plot we obtained for $Q = (1, 0, 14, 43.5)$

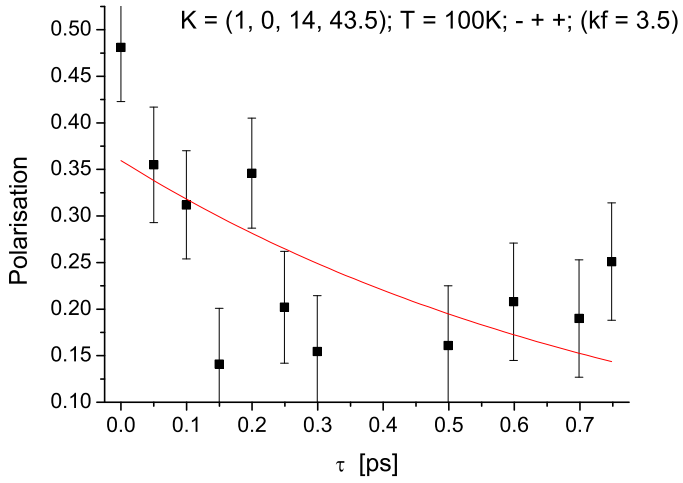

Figure 7.5: Neutron spin echo measurements for $Q = (1, 0, 14, 43.5)$ at 100K with a spectrometer configuration (- + +). We measured with fixed final energy and $k_f = 3.5\mathring{A}^{-1}$. One recognizes that the polarization for small τ-values decreases faster than the fitted function and that the neutron beam was almost depolarized for τ-values around 0.4. For larger τ values the polarization increases again. For a possible explanation see text.

at $10K$ a half width of half maximum (HWHM) of $1681 \pm 329\mu eV$. Again we observe a relative steep decrease of the polarization for small spin echo times and almost depolarization before the polarization increases again for higher spin echo times.

Figure 7.7 presents the measured data for $Q = (0.75, 0, 14, 43.5)$ at $100K$ and $10K$. We performed for seven τ-values the polarization scans for each graph and performed also an least square fit to the e-function given above. From these plots we obtained for $Q = (0.75, 0, 14, 43.5)$ at $100K$ a half width of half maximum (HWHM) of $1529 \pm 312\mu eV$ and at $10K$ a HWHM of $1833 \pm 340\mu eV$. For the measurements at $100K$ we didn't observe an oscillation of the polarization depending on the spin echo time compared to the data we measured at the center of the Brillouin zone. The measured data are lying more or less on the fitted e-function. However for $10K$ there is an odd point which doesn't lay on the fitted e-function.
From the corresponding plot for 70K of figure 7.7 we obtained for $Q = (0.75, 0, 14,$ 43.5) at $70K$ a half width of half maximum (HWHM) of $1838 \pm 446\mu eV$. In the polarization- τ diagram one could also observe an oscillation comparable to these ones observed at the Brillouin zone center.

Figure 7.8 presents the measured data for $Q = (0.6, 0, 14, 43.5)$ at $100K$ and

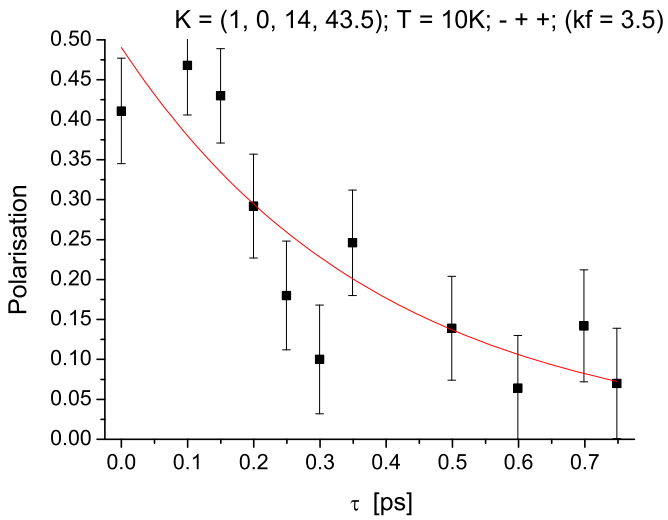

Figure 7.6: Neutron spin echo measurements for $Q = (1, 0, 14, 43.5)$ at $10K$ with a spectrometer configuration (- + +). We measured with fixed final energy and $k_f = 3.5\mathring{A}^{-1}$.

$10K$. We performed for six τ-values the polarization scans for each graph and performed also an least square fit to the e-function given above. From these plots we obtained for $Q = (0.6, 0, 14, 43.5)$ at $100K$ a half width of half maximum (HWHM) of $1689 \pm 395\mu eV$ and at $10K$ a HWHM of $1108 \pm 328\mu eV$. For the measurements at $100K$ we didn't observe an oscillation of the polarization depending on the spin echo time compared to the data we measured at the center of the Brillouin zone. The measured data are lying more or less on the fitted e-function. However for 10K a depolarization before an increase of the polarization for higher spin echo times could again be observed.

Figure 7.9 presents the measured data for $Q = (0.5, 0, 14, 43.5)$ at 100K and 10K. We performed for six τ-values the polarization scans for each graph and performed also an least square fit to the e-function given above. From these plots we obtained for $Q = (0.5, 0, 14, 43.5)$ at $100K$ a half width of half maximum (HWHM) of $1993 \pm 432\mu eV$ and at $10K$ a HWHM of $1449 \pm 308\mu eV$. For the measurements at $100K$ and $10K$ we didn't observe an oscillation of the polarization depending on the spin echo time compared to the data we measured at the center of the Brillouin zone. The measured data are lying more or less on the fitted e-function.
As mentioned previously one possible explanation for the oscillations of the polarization depending on the spin echo time can be, that another phonon is in the vicinity of the phonon buckling mode. Due to the spectrometer resolution function it can

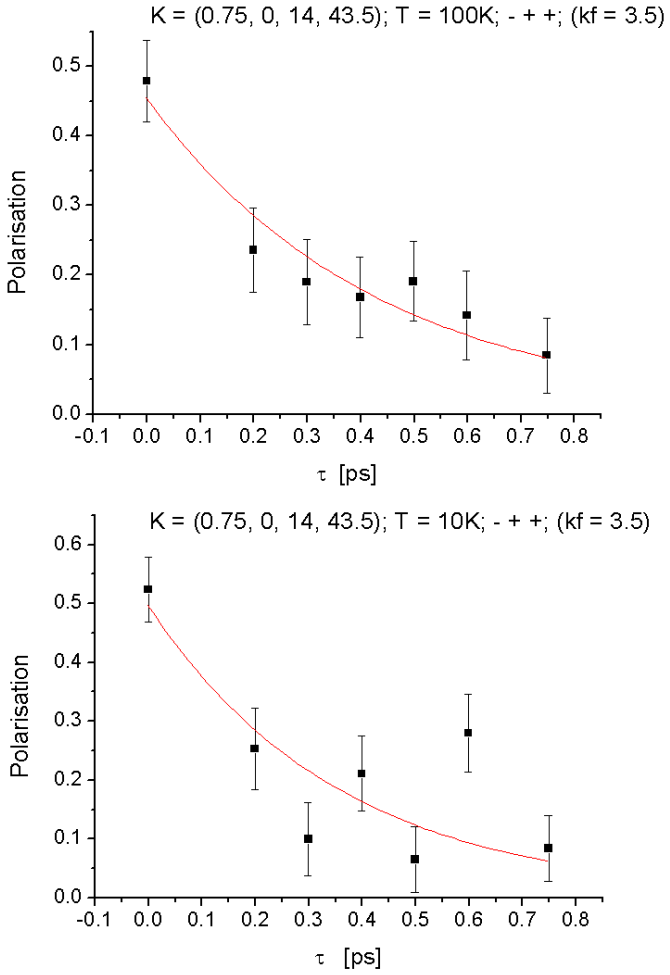

Figure 7.7: Neutron spin echo measurements for $Q = (0.75, 0, 14, 43.5)$ at $100K$ and $10K$ with a spectrometer configuration (- + +). We measured with fixed final energy and $k_f = 3.5\mathring{A}^{-1}$. Compared to the measurements at the Brillouin zone center at this q value no oscillation of the polarization could be observed. However for $10K$ there exists an odd point which isn't lying on the fitted function.

be possible, that we couldn't resolve these two phonons completely and therefore we measured both. This would result in such an oscillation. Therefore we calculated the spectrometer resolution function for the configuration of the spectrometer with which we measured the data above. For our calculation we considered the effective collimations, the lattice constants of the monochromator and the analyzer, the mosaicities of the monochromator, the analyzer and the sample, Popovici's parameters: the width and the hight of the source, the width, hight and the depth of the detector, monochromator, analyzer, sample and finally the distances between these, the

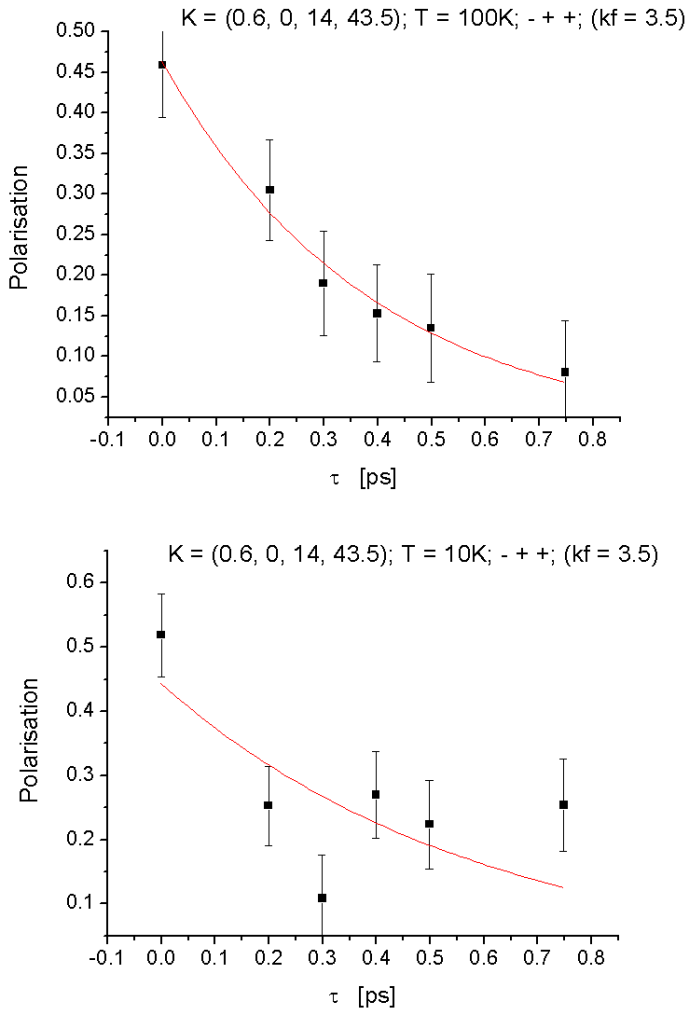

Figure 7.8: Neutron spin echo measurements for $Q = (0.6, 0, 14, 43.5)$ at $100K$ and $10K$ with a spectrometer configuration (- + +). We measured with fixed final energy and $k_f = 3.5\mathring{A}^{-1}$. Compared to the measurements at the Brillouin zone center at this q value no oscillation of the polarization could be observed at $T = 100K$. However for 10K there exists again a depolarization before an increase of the polarization for higher spin echo times.

focusing of the monochromator and the analyzer and that we measured at the reciprocal lattice point $Q = (1, 0, 14)$ at an energy of $43.5meV$ and with fixed final energy corresponding to a final wave vector $k_f = 3.5\mathring{A}^{-1}$ and a spectrometer configuration (- + +). These calculations were performed with Rescal and Popovici's method [**?**] was employed. The result of the resolution of the spectrometer for the given configuration was 6.719 meV. That means we covered the energy range $40.5 \leq E \leq 46.5$

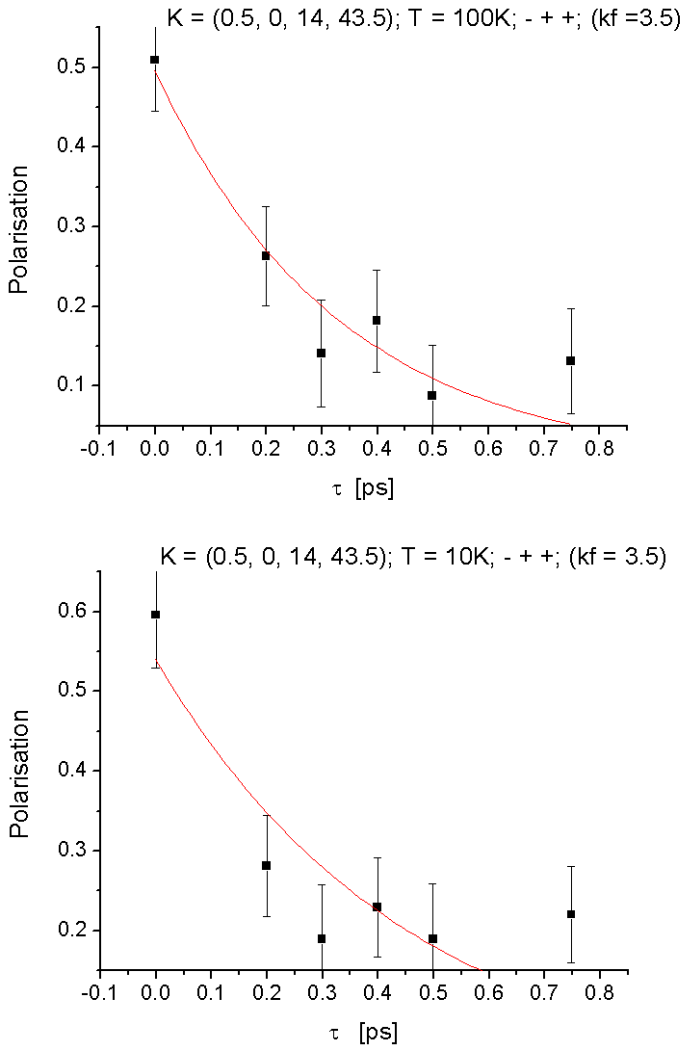

Figure 7.9: Neutron spin echo measurements for $Q = (0.5, 0, 14, 43.5)$ at $100K$ and $10K$ with a spectrometer configuration (- + +). We measured with fixed final energy and $k_f = 3.5\mathring{A}^{-1}$. Compared to the measurements at the Brillouin zone center at this q value no oscillation of the polarization could be observed.

by our spin echo measurements. If one compares this energy range with the data shown in sections 6.9 and 6.11 one recognizes, that we indeed measured two phonon branches with our spin echo measurements: The buckling mode and the plane chain mode. This explains our observed oscillations.

7.7 Summary of results and comparison with Raman results and previous neutron scattering data

Our results of the neutron spin echo measurements obtained with the untwinned $YBa_2Cu_3O_7$ sample are summarized in figure 7.10. It shows the line width (HWHM) of the out of phase buckling phonon mode ($42.5meV$ mode) for the measured q values and different temperatures above and below the superconducting transition temperature of our sample of about $90K$. However, as we could observe oscillations these values might be strongly affected by the distance between the buckling mode and the apical oxygen mode (see figure 6.12).

The "line width" seems to increase from the Brillouin zone center towards the

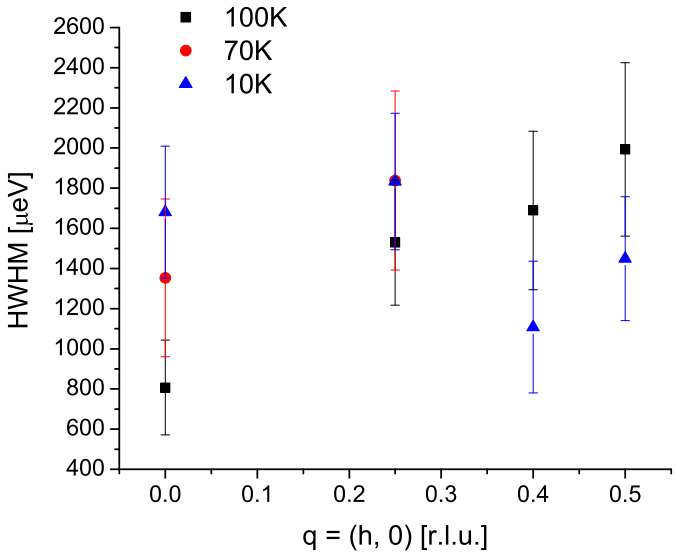

Figure 7.10: Summary of the results of our neutron spin echo measurements. The diagram shows the "line width" of the out of phase buckling phonon mode (HWHM) for different q values and different temperatures above and below T_c.

boarder of the Brillouin zone for $100K$ and $70K$. Whereas such a trend couldn't be observed for the data at $10K$. Here it seems that something interesting happens at q around 0.3. For an optimally doped sample of $YBa_2Cu_3O_{6.93}$ with a transition temperature of $92K$ Raman measurements have been made. These measurements can be compared to the neutron spin echo measurements. For $10K$ a HWHM of $1.96 \pm 0.06meV$, 70K a HWHM of $2.36 \pm 0.06meV$ and for $100K$ a HWHM of $1.91 \pm 0.06meV$ was measured for the phonon line width by Raman spectroscopy.

For $100K$ and $70K$ the results of the Raman measurements are lying within the error bars of the neutron spin echo data. However for 10K there exists a clear discrepancy which might be due to the close vicinity of the apical oxygen mode.
D. Reznik et al. [103] measured the phonon line width of the same phonon with a triple-axis spectrometer also for different q values and for $T = 100K$ above the transition temperature and for $T = 50K$ below the transition temperature. For the 100K data they found a constant phonon line width within the Brillouin zone of around $2meV$ FWHM. At the Brillouin zone center their result is within our error bars, however, for higher q values we measured a larger phonon line width compared to their data. For 50K at the Brillouin zone center they measured a phonon line width of about $2.4meV$, the line width increased to about $2.8meV$ at $q = 0.25$ and decreased again towards the border of the Brillouin zone to about $2.2meV$. These data are within our error bars throughout the whole Brillouin zone. However, we couldn't recognize a maximum of the phonon line width at around $q = 0.25$, which was indicated by the data of Reznik et al. In any case one has to consider the fact that we measured with a completely different sample. They used a big single crystal, which was twinned. Whereas we used an array of small single crystals which has been detwinned and aligned in one direction. So our single crystal was without any inclusions and probably of higher quality. Considering our new data from sections 6.9 and 6.11 one has to state that in both cases (spin echo data and previous measurements by D. Reznik) most probably the distance between the buckling mode and the plane chain mode was measured and not the line width of the phonon buckling mode as intended. However, these spin echo measurements are nevertheless of certain importance, as they prove that these further phonon modes are not spurious.

Chapter 8

Acknowledgement

This PhD thesis would not have been possible without considerable help of numerous people which will be named in the following paragraphs. In my opinion it is almost impossible to name all these persons explicitly, nevertheless, I really did my best:

First of all I'm very grateful to Prof. B. Keimer for accepting me as a PhD student and hence giving me the possibility to work on two projects each of which led to very interesting scientific results. I exceptionally appreciate being supervised by him, as he always was interested in my work, supported me considerably and could help several times, when the projects seemed to be stuck. Finally he ensured that our work was presented in a very interesting and effective way.

My first PhD project is a collaboration with the department of Prof. M. Jansen. Together with Prof. B. Keimer he ensured that my work on this project was successful. Therefore I would like to thank him notably.

I'm also thankful to Prof. M. Dressel for the friendly acceptance to be the ,,Mitberichter" of my PhD thesis.

I'm especially thankful to D. Reznik from the "Forschungszentrum Karlsuhe" and the LLB in Paris, from whom I learned a lot on triple-axis spectroscopy and who contributed considerably to the quality and the understanding of our data on the buckling mode. For the correct understanding and interpretation of the magnetic data on sodium cuprate the help of M. Reehuis was essential. Therefore I'm especially grateful for his contribution. I would also like to thank notably V. Hinkov from whom I learned how to make a high-quality twin-free YBCO7 sample. Moreover he gave me several useful hints during my PhD work. Without the very good collaboration together with M. Sofin who provided me with the sodium cuprate powder sample the corresponding work would have been impossible. Therefore I'm also very grateful.

It was a pleasure to collaborate with and being supported by the local contacts during my experiments on several neutron diffractometers and spectrometers and hence I'm very thankful to all of these people: G. André and F. Bourée from the LLB in

Paris introduced me to magnetic and nuclear neutron diffraction, respectively. D. Reznik introduced me to neutron spectroscopy on a triple-axis spectrometer. Together with D. Lamago his successor I spent some interesting beam times and they even accompanied me to our measurements at the FRM II in Munich. T. Keller introduced me to the technique of neutron spin echo spectroscopy and several advanced aspects of triple-axis spectroscopy. Last but not least I shared two very successful beam times together with K. Hradil from the University of Göttingen and the FRM II. Therefore I'm especially grateful. There I also get acquainted with R. Mole who give us additional help. In addition I would like to thank all the technicians at LLB and FRM II who helped us with their technical knowledge during our experiments.
During my PhD I had a good and important collaboration with the Raman group. Therefore I'm very thankful to M. Bakr for making the Raman measurements and C. Ulrich and M. Cardona for discussions. I'm also very thankful to M. Bröll, who helped me in making our twin-free sample off YBCO7. Moreover I could learn additional knowledge from him about the neutron spin echo technique. In addition I thank L. Capogna for the introduction in the physics of sodium cuprates.
I'm also thankful to R. E. Dinnebier, J. Strempfer and D. Haug who performed x-ray measurements for me, to R. K. Kremer who introduced me to magnetic susceptibility and dielectric constant measurements, to S. Bayrakci who helped me in analyzing Laue pictures, to C. T. Lin, Th. Wolf and A. Maljuk for the production of samples and for the discussions of my experimental results on the phonon buckling mode with V. Damljanović, P. Bourges, Y. Sidis, P. Horsch, C. Bernhard, D. Manske, G. Khaliullin, R.Held, R. Zeyher, L. Pintschovius and O. Gunnarson. At the beginning of my PhD work, I also worked together with P. Lemmens.
I also thank C. Hagemann, Mrs. Schleehauf, Mrs. Süss and Mrs. Sigloch for their continuous support in several administrative procedures. I'm really thankful to H. Klann who gave me an introduction to the PPMS and helped me several times with the installation of computer programs. The same is valid for M. Ohl who constructed for us an appropriate sample holder for our triple-axis measurements. Moreover I'm thankful to C. Busch for technical help during the long preparation of our twin-free sample, B. Baum and S. Lacher for the support in making and preparing the crystals such that they could be easily detwinned. E. Brücher and G. Siegle for susceptibility and dielectric constant measurements. Moreover I'm thankful to H. Bender, L. Dorner-Finkbeiner, A. Schulz and W. Wended for their help with technical problems.
As a scholarship holder of the International Max-Planck- Research School for Advanced Materials I am very grateful to H. G. Libuda for organizing workshops, research schools and last but not least our yearly status seminar, which always included a very interesting excursion. Moreover he helped us with some important administrative work.

I'm very grateful to the group members of the Keimer group for several interesting discussions and especially for the good atmosphere in our group. I would like to acknowledge to my former and actual room mates most of whom I've already mentioned as a collaborator. I'm also very grateful to I. Zegkinoglou, who always encouraged me and was interested in my experiments. I'm also thankful to P. Aynajian with whom I shared the Garching flat when we were both on beam times in Munich. And I can say that I enjoyed it very much discussing my results with him. I also thank P. Yordanov with whom I also had several interesting discussions. I'm also grateful to P. Leininger with whom I had also a lot of interesting discussions on neutron scattering and x-rays. Some of our discussions even have been in French what I especially appreciated. Last but not least I'm also grateful to several good colleagues M. Rahlenbeck, B. Bohnenbuck, S. S. Seok, A. Suchaneck, Y. Matiks, A. Mekonnen, P. Popovich and M. Rawolle.
I'm also thankful to the fine mechanics and glass workshop, the computer specialists and all the other employees including the charwomen and watchmen of the MPI for Solid State Research.
After the PhD the world does not stand still and work continues. Therefore I'm really grateful to Prof. B. Keimer to allow me staying in his group for another few months and giving me the responsibility for co-initiating several very interesting projects. During the preparation for these projects I've already had the pleasure to cooperate with M. Krisch, J. Serrano from the ESRF, C. Ulrich, M. Bakr and with my successor J. Park and N. Munnikes and their supervisors V. Hinkov and T. Keller who will ensure that the sample I've made during my PhD work will reveal further interesting insights in the world of high T_c cuprates. Therefore I'm also very grateful.
Darüberhinaus bin ich besonders meinen lieben Eltern, Brüdern und Herrn Hartmann für ihre kontinuierliche Unterstützung und Motivation während meiner Doktararbeit dankbar.

Chapter 9

Curriculum Vitae

School time

1987-1996	Schelztor Gymnasium (high school) Esslingen (final grade: 1,4)
1993-1996	Participation in the Kepler-Seminar of Natural Sciences and its physics workshop.
1995	8th International Young Physicists' Tournament in Polen
1996	9th IYPT in Georgia (second-best, s. Bild der Wissenschaft 2/1997, page 38)

University

1997-2003	"Diplomstudium" at the University of Stuttgart with focus in biophysics (final grade: good) "Diploma" thesis work: "Configurations of biopolymers on inhomogeneous substrates" (theoretical physics); Prof. Seifert, Prof. Dietrich
2000-2003	Academic master studies at the University of Stuttgart with focus in solid state physics (final grade: very good)
1999/2000	Tutor for the exercises in experimental physics 1 and 2; Dr. Lassmann, Prof. Dressel
2002/2003	Tutor for the exercises in statistical physics (theoretical); Dr. Hanke, Prof. Seifert

PhD thesis in Keimer's group

2003 - 2008 PhD thesis at the Max-Planck-Institute for Solid State Research in Stuttgart within the "International Max Planck Research School for Advanced Materials" (IMPRS-AM) with Prof. Keimer as supervisor.

2005 Hercules course at the ILL and ESRF in Grenoble and at the LLB in Saclay. This course included the presentation of a poster about sodium cuprates.

2005 "Helicoidal magnetic order in the spin-chain compound $NaCu_2O_2$" L. Capogna, M. Mayr, P. Horsch, M. Raichle, R. K. Kremer, M. Sofin, A. Maljuk, M. Jansen and B. Keimer, Phys. Rev. B 71 (14), 140402 (2005).

2007 Properties of HTSC workshop, Munich Residence: talk about "Doping dependence of the buckling mode in the system $YBa_2Cu_3O_{6+x}$"

2008 "Incommensurate spin density modulation in a copper-oxide chain compound with commensurate charge order" M. Raichle, M. Reehuis, G. André, L. Capogna, M. Sofin, M. Jansen and B. Keimer. accepted at Physical Review Letters.

2008 "Unusual electron-phonon interactionof the buckling mode in $YBa_2Cu_3O_7$" M. Raichle, D. Reznik, M. Bakr, C.Ulrich, V. Hinkov, K. Hradil, D. Lamago, M. Bröll, C. T. Lin, Th. Wolf and B. Keimer, submitted.

Bibliography

[1] R. Scherm et al., "Neutrons", in Neutron and Synchrotron Radiation for Condensed Matter Studies, Vol. 1: Theory, Instruments and Methods, ed. J.Baruchel et al. (EDP Sciences - Springer Verlag) (1993).

[2] G. Shirane, S. M. Shapiro, J. M. Tranquada, Neutron Scattering with a Triple-Axis Spectrometer, (Cambridge University Press) (2002)

[3] H. Zabel, "Interaction of Neutrons with Matter: Neutrons - Inelastic Case", in Neutron and Synchrotron Radiation for Condensed Matter Studies, Vol. 1: Theory, Instruments and Methods, ed. J.Baruchel et al. (EDP Sciences - Springer Verlag) (1993).

[4] Ch. Kittel, Einführung in die Festkörperphysik, 12. Auflage, R.Oldenbourg Verlag München Wien (1999)

[5] O. Halpern and M. H. Johnson, Phys. Rev. 55, 898 (1939)

[6] G. E. Bacon, Neutron Diffraction, Third Edition (Oxford Clarendon Press) (1975), p.261

[7] G. L. Squires, Introduction to the Theory of Thermal Neutron Scattering (Dover Publications) (1996), p.150

[8] See, *e.g.*, S. Park, Y. J. Choi, C. L. Zhang, and S-W. Cheong, Phys. Rev. Lett. **98**, 057601 (2007); Y. Naito *et al.*, J. Phys. Soc. Jpn. **76**, 023708 (2007); S. Onoda and N. Nagaosa, Phys. Rev. Lett. **99**, 027206 (2007); H.J. Xiang and M.-H. Whangbo, Phys. Rev. Lett. **99**, 257203 (2007).

[9] See, *e.g.*, A. Lüscher, A.I. Milstein, and O.P. Sushkov, Phys. Rev. Lett. **98**, 037001 (2006).

[10] See, *e.g.*, S. Papanikolaou, K.S. Raman, and E. Fradkin, Phys. Rev. B **75**, 094406 (2007); M. Vojta and O. Rösch, Phys. Rev. B **77**, 094504 (2008); M. Vojta and S. Sachdev, Phys. Rev. Lett. **83**, 3916 (1999).

[11] M. Matsuda *et al.*, Phys. Rev. B **59**, 1060 (1999).

[12] V. Kataev *et al.*,Phys. Rev. Lett. **86**, 2882 (2001); U. Ammerahl *et al.*, Phys. Rev. B **62**, R3592 (2000).

[13] R. Klingeler *et al.*,Phys. Rev. B **72**, 184406 (2005); *ibid.***73**, 014426 (2006).

[14] U. Schwingelschlögl and C. Schuster, Phys. Rev. Lett. **99**, 237206 (2007).

[15] A. Gellé and M.B. Lepetit, Phys. Rev. Lett. **92**, 236402 (2004); Phys. Rev. B **74**, 235115 (2006).

[16] M. v. Zimmermann *et al.*,Phys. Rev. B **73**, 115121 (2006).

[17] A. Rusydi *et al.*,Phys. Rev. Lett. **100**, 036403 (2008).

[18] A. Hayashi, B. Batlogg, and R. J. Cava, Phys. Rev. B **58**, 2678 (1998).

[19] H. F. Fong *et al.*,Phys. Rev. B **59**, 6873 (1999); M. Matsuda, K. Ohyama, and M. Ohashi, J. Phys. Soc. Jpn. **68**, 269 (1999).

[20] M.D. Chabot and J.T. Markert, Phys. Rev. Lett. **86**, 163 (2001); M. Matsuda *et al.*,Phys. Rev. B **71**, 104414 (2005); K. Kudo *et al.*, *ibid.***71**, 104413 (2005); K. Park, Y.J. Lee, and J.T. Markert, Physica C **460–462**, 466 (2007).

[21] M. Sofin, E.M. Peters, and M. Jansen, J. Sol. State Chem. **178**, 3708 (2005).

[22] P. Horsch, M. Sofin, M. Mayr, and M. Jansen, Phys. Rev. Lett. **94**, 076403 (2005).

[23] S. van Smaalen, R. Dinnebier, M. Sofin, and M. Jansen, Acta Cryst. B **63**, 17 (2007).

[24] J. Rodriguez-Carvajal, Physica B **192**, 55 (1993).

[25] Y. Mizuno *et al.*,Phys. Rev. B **57**, 5326 (1998).

[26] S.L. Drechsler *et al.*, Europhys. Lett. **73**, 83 (2006).

[27] S.L. Drechsler *et al.*, Phys. Rev. Lett. **98**, 077202 (2007).

[28] H.J. Xiang, C. Lee, and M.-H. Whangbo, Phys. Rev. B **76**, 220411(R) (2007).

[29] A.A. Gippius *et al.*, Phys. Rev. B **70**, 020406 (2004).

[30] T. Masuda *et al.*, Phys. Rev. B **72**, 014405 (2006).

[31] L. Capogna *et al.*, Phys. Rev. B **71**, 140402 (2005).

[32] M. Boehm *et al.*, Europhys. Lett. **43**, 77 (1998).

[33] Y.J. Kim *et al.*, Phys. Rev. Lett. **83**, 852 (1999); F.C. Chou *et al.*, *ibid.* **78**, 535 (1997).

[34] W. Soller, Phys. Rev. 24, 158 (1924).

[35] C. J. Carlile et al., J. Phys. E 10, 543 (1977).

[36] D. C. Tennant, Rev. Sci. Instrum. 59, 380 (1988).

[37] A. Freund and J. B. Forsyth, "Materials problems in neutron devices", in Treatise on Materials Science and Technology, Vol. 15: Neutron Scattering, ed. G. Kostorz (Academic Press, New York), p.462 (1988).

[38] D. O. Loopster, Nucl. Instrum. Methods 44, 181 (1966).

[39] G. Shirane and V. J. Minkiewicz, Nucl. Instrum. Methods 89, 109 (1970).

[40] M. J. Cooper and R. Nathans, Acta Cryst. 23, 357 (1967)

[41] N. J. Chesser and J. D. Axe, Acta Cryst. A 29, 160 (1973)

[42] Y.Ishikawa, C.R. Jr. Fincher, G. Shirane, BNL Memo G-111, (1980)

[43] P. G. Radaelli, Structural Anomalies, Oxygen Ordering and Superconductivity in $YBa_2Cu_3O_{6+x}$, in Neutron Scattering in Layered Copper-Oxide Superconductors edited by A. Furrer.

[44] J. G. Bednorz and K. A. Müller, Z. Phys. B Condensed Matter 64, 189 (1986)

[45] H. K. Wu et al., Phys. Rev. Lett. 58, 908 (1987)

[46] H. Ibach and H. Lüth, Solid-State Physics - An Introduction to Principles of Material Science, Springer (2003)

[47] R. J. Cava et al., Phys. Rev. Lett. 58, 1676 (1987)

[48] R. M. Hazen et al., Phys. Rev. B 35, 7238 (1987)

[49] T. Siegrist et al., Phys. Rev. B 35, 7137 (1987)

[50] Y. LePage et al., Phys. Rev. B 35, 7245 (1987)

[51] J. J. Capponi et al. Europhys. Lett. 3, 1301 (1987)

[52] D. E. Cox et al., J. Phys. Chem. Solids 49, 47 (1988)

[53] J. E. Greedan et al., Phys. Rev. B 35, 8779 (1987)

[54] F. Beech et al. Phys. Rev. B 35, 8778 (1987)

[55] S. Katano et al, Jpn. J. Appl. Phys. 26, L1046 (1987)

[56] M. A. Beno et al., Appl. Phys. Lett. 51 57 (1987)

[57] W. I. F. David et al., Nature (London) 327, 310 (1987)

[58] A. Santoro et al., Mat. Res. Bull. 22, 1007 (1987)

[59] A. W. Hewat et al., Solid State Communications 64, 301 (1987)

[60] J. D. Jorgensen et al., Phys. Rev. B 36, 3608 (1987)

[61] X. S Wu and J. Gao, Physica C 329 (4), 285 (2000)

[62] I. D. Brown and D. Altermatt, Acta Crystallographica B41, 244 (1985)

[63] P. K. Gallagher, Mat. Res Bull. 22, 995 (1987)

[64] K. Kishio et al., Jpn. J. Appl. Phys. 26, L1228 (1987)

[65] G. van Tendeloo and S. Amelinck, Sol. St. Comm. 63, 603 (1987)

[66] C. Chaillout et al., Sol. St. Comm. 65, 283 (1988)

[67] M. A. Alario-Franco et al., Physica C 156, 455 (1988)

[68] R. J. Cava et al., Phys. Rev. B 36, 5719 (1987)

[69] R. Beyers et al., Nature 340, 619 (1989)

[70] R. J. Cava et al., Physica C 152-155, 560 (1988)

[71] R. J. Cava et al., Physica C 156, 523 (1988)

[72] R. J. Cava et al., Physica C 165, 419 (1990)

[73] A. J. Jacobson et al., Phys. Rev. B 39, 254 (1989)

[74] W. E. Farneth et al., Sol. St. Comm. 66, 953 (1988)

[75] J. D. Jorgensen et al., Phys. Rev. B 41, 1863 (1990)

[76] H. F. Poulsen et al., Nature 349, 594 (1991)

[77] W. E. Pickett et al., Phys. Rev. B 42, 8764 (1990)

[78] D. de Fontaine et al., Phys. Rev. B 36, 5709 (1987)

[79] L. T. Wille et al., Phys. Rev. B 37, 2227 (1988)

[80] P. Burlet et al., Phys. Lett. A 167, 401 (1992)

[81] P. Burlet et al., Workshop on Phase Seperation in Cuprate Superconductors, Erice, Italy, 6-12 May 1992, (World Scientific, Singapore, p. 208)

[82] V. Plakhty et al., Physica C 235-240, 867 (1994)

[83] R. A. Hadfield et al., Physica C 235-240, 1267 (1994)

[84] M. Francois et al., Sol. St. Comm. 66, 1117 (1988)

[85] P. Schweiss et al. Phys. Rev. B 49, 1387 (1994)

[86] L. P. Regnault et al., Phase Digrams and Spin Correlations in $YBa_2Cu_3O_{6+x}$, in Neutron Scattering in Layered Copper-Oxide Superconductors edited by A. Furrer.

[87] L. Ozyuzer et al., Physica C 320, 9 (1999)

[88] Z.-X. Shen et al., Phys. Rev. Lett. 70, 1553 (1993)

[89] I. Giaever., Phys. Rev. Lett 5, 147 (1960)

[90] F. Lombardi et al., Phys. Rev. Lett. 89, 207001 (2002)

[91] H. J. H. Smilde et al., Phys. Rev. Lett. 95, 257001 (2005)

[92] J. R. Kirtley et al., Nat. Phys. 2, 190 (2006)

[93] Ch. Renner et al., Phys. Rev. Lett. 80, 149 (1998)

[94] N. Miyakawa et al., Phys. Rev. Lett. 83, 1018 (1999)

[95] V. M. Krasnov et al., Phys. Rev. Lett. 84, 5860 (2000)

[96] T. Cren et al., Phys. Rev. Lett. 84, 147 (2000)

[97] S. H. Pan et al., Nature 413, 282 (2001)

[98] C. Howald et al., Phys. Rev. B 64, 100504R (2001)

[99] K. M. Lang et al., Nature 415, 412 (2002)

[100] L. Pintschovius and W. Reichardt, Phonon Dispersion and Phonon Density-of-States in Copper-Oxide Superconductors, in Neutron Scattering in Layered Copper-Oxide Superconductors edited by A. Furrer.

[101] W. Reichardt et al., Journal of Superconductivity, Vol. 7, No. 2, 399 (1994)

[102] N. Pyka et al., Phys. Rev. Lett. 70, 1457 (1993)

[103] D. Reznik et al., Phys. Rev. Lett. 75, 2396 (1995)

[104] L. Pintschovius et al., Phys. Rev. Lett. 89, 037001-1 (2002)

[105] L. Pintschovius et al., Phys. Rev. B 69, 214506-1 (2004)

[106] M. d'Astuto et al., Phys. Rev. Lett 88, 167002-1 (2002)

[107] H. Uchiyama et al., Phys. Rev. Lett. 92, 197005-1 (2004)

[108] T. Fukuda et al., Phys. Rev. B 71, 060501(R) (2005)

[109] T. Cuk et al., Phys. Rev. Lett. 93, 117003-1 (2004)

[110] T. P. Devereaux et al., Phys. Rev. Lett. 93, 117004-1 (2004)

[111] H. F. Fong et al., Phys. Rev. Lett. 75, 316 (1995)

[112] F. E. Bates, Phys. Rev. B 39, 322 (1989)

[113] R. Liu et al., Phys. Rev. B 37, 7971 (1988)

[114] M. Krantz et al., Phys. Rev. B 38, 4992 (1988)

[115] B. Friedl et al., Phys. Rev. Lett. 65, 915 (1990)

[116] E. Altendorf et al., Solid State Commun. 80, 627 (1991)

[117] K. F. McCarty et al., Physica (Amsterdam) 192C, 331 (1992)

[118] E. Altendorr et al., Phys. Rev. B 47, 8140 (1993)

[119] B. Friedl et al., Phys. Rev. Lett. 65, 915 (1990)

[120] J. D. Axe. et al., Phys. Rev. Lett. 30, 214 (1973); S. M. Shapiro et al., Phys. Rev. B 12, 4899 (1975)

[121] R. Zeyher and G. Zwicknagl, Z. Phys. B 78, 175 (1990)

[122] F. Marsiglio et al., Phys. Rev. B 45, 9865 (1992)

[123] L. Pintschovius, Phys. Stat. Sol (b), 1-21 (2004), page 10; R. Heid private communications

[124] X. J. Zhou et al., Angle-Resolved Photoemission Spectroscopy on Electronic Structure and Electron-Phonon Coupling in Cuprate Superconductors, in the Handbook of High- Temperature Superconductivity edited by J. R. Schrieffer and J. S. Brooks, Springer Science and Business Media, LLC. (2007)

[125] P. V. Bogdanov et al., Phys. Rev. Lett. 85, 2581 (2000)

[126] A. Lanzara et al., Nature 412, 510 (2001)

[127] A. Kaminski et al., Phys. Rev. Lett. 86, 1070 (2001)

[128] P. D. Johnson et al., Phys. Rev. Lett. 87, 177007 (2001)

[129] S. V. Borisenko et al., Phys. Rev. Lett., 90, 207001 (2003)

[130] X. J. Zhou et al., Nature 423, 389 (2003)

[131] G.-H. Gweon et al., Nature 430, 187 (2004)

[132] L. Pintschovius and M. Braden, Phys. Rev. B 60, R15039 (1999)

[133] R. J. McQeeney et al., Phys. Rev. Lett. 82, 628 (1999)

[134] A. D. Gromko et al., Phys. Rev. B 68, 174520 (2003)

[135] T. K. Kim et al., Phys. Rev. Lett. 91, 167002 (2003)

[136] Z. Islam et al., Phys. Rev. B 66, 092501 (2002)

[137] Z. Islam et al., Phys. Rev. Lett. 93, 157008-1 (2004)

[138] J. Strempfer et al., Phys. Rev. Lett. 93, 157007-1 (2004)

[139] L. Pintschovius, Phys. Stat. Sol (b), 1-21 (2004)

[140] S. L. Chaplot et al., Phys. Rev. B 52, 7230 (1995)

[141] W. Reichardt, J. Low Temp. Phys. 105, 807 (1996)

[142] J. M. Tranquada et al., Nature 375, 561 (1995)

[143] H. A. Mook et al., Nature 404, 729 (2000)

[144] J. Humlicek et al., Physica C 206, 345 (1993)

[145] M. Bakr et al., unpublished work (2007)

[146] M. Eschrig, Adv. Phys. 55, 47 (2006)

[147] U. Welp et al., Physica C 161, 1 (1989)

[148] V. Hinkov et al., Nature 430 (7000), 650 (2004)

[149] D. van der Marel, J. Supercond. 17, 559 (2004)

[150] D. van der Marel et al., Phys. Rev. B 51, 1147 (1995)

[151] H. Y. Kee et al., Phys. Rev. B 58, 15035 (1998)

[152] P. A. Lee et al., Phys. Rev. B 68, 024516 (2003)

[153] E. Kaneshita et al., Phys. Rev. Lett. 88, 115501 (2002)

[154] S. Y. Savrasov et al., Phys. Rev. Lett. 77, 4430 (1996)

[155] T. Sakai et al., Phys. Rev. B 55 8445 (1997)

[156] O. Jepsen et al., J. Phys. Chem. Solids 59, 1718 (1998)

[157] C. Honerkamp et al., Phys. Rev B 75, 014503 (2007)

[158] X. J. Zhou et al., Phys. Status Solidi (a) 202, R7 (1997)

[159] V. G. Hadjiev et al., Phys Rev. B 55, 12770 (1997)

[160] Thomas Keller et al., "Neutron Spin Echo - A technique for high resolution neutron scattering" (unpublished data).